Inelastic WIMP-Nucleus Interactions in XENON100 and Cables and Connectors for XENON1T

Dissertation

zur

Erlangung der naturwissenschaftlichen Doktorwürde
(Dr. sc. nat.)

vorgelegt der

Mathematisch-naturwissenschaftlichen Fakultät

der

Universität Zürich

von

Gaudenz P. Kessler

von

Leukerbad VS

Promotionskomitee:

Prof. Dr. Laura Baudis (Vorsitz)
Prof. Dr. Florencia Canelli
Prof. Dr. Marc Schumann

Zürich, 2016

©2016 – Gaudenz Kessler
all rights reserved.

Abstract

The primary purpose of the XENON Dark Matter Project is the direct detection of weakly interacting massive particles (WIMPs). The discovery of these particles would provide a solution to one of the most exciting mysteries of modern physics: The presence of dark matter in our universe. Data collected during 225 live days from 2011 to 2012 could exclude a spin-independent WIMP-nucleon cross section of $2 \times 10^{-45}\,\mathrm{cm}^2$ for a WIMP mass of $55\,\mathrm{GeV/c}^2$. XENON1T, the successor of XENON100, is currently in the commissioning phase. It is designed to test cross sections down to $1.6 \times 10^{-47}\,\mathrm{cm}^2$ at a WIMP mass of $50\,\mathrm{GeV/c}^2$.

This thesis presents an analysis of inelastic WIMP scattering off ^{129}Xe nuclei in XENON100. For the two isotopes ^{129}Xe and ^{131}Xe, which have low-lying excited states of 36.9 keV and 80.2 keV, respectively, the expected interaction rate is calculated. For this analysis the isotope ^{129}Xe was chosen due to its improved sensitivity. The signature of this interaction is the simultaneous observation of an 36.9 keV de-excitation gamma and the recoil energy on the nucleus. Two different methods are shown and compared. The first method exploits the characteristic of nuclear recoils that introduce an asymmetry to the distribution of these events compared to the background distribution of electronic recoils. The second method compares the number of expected events with the number of measured events. For the determination of the signal region, a Monte Carlo simulation was performed. The resulting limit on the cross section is at $1.3 \times 10^{-38}\,\mathrm{cm}^2$ for a WIMP mass of $140\,\mathrm{GeV/c}^2$ for the asymmetry based method. In comparison, the other method excludes cross sections down to $6.4 \times 10^{-38}\,\mathrm{cm}^2$ for $134\,\mathrm{GeV/c}^2$ WIMP masses. The asymmetry based method is more sensitive to background fluctuations.

The XENON1T experiment houses 254 photomultiplier tubes (PMTs). 1041 high voltage cables and 1031 signal cables with a total length of 11.4 km were installed. The details of the development and installation of the cables and connectors in the detector are described in the framework of this thesis. Due to strict background requirements of the experiment ultra low radioactivity cables and connectors had to be used. The performance of the cables and the custom connectors in the detector were tested and it was proven that all connections are successfully established.

Zusammenfassung

Das XENON Dark Matter Projekt hat den direkten Nachweis von *weakly interacting massive particles* (WIMPs) zum Ziel. Würde der Nachweis gelingen, wäre dies eine Erklärung für eines der spannendsten offenen Fragen der modernen Physik: die Dunkle Materie in unserem Universum. Der XENON100-Detektor konnte aufgrund von Daten, die über 225 Tage aufgezeichnet wurden, einen Wirkungsquerschnitt zwischen WIMP und Neutron von $2 \times 10^{-45}\,\mathrm{cm}^2$ ausschliessen für eine WIMP-Masse von $55\,\mathrm{GeV/c}^2$. Der Nachfolger von XENON100, XENON1T, wird zur Zeit in Betrieb genommen. Das Ziel dieses Detektors wird sein, einen Wirkungsquerschnitt von $1.6 \times 10^{-47}\,\mathrm{cm}^2$ auszuschliessen.

Die vorliegende Arbeit stellt die Analyse von inelastischen Wechselwirkungen zwischen einem WIMP und einem ^{129}Xe Kern im XNEON100-Detektor vor. Die erwartete Wechselwirkungsrate wird für die beiden Isotope ^{129}Xe und ^{131}Xe berechnet, die niedrige Anregungszutände von 36.9 keV und 80.2 keV aufweisen. Für die Analyse wird jedoch nur das sensitivere ^{129}Xe verwendet. Die Charakteristik für eine solche Wechselwirkung ist die gleichzeitige Beobachtung des Gammateilchens der Kernabregung und des Rückstosses des Xenonkerns. Es werden zwei verschiedene Methoden vorgestellt. Die erste Methode nutzt den Umstand, dass die Signalereignisse aufgrund des Kernrückstosses asymmetrisch zu den Untergrundereignissen verteilt sind. Die zweite Methode vergleicht die Anzahl der erwarteten Ereignisse mit den beobachteten. Für diese Methode wurde eine Monte-Carlo-Simulation für die Bestimmung der Signalregion durchgeführt. Die Methode, welche die asymmetrische Verteilung ausnutzt, ist empfindlicher gegenüber Schwankungen des Untergrunds und führt zu einem Limit auf dem Wirkungsquerschnitt von $1.3 \times 10^{-38}\,\mathrm{cm}^2$ für eine WIMP-Masse von $140\,\mathrm{GeV/c}^2$. Die andere Methode kann einen Wirkungsquerschnitt von $6.4 \times 10^{-38}\,\mathrm{cm}^2$ ausschliessen.

Für den Bau des XENON1T-Detektors wurden 254 Photomultiplier mit der Elektronik verbunden. Es wurden 1041 Hochspannungskabel und 1031 Signalkabel verlegt mit einer Gesamtlänge von 11.4 km. Die vorliegende Arbeit zeigt die Entwicklung und die Installation der Kabel und Steckverbindungen des Experiments. Wegen der strengen Anforderungen an den radioaktiven Untergrund im Detektor, mussten möglichst strahlungsarme Materialien verwendet werden. Es wurde erfolgreich getestet, dass alle Kabel im Detektor funktionieren.

Contents

Listing of figures

Listing of tables

Acknowledgments

Ich danke besonders und in allererster Linie Laura Baudis, hätte ich doch ohne sie niemals die Möglichkeit gehabt, diese Arbeit zu erstellen und konnte ich wegen ihr in einem der interessantesten Gebiete der modernen Physik einen Beitrag leisten. Sie hat mich speziell gefördert, ein breites Spektrum an Aufgaben zu übernehmen. Dadurch habe ich spannende Einblicke in die Datenanalyse, Hardware sowie die Operation und die Kalibrierung des Detektors erhalten können.

Enorme Unterstützung habe ich von Marc Schumann erhalten. Mein Dank gilt seiner Geduld, mit der er meine vielfältigen Fragen über das Experiment und meine Arbeit geklärt hat. Dadurch hat er mir schwierigen Phasen oft gute Hilfestellungen gegeben und dadurch konnte ich viel von ihm lernen.

Von meinen Kollegen möchte ich vor allem Alexander Kish hervorheben, der mir seine Hilfe über die gesamte Zeit angeboten hat, sowie Aaron Manalaysay und Teresa Marrodan, die mir beim Einarbeiten in mein Projekt grosszügig zur Verfügung standen. Für meine Arbeit an der Datenanalyse haben mir die intensiven Diskussionen mit Rafael Lang, Ludwig Rauch, Shayne Reichard, Francesco Piastra, Giovanni Benato und Alessandro Manfredini sehr viel geholfen. Bei meiner Arbeit an den Kabeln und Konnektoren, bin ich dankbar, mit Martin Auger, Domenico Franco und Guillaume Plante zusammengearbeitet zu haben, von denen ich jeweils viel profitiert habe. Hier haben mich auch Achim Vollhardt und Daniel Florin von der Elektronikwerkstatt sehr stark unterstützt. Beim Bau der Konnektor-Teile war die Hilfe von Andreas James und der Werkstatt-Mitarbeiter, allen voran Reto Maier und Kurt Bösiger unerlässlich.

Während meiner Doktorarbeit war mir aber die persönliche Unterstützung unzähliger Mitmenschen ausserordentlich wichtig. Enorm viel hat mir der Rückhalt und die Unterstützung in meiner Familie bedeutet. Dafür danke ich meinen Eltern Nelly und Sigurd und meinen Brüdern Reto und Björn ohne die ich ganz sicher niemals dort stehen würde, wo ich jetzt bin.

Unter meinen Arbeitskollegen will ich an dieser Stelle Manuel Walter, Giovanni Benato, Julien Wulf, Peter Barrow und speziell meinem Mitbewohner Daniel Mayani nennen, mit denen ich privat und beruflich sehr gut ausgekommen bin und die die Arbeitszeit bereichert haben.

Ein grossartiges Dankeschön gilt meinen Freunden ausserhalb der Arbeit. Besonders froh bin ich, dass ich mit Benedikt Ofner, Hendrik Meyer, Ekaterina Panfilova, Admiral Viscount Nelson, Simon Rösch, Floor Tanner, Virgína Almeida, Daniela Abílio und Corinne Knöpfel Zeit verbringen konnte. Sie alle wissen, warum. Einen speziellen Stellenwert nehmen Sandro D'Amato, Chris Marentini und Roman Gredig ein, mit denen ich sowohl sportlichen Ausgleich und endlos viele spannende und bereichernde Diskussionen haben durfte. Danke!

1 Introduction

The study of the nature of Dark Matter is one of the most important open questions in modern fundamental physics. The most popular model to explain Dark Matter assumes the existence of Weakly Interacting Massive Particles (WIMPs) [1] that accounts for 27% of the total mass-energy of the universe [2]. The following section describes the indications for Dark Matter and WIMPs and introduces the XENON Dark Matter search project.

1.1 Observational Evidence for Dark Matter

The first claim of an experimental observation of an effect caused by dark matter comes from the Dutch Astronomer Jan Oort. In the year 1932 he observed that stars in our galaxy were moving faster than expected [3]. Today it is, however, assumed that his observation is rather explained by dust and gas in the galaxy, than by dark matter [4].

Only one year later, in 1933, the Swiss astronomer Fritz Zwicky studied the velocities of extragalactic nebulae in the Coma cluster [5]. He found that the motion of the galaxies contradicts the expectation deduced by the viral theorem, if the mass of the galaxies is calculated by the luminous content of the galaxy.

One of the strongest indications of the existence of dark matter is the observation of the rotation curves of galaxies. In 1959 Louise Volders measured the rotation velocity in M33 [6] and observed that it differs from the expected motion if the mass inside the galaxy is distributed like the luminosity. In 1960 Vera Rubin observed the velocity of stars with a higher precision [7]. She could show that mostly all objects in a galaxy move with the same velocity.

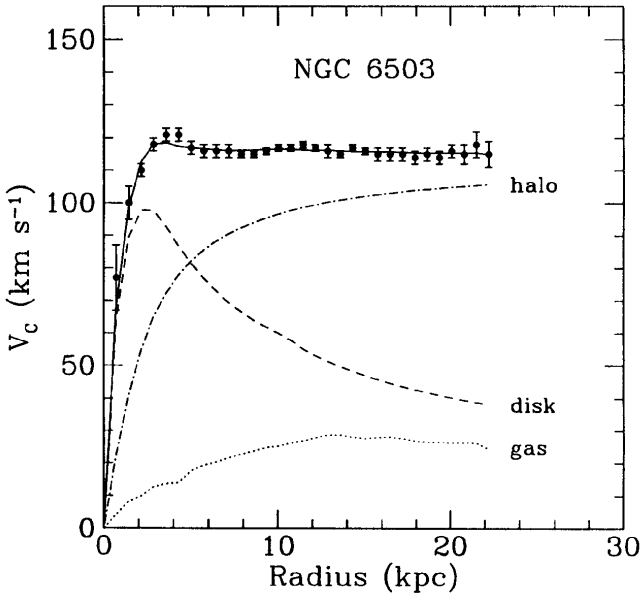

Figure 1.1: Rotation curve of the galaxy NGC 6503. Almost all objects move with the same velocity while it is expected that the velocity decreases with the radius. Figure taken from [8]

But for objects in a larger distance to the center this is an evidence that the mass distribution is linearly increasing with the radius, which is not the case for the stars. Figure 1.1 shows the rotation curve for the spiral galaxy NGC 6503. The radius of the observable part of the galaxy is about 5 kpc. Due to Newtonian laws objects in a further distance r to the center are expected to move with a velocity

$$v(r) = \sqrt{\frac{GM(r)}{r}}\,, \tag{1.1}$$

where G is the Newtonian gravitational constant and $M(r)$ is the total mass of the galaxy inside of r (dashed line in figure 1.1). Instead, the velocity of the object stays constant for radii larger than 10 kpc. This suggests the existence of a non-luminous halo consisting of dark matter.

The ability of mass to deflect light was described by Einstein in 1911 [9]. F. Zwicky was the first to consider galaxies as the light source and to detect heavy non-luminous matter in between [10]. This effect is called *weak lensing*. Using this effect the observation of the *bullet cluster* [11] was a remarkable evidence for the existence of dark matter. It could show the local separation of hot gas and of heavy mass from two colliding galaxies (figure 1.2). This observation contradicted a theory of modified Newton dynamics (MOND), that suggests

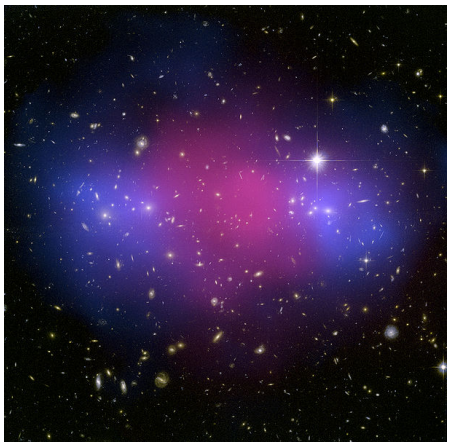

Figure 1.2: Bullet cluster. The picture shows a photograph made by the Hubble space telescope. The mass distribution that was calculated by weak lensing of the background is shown in blue. The x-ray emission of baryonic matter is shown in red.

that modified Newton's laws on larger scales is responsible for the observed properties of galaxies [12].

The cosmic microwave background (CMB) is the radiation from the last scattering before the recombination about 380 thousand years after the Big Bang. With time the light cooled down to a temperature of 2.7 K. The angular anisotropies in the CMB are a result of acoustic oscillations in the photon-baryon plasma in the early universe. These oscillations occur because gravitational mass tends to enhance anisotropies whereas the photons tend to counterbalance them. The anisotropies were measured first by the COBE satellite [13], by WMAP [14] and recently by the Planck satellite [2]. Figure 1.3 shows the power spectrum obtained by Planck, i.e. the strength of the fluctuations in the temperature depending on the angular scale where they occur. The position and the ratio of the peaks from the first order and higher order oscillations give information about the densities of baryonic matter, dark matter and dark energy. Latest results from Planck yield that 27% of the universe consist of dark matter.

1.2 Dark Matter Detection Experiments

Figure 1.4 illustrates three different possible ways, how dark matter can be detected. Experiments can search for product particles from the annihilation of WIMPs. The instruments Fermi [15], MAGIC [16] or H.E.S.S. [17] look for the photons created by WIMP annihilation. IceCube [18] or ANTARES [19] are telescopes searching for neutrinos that could be formed by WIMP annihilation and PAMELA [20] or AMS [21] could detect anti-fermions as a part of the

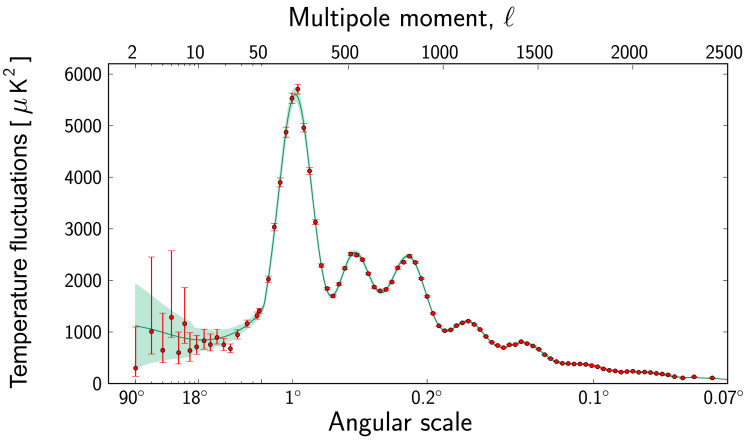

Figure 1.3: Planck power spectrum from the Planck satellite. Figure taken from [2]

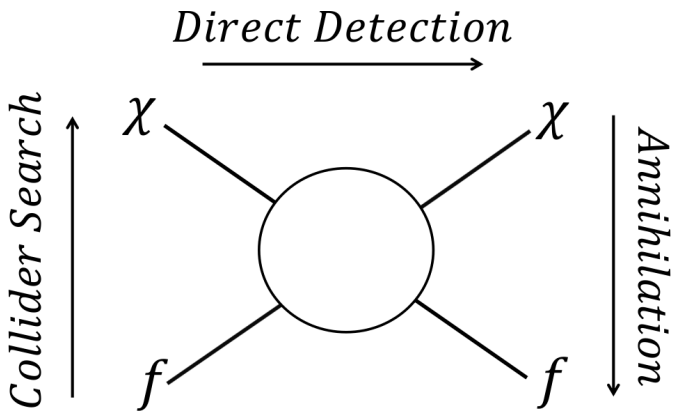

Figure 1.4: Possible interactions between a WIMP (χ) and a fermion (f).

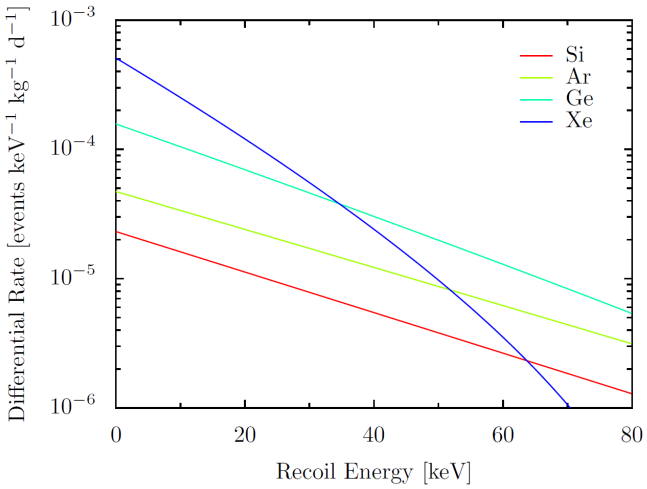

Figure 1.5: Recoil spectra of WIMPs with different detector materials. A WIMP with a mass of $m_\chi = 100$ GeV/c^2 and a cross section of $\sigma = 10^{-44}$ cm^2 is assumed. Figure taken from [24].

product from the annihilation process. None of these experiments has observed a significant signal for dark matter.

Particle colliders could produce WIMPs that would manifest in the form of a missing momentum of the collision. At the Large Hadron Collider (LHC) no dark matter signal has been found so far [22, 23]

Direct detection experiments use the interaction of a WIMP with normal matter. Figure 1.5 compares the expected differential rate per target mass for the four different detector materials silicon, argon, germanium and xenon. The rate is proportional to the square of the mass number A^2. Hence elements with a higher mass number are preferred. Since the recoil rate decreases exponentially with the recoil energy, a low energy threshold is crucial for direct detection experiments. Of the four compared elements xenon is the one with the highest expected rate. Its nuclear form factor is responsible for the stronger decrease for higher recoil energies compared to the other elements. The recoil spectrum of xenon is further discussed in section 3.1 of this work.

The DAMA/LIBRA experiment [25] and the CoGeNT experiment [26] look for the annual modulation in their data employing NaI and germanium crystals, respectively. The annual modulation is originated by the fact that while the earth travels around the sun it runs against the wind of WIMPs at one point the year. This leads to an increased number of WIMP interaction compared to half a year later, when the earth travels with the WIMP wind.

The experiments CDMS [27] and EDELWEISS [28] measure ionization and phonons simultaneously in a silicon and a germanium crystal, respectively. CRESST [29] employs phonons

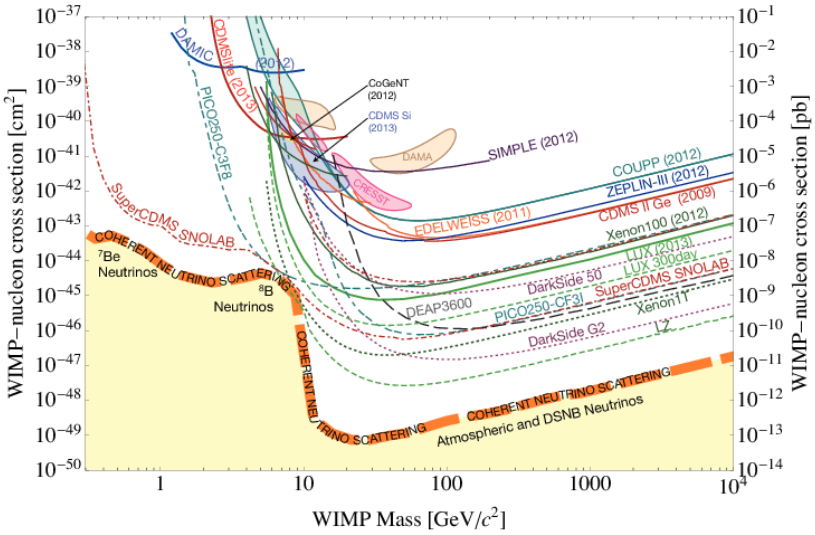

Figure 1.6: Overview over the current spin-independent limits on the WIMP-nucleon cross section (solid lines) together with claims of WIMP signals (closed areas) from current experiments and the expected sensitivities for planned direct detection experiment (dashed lines). The solar neutrinos, atmospheric neutrinos and the neutrinos from supernovae (shown as yellow band at the bottom) introduce an irremovable background in the experiments and restricts the possibility to probe the WIMP-nucleon cross section at small values. Figure taken from [39].

and scintillation in a $CaWO_4$ crystal. The experiments PICASSO [30], COUPP [31] and PICO [32] use bubble chambers containing a superheated solution.

This work will present the XENON100 experiment [33] and the XENON1T experiment [34] in detail. These experiments use the liquefied noble gas xenon and reads out the scintillation light and ionization simultaneously. Instruments that work likewise are ZEPLIN [35], LUX [36] and DarkSide [37]. The last instrument contains liquid argon. XMASS [38] is an example for a liquid xenon detector observing only the scintillation light. Figure 1.6 shows an overview over the current limits on the spin-independent WIMP-nucleon cross section of leading experiments.

This work evolved in the framework of the XENON collaboration and deals with the detectors: XENON100 that is currently operating at the Laboratory of Gran Sasso [41], and XENON1T that was constructed there between 2013 and 2016. Chapter 2 briefly describes the two detectors and their working principle. Aside from spin-independent elastic interactions, WIMPs can scatter spin-dependently on nuclei with a non-zero spin via an axial-vector

coupling. There are two such nuclei in xenon, ^{129}Xe and ^{131}Xe, with a spin of 1/2 and 3/2 respectively. By an inelastic interaction together with a spin change with another particle both of these isotopes can be excited to a low-lying excited state. In the search to find dark matter, this work presents a method to search for inelastic spin-dependent WIMP-nucleon interactions using data from the XENON100 detector, that was taken in the years 2011 and 2012. The analysis is described in chapter 3. XENON1T is the successor of XENON100 and the next important step in the search for dark matter in the universe. In the construction process of XENON1T 248 light sensors in the detector had to be connected to the electronics. This work contains the development and installation of the cables and connectors. It is described in chapter 4.

2

Direct Dark Matter Detection with the XENON Dark Matter Project

The XENON Dark Matter Project contains various instruments for the search for Dark Matter interactions in liquid xenon. The first detector, XENON10 [40], at the Gran Sasso underground laboratories (LNGS) [41] in the Abruzzo mountains in Italy could demonstrate the performance of xenon dual phase time projection chambers (TPCs). With 15 kg of liquid xenon it led to a limit on the WIMP nucleon cross section of $8.8 \times 10^{-44}\,\mathrm{cm}^2$ for a WIMP mass of $100\,\mathrm{GeV}/c^2$ at 90% confidence level (C.L.) in 2008.

The successor, XENON100, was the continuation of the same detector principle and was installed at the same location. The amount of xenon was increased by a factor 10 to 161 kg and the detector was designed to have a 100 times lower radioactive background in the signal regions [33]. These improvements enabled the detector to set the most sensitive upper limit at the time for spin-independent [42] and spin-dependent WIMP-nucleon interactions [43].

The current project, the XENON1T detector, is designed to probe a 100 times lower WIMP-nucleon cross section [34]. The detector principle will be described in more detail below as well as both experiments, XENON100 and XENON1T.

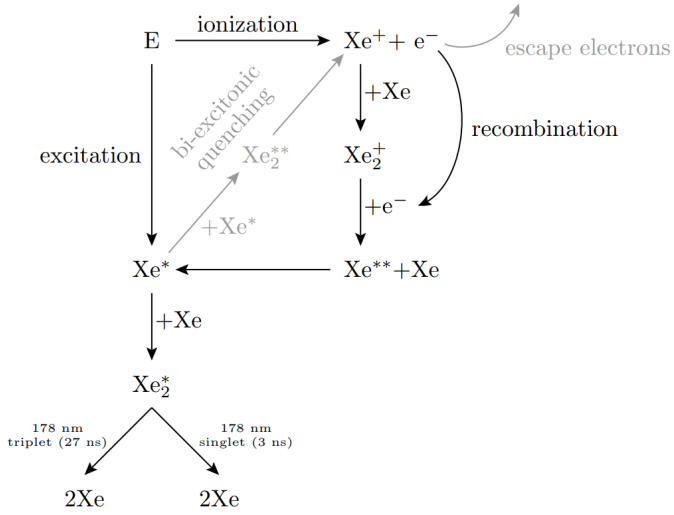

Figure 2.1: Schematic of the scintillation mechanism: an energy deposition leads to excimers either through excitation or ionization. The deexcitation of the excimers produces scintillation light.

2.1 Working Principle of a Xenon TPC

This section describes the scintillation process that occurs when a particle scatters off an atom in liquid xenon and the working principle of a dual-phase time projection chamber (TPC) employing liquid and gaseous xenon as it is used in the XENON100 and the XENON1T experiment.

2.1.1 Scintillation and Ionization Properties of Liquid Xenon

Xenon is a noble gas that rarely occurs in the Earth's atmosphere (with 0.09 ppm) [44]. There are nine stable or almost stable isotopes in natural xenon. All other isotopes have a live time of less than 5.3 days [44]. Therefore xenon has a very low intrinsic radioactivity.

Like other liquid noble gases, xenon shows a large gap between the valence and the conduction band [45]. In its liquefied state it creates both scintillation light and ionization when interacting with a charged particle or γ rays. Figure 2.1 shows a schematic of the scintillation process. An energy deposition in liquid xenon excites a xenon atom and forms an *exciton* Xe^* or ionizes it to form an ion Xe^+. An exciton can form an *excimer*, an excited molecular state, Xe_2^* with another xenon atom from its environment. When these excimers disintegrate and decay to their ground level, they create light with a mean wavelength of 178 nm. This corresponds to an energy of 7 eV [46, 47]. (Light of this wavelength is called vacuum scintillation

light, since it is absorbed by oxygen in air and hence requires vacuum to propagate.)

$$\mathrm{Xe}^* + \mathrm{Xe} \rightarrow \mathrm{Xe}_2^* \tag{2.1}$$

$$\mathrm{Xe}_2^* \rightarrow 2\mathrm{Xe} + h\nu \tag{2.2}$$

On the other hand, ions and electrons recombine. This process as well produces excitons.

$$\mathrm{Xe}^+ + \mathrm{Xe} \rightarrow \mathrm{Xe}_2^+ \tag{2.3}$$

$$\mathrm{Xe}_2^+ + e \rightarrow \mathrm{Xe}^{**} + \mathrm{Xe} \tag{2.4}$$

$$\mathrm{Xe}^{**} \rightarrow \mathrm{Xe}^* + \text{heat}\,, \tag{2.5}$$

followed again by eq. 2.2. Excimers can occur in two spin states: a singlet and a triplet. The life times of the two states are 2.2 and 27 ns, respectively, generated by relativistic electrons in liquid xenon [48]. The ionization density plays a role for the time scale of the scintillation processes and hence varies for other types of interaction, for example for α particles [49]. However, in the presence of an electric field, a fraction of the free electrons from the ionization process gets extracted before they have the chance to recombine with nearby ions.

Assuming that all excimers produce a photon, the number of photons N_{ph} and the number of free electrons N_q can be written as [50]

$$N_{ph} = N_{ex} = N'_{ex} + rN_i \tag{2.6}$$

$$N_q = (1 - r)N_i\,, \tag{2.7}$$

where $r \in [0, 1]$ is the fraction of ions that recombine and produce excimers, N_{ex} is the total number of produced excimers, N'_{ex} is the number of excimers produced directly by eq. 2.1 and N_i is the number of ionized xenon atoms. The average energy to produce either a free electron or a scintillation photon is [51]

$$\varepsilon = 13.7 \pm 0.2\,\mathrm{eV}\,. \tag{2.8}$$

Hence, from the detected number of scintillation photons n_γ and free electrons n_e, the recoil energy can be expressed by

$$E_{\mathrm{er}} = \varepsilon(n_\gamma + n_e)\,. \tag{2.9}$$

While the recoil with electrons converts almost all the available energy into excitation of xenon atoms, nuclear recoils lose a considerable part of the available energy in atomic motion and hence to heat. Therefore, eq. 2.9 is only suitable to calculate the energy of an absorbed particle recoiling on the shell electrons of the xenon atoms. These particles are in principle electrons and γ's. For nuclear recoils the energy gets reduced by the *Lindhard factor* [52, 53]

$$f_n = \frac{kg(e)}{1 + kg(e)}\,, \tag{2.10}$$

where [54]

$$g(e) = 3e^{0.15} + 0.7e^{0.6} + e\,, \tag{2.11}$$

$$e = 11.5 \cdot \frac{E_R}{\text{keV}} \cdot Z^{-7/3} \tag{2.12}$$

$$k = 0.133 \cdot Z^{2/3} \cdot A^{-1/2} \tag{2.13}$$

For xenon $k = 0.166$ [54]. The energy for a nuclear recoil becomes

$$E_{\text{nr}} = \varepsilon(n_\gamma + n_e)/f_n\,. \tag{2.14}$$

P. Sorensen and C. E. Dahl [53] suggest to use $k = 0.110$. The relation between the nuclear recoil energy and electronic recoil energy is shown in figure 2.2 for $k = 0.110$ and $k = 0.166$.

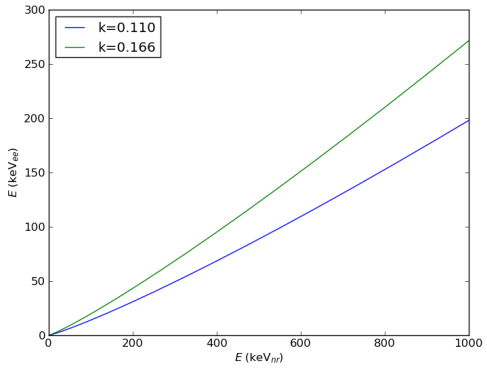

Figure 2.2: The relation between E_{nr} and E_{er} is given by the quenching factor f_n ($E_{\text{nr}} = E_{\text{er}} \cdot f_n$).

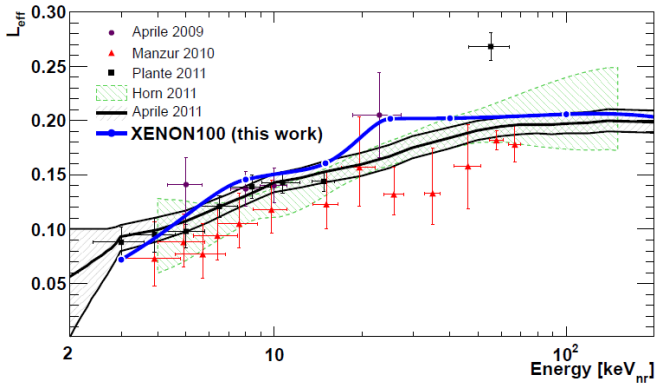

Figure 2.3: Measurements of $\mathcal{L}_{\text{eff}}$. Figure taken from [58]

2.1.2 Energy Determination in Liquid Xenon Detectors

In practice, the relative scintillation efficiency $\mathcal{L}_{\text{eff}}$ is measured, rather than the Lindhard factor, since it is experimentally accessible. For a specific nuclear recoil energy E_{nr}, it is defined as:

$$\mathcal{L}_{\text{eff}}(E_{\text{nr}}) = \frac{L_{y,\text{nr}}(E_{\text{nr}})}{L_{y,\text{er}}(E_{\text{er}} = 122\,\text{keV})}\,, \tag{2.15}$$

where $L_{y,\text{nr}}(E_{\text{nr}})$ is the light yield of a nuclear recoil with the energy E_{nr}. $L_{y,\text{nr}}$ is normalized to the light yield of an electronic recoil of a 122 keV gamma, as it is emitted by the common calibration source ^{57}Co. Indirect measurements of $\mathcal{L}_{\text{eff}}$ compare Monte Carlo Simulation with experimental data from a neutron source with an energy spectrum and were performed by Sorensen et al. [55], Lebedenko et al. [56], Horn et al. [57] or Aprile et al. [58]. Direct Measurements (performed by Aprile et al [59, 60], Chepel et al. [61], Manzur et al. [62] or Plante et al. [63]) use a monoenergetic neutron source recording fixed-angle scatters. They contain less systematic uncertainties than indirect measurements. Figure 2.3 shows the results of the determination of $\mathcal{L}_{\text{eff}}$ from neutron calibration data in XENON100 in comparison with other measurements.

For the charge yield of nuclear recoils $Q_Y(E)$ is the analog of $\mathcal{L}_{\text{eff}}$ and gives the number of free electrons N_q per keV_{nr} deposited energy,

$$Q_y(E) = \frac{N_q}{E}\,. \tag{2.16}$$

Measurements of Q_y were performed by Aprile et al. [64, 58], Manzur et al. [62], Sorensen et al. [55] or Horn et al. [57] (Figure 2.4).

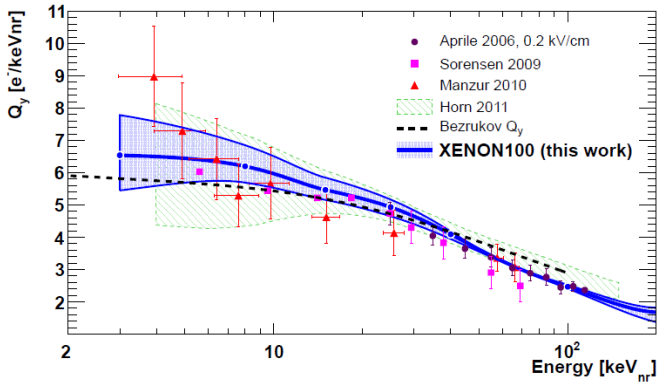

Figure 2.4: Measurements of Q_y. Figure taken from [58]

2.1.3 Event Reconstruction

As described above, an energy deposition that occurs inside the sensitive volume of the liquid xenon in the detector due to a particle interaction produces two kinds of signals (figure 2.5).

- The *direct scintillation light (S1)* is detected by the photomultipliers in the arrays below and above the TPC.
- The free electrons drift upwards due to an electric field that is applied between the anode at the bottom of the TPC and the gate grid that is on ground level at the top of the TPC. After the electrons pass the gate grid they are accelerated into the gaseous phase by another electric field between the gate grid and the anode in the gaseous phase. There each electron produces scintillation light with the xenon atoms in the gas (S2). The light that is emitted in the gaseous phase is hence proportional to the number of free charges produced in the particle interaction. Therefore, the S2 signal is also called *proportional scintillation light.*

An example of a waveform observed in the XENON100 detector of a low-energy event is shown in figure 2.6. The light collection efficiency for the bottom array is more reliable for the energy reconstruction of the S2 events, since the light emission occurs so close to the top PMT array. Therefore for the calculation of the size of the S2 pulse, only the light collected by the bottom $S2_b$ PMTs is used.

The ratio of S2/S1 depends on the ionization density of the particle interaction [47]. This is higher for nuclear recoils, hence an event produced by a WIMP or a neutron has a lower ratio S2/S1. This allows for an effective discrimination of the electronic recoil produced by β or γ particles as shown in figure 2.7. The events are transformed to the so called *flattened*

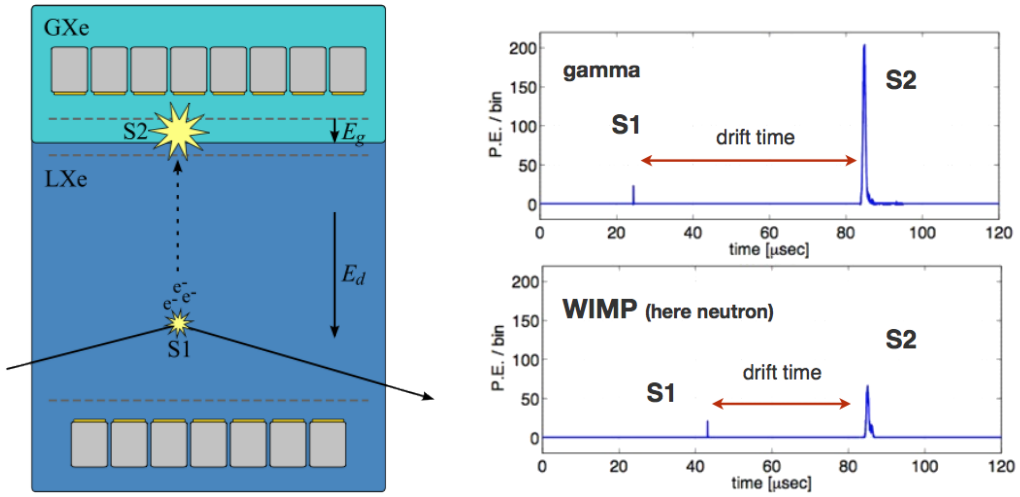

Figure 2.5: Working principle of a xenon dual phase TPC. Left: A particle interaction creates direct scintillation light (S1) and free electrons that drift to liquid-gas surface due to an electric field. There the electrons create proportional scintillation light. Right: the time difference between the S1 and the S2 pulse is determined by the distance of the interaction and the liquid-gas surface. The ratio S2/S1 is different for electronic recoils (for example created by gammas) and nuclear recoils (like with WIMPs).

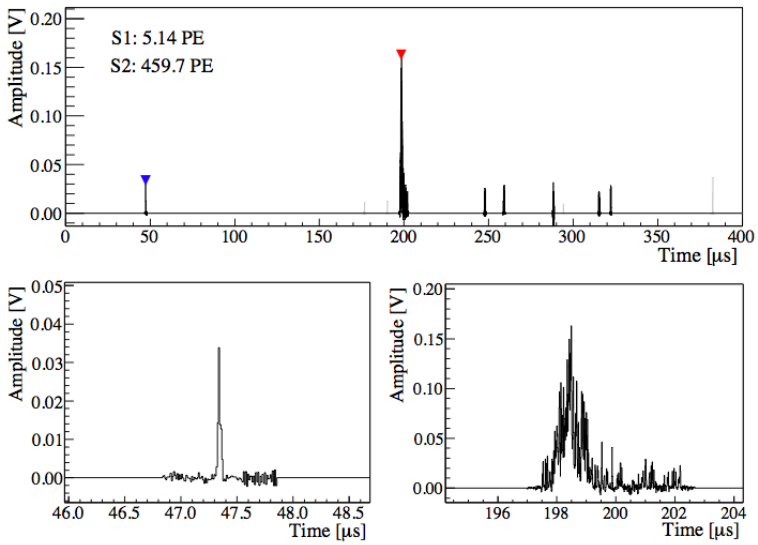

Figure 2.6: An example of a low energy event obtained by the XENON100 detector. The S1 pulse at $t \approx 47$ μs is marked with a blue triangle and shown in detail in the bottom left plot. The S2 pulse at $t \approx 200$ μs is marked with a blue triangle and shown in detail in the bottom right plot. Figure taken from [33].

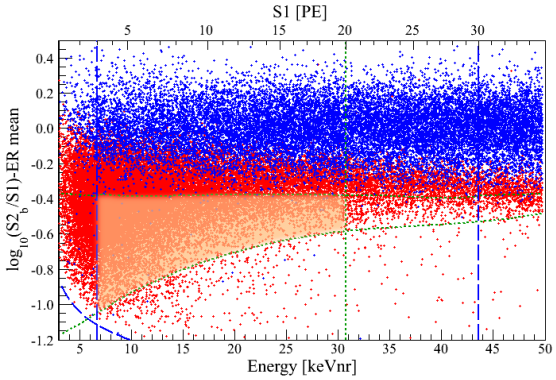

Figure 2.7: Discrimination of electronic recoil events in the flattened parameter space. The Electronic recoil events (blue) are produced with an ^{60}Co calibration source. They are distributed around 0. The nuclear grecoil events distribution (red) comes from an AmBe neutron calibration source.

parameter space

$$\text{flattened space} = \log\left(\frac{S2_b}{S1}\right) - \text{ER}_{\text{mean}}\,, \tag{2.17}$$

which is defined, such that the electronic recoil events are distributed around the value 0. Here 50% of the nuclear recoil events are located below the 99.5% quantile of the electronic recoil event distribution.

Position Reconstruction

Since for a given electric field the drift velocity of the electrons is constant, the depth of the event in the detector (z component of the position) can be determined by the time difference between the S1 and the S2 signal. Since the S2 signal is emitted very close to the top PMTs, the light hit pattern of the top PMT array allows for the reconstruction of the x and y component of the events location. Therefore a selection of an inner partial volume (called *fiducial volume*, FV) is possible to reject regions near the border of the TPC that show a high rate of background. This feature belongs to the most powerful of a dual-phase TPC.

2.2 The XENON Dark Matter Project

This section briefly describes the setup of the XENON100 and the XENON1T detector. Further information can be found in [33] and [34], respectively.

2.2.1 XENON100

The XENON100 detector [33] is to date operated at the Gran Sasso Underground Laboratory [41] and aims to directly detect Dark Matter particles scattering off xenon nuclei. Its core piece is a dual phase (liquid-gas) xenon time-projection chamber (TPC). The total amount of liquid xenon is 161 kg, 62 kg of which are in the active target enclosed in a cylindrical Teflon/copper structure, which is 30.5 cm high and has a radius of 15.3 cm. The residual 99 kg xenon form the surrounding active veto. The direct and proportional UV light signal produced by particle interactions is detected by 242 Hamamatsu R8520 PMTs with 1 inch square photocathode windows, which are optimized for the response to light in the vacuum ultraviolet regime. 98 PMTs are located in the top PMT array in the gas phase arranged in concentric circles for optimized resolution of the radial event position reconstruction. They cover 43.9% of the top PMT array area. The 80 PMTs in the bottom array are optimized for maximum area coverage such that 52% of the bottom array's area is covered with sensitive area of a PMT. 64 PMTs detect interaction in the veto, a 4 cm thick layer of liquid xenon, surrounding the TPC from all sides.

Event position reconstruction

For the position reconstruction in XENON100 three different algorithms were used:

- Minimizing the χ^2 between the hit pattern and Monte Carlo simulations,
- Support vector machine (SVM) or
- Neural network (NN).

The two latter methods are trained with simulated data. The method using NN has been found to produce the most precise and reliable results and is therefore used to determine the event position for the analysis. However, it is required that all three methods produce consistent results. Hence a full 3D event position reconstruction is possible. An example hit pattern is shown in figure 2.8. Event position reconstruction is important to correct for the inhomogeneous light collection efficiency for different locations in the TPC (c.f. [33]).

Electronic Background

The understanding of the background in the detector is crucial for a rare event search experiment. Therefore each component of the detector is selected to meet the stringent requirements for low radioactivity. For the background estimation in XENON100 a GEANT4 [65] simulation for the radioactive decays of all materials in detector with a detailed geometry was performed [66]. To obtain the data for the simulation, the radioactivity of every component

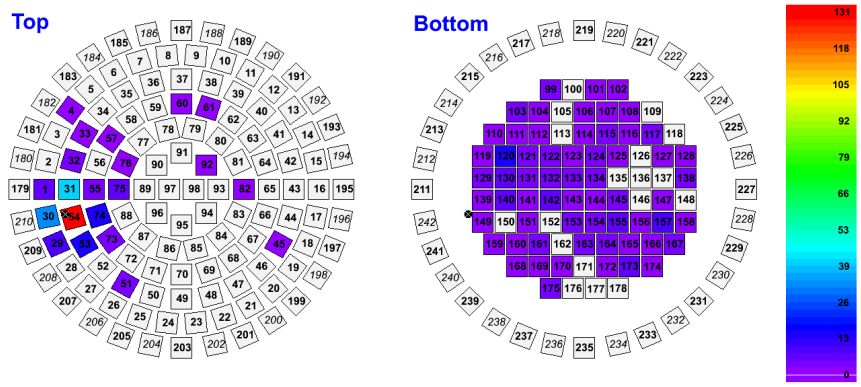

Figure 2.8: Example hit pattern of an event for the top (left) and the bottom (right) PMT array that is used for the event position reconstruction in x and y direction. Figure taken from [33].

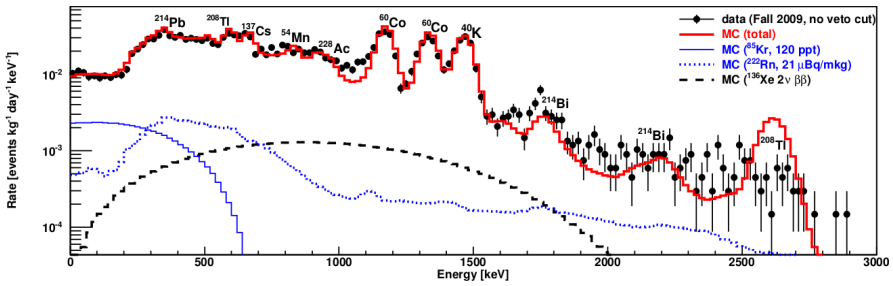

Figure 2.9: Electronic recoil background in XENON100. The total energy spectrum from the Monte Carlo simulations (red) and the measured spectrum (black). Figure taken from [66].

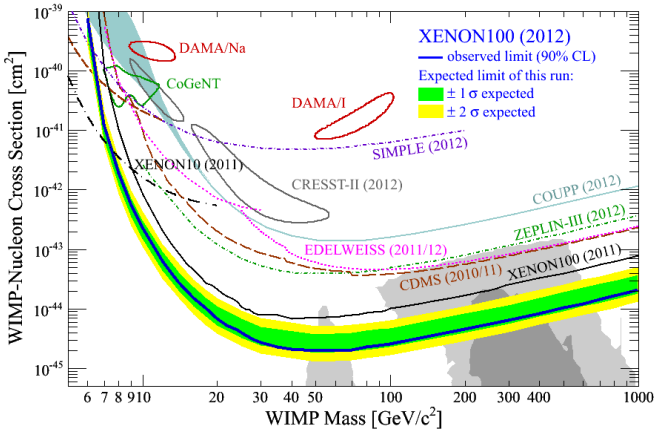

Figure 2.10: Limit of the XENON100 detector from 225 life days for spin independent coupling. Figure taken from [42].

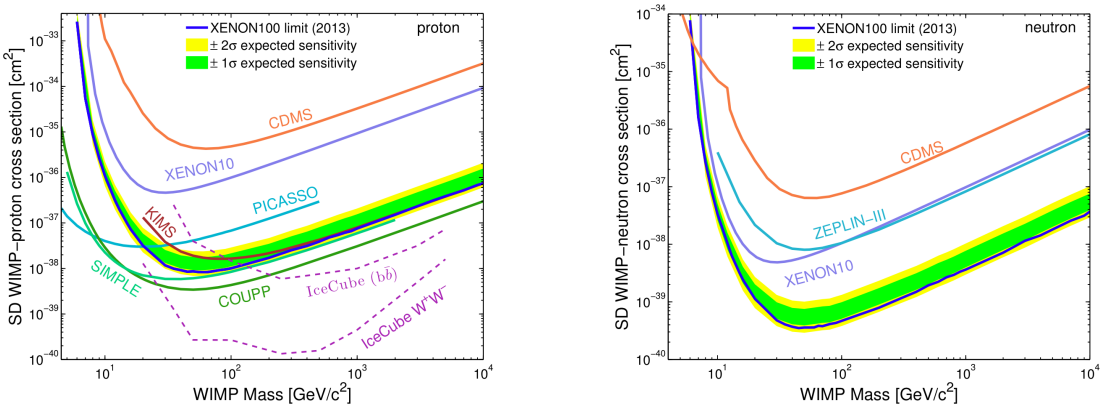

Figure 2.11: Limit of the XENON100 detector from 225 life days for spin dependent coupling on the proton (left) and on the neutron (right). Figures taken from [43].

was measured with a high sensitivity germanium detector. As figure 2.9 shows the measured electronic recoil spectrum is in very good agreement with the spectrum obtained from the Monte Carlo simulation.

Results

The longest and most successful data taking run started in March 2011. Within about one year 225 live days of dark matter search data has been collected. This has led to a limit on the spin-independent elastic WIMP-nucleon scattering for WIMP masses above $8\,\mathrm{GeV/c^2}$, with a minimum cross section of $2 \times 10^{-45}\,\mathrm{cm^2}$ at $55\,\mathrm{GeV/c^2}$ at 90% confidence level (C.L.) [42] (Figure 2.10). On the spin-dependent WIMP-neutron interaction XENON100 could set a limit of $3.5 \times 10^{-40}\,\mathrm{cm^2}$ at a WIMP mass of $45\,\mathrm{GeV/c^2}$ at 90% C.L. [43] (Figure 2.11).

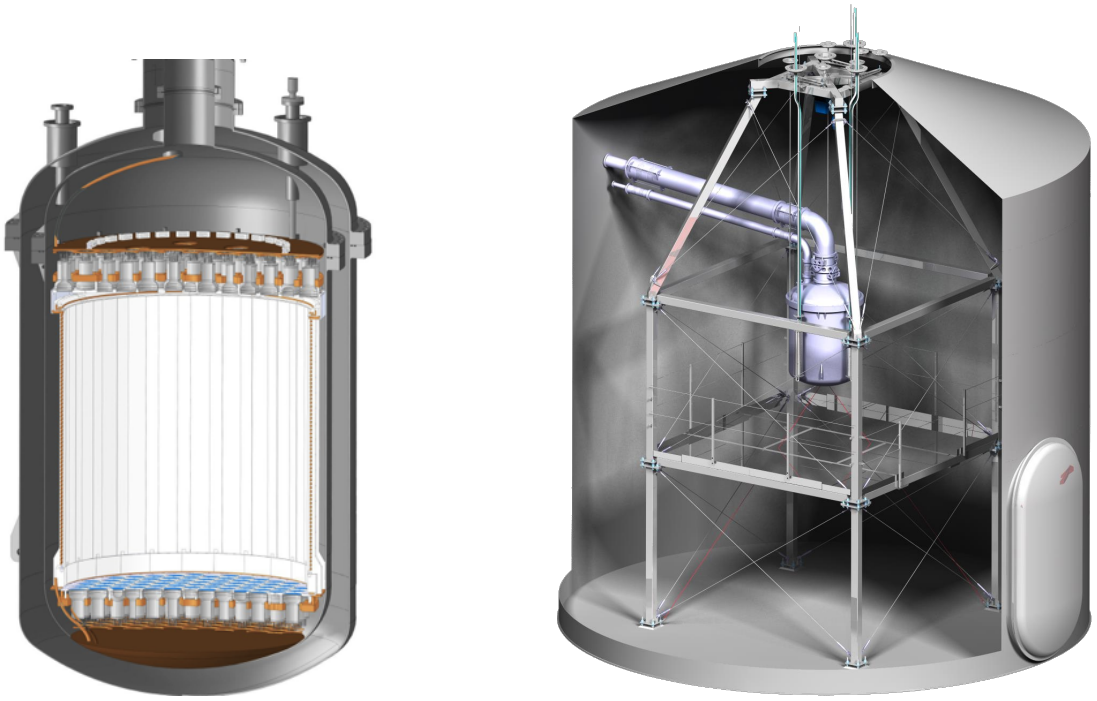

Figure 2.12: Left: sketch of the XENON1T TPC. Figure made by Andreas James. Right: sketch of the watertank. The TPC is located in the center. All required supply (such as liquid xenon, high voltage) runs through pipes that come from a service building next to the water tank. The calibration sources are inserted from above. Figure from the XENON collaboration.

2.2.2 XENON1T

XENON1T [34] is the successor of XENON100. At the time of writing it is in the commissioning phase. The aim of the XENON1T project is to improve the sensitivity by two orders of magnitude compared to XENON100. Therefore, TPC the (figure 2.12, left) was enlarged to a cylinder with a height of 0.95 m and a diameter of 1.05 m. The content of liquid xenon in the target volume is increased to 2 tonnes. The total mass of the liquid xenon is 3.5 tonnes. The expected background was reduced by a factor 100 to $(1.80 \pm 0.15) \cdot 10^{-4} (\mathrm{kg \cdot day \cdot keV})^{-1}$. Aside from increasing the detector size this is achieved through careful selection of low radioactive detector materials and by reducing the radioactive krypton-85 in the xenon down to a level of 0.2 ppt using a distillation column. The XENON1T TPC is equipped with 248 Hamamatsu R11401_21 [68, 69] PMTs, which are designed to have a low radioactivity and for the operation in liquid xenon. 127 PMT are in the top array in the gas phase arranged in concentric circles to optimize the radial resolution in the position reconstruction. 121 PMT are in the bottom

Figure 2.13: Photograph of the XENON1T Experiment. The watertank is on the left, the service building on the right, containing the xenon storage (ground floor), the electronics with the data acquisition and the power supply (second floor) and the cooling system (upper floor). Picture from the XENON collaboration.

array arranged in a hexagonal pattern to achieve optimum packing. 6 R8520 1-inch PMTs are installed in the xenon that surrounds the TPC for diagnostic reasons.

The XENON1T TPC is located in the center of a ∼10 meter diameter water tank that is equipped with 84 8-inch PMTs and acts as a shield and an active Cherenkov muon veto [67]. Next to the water tank an infrastructure building containing the xenon storage and purification system and the DAQ as well as the cryogenic system is situated (figure 2.13). The supply of liquid xenon from the cryogenic system runs through a pipe crossing the watertank. The cables of all PMTs pass this pipe (chapter 4).

After an exposure of 2 years XENON1T will reach a sensitivity of $1.6 \times 10^{-47}\,\mathrm{cm}^2$ on the spin in-independent WIMP-nucleon cross section at a WIMP mass of $50\,\mathrm{GeV/c}^2$ [34].

Many subsystems of the XENON1T experiment are designed such that the experiment can be upgraded to a larger detector, XENONnT, that will contain about 7 tonnes of liquid xenon. It will be installed in the same watertank. The outer cryostat is built such that it can house a TPC with the diameter of 1.4 m. The xenon storage system is designed for a total amount of 7 tonnes, already. The amount of cables installed in the pipe suffices to operate 432 PMTs. This way the detector can be upgraded essentially exchanging the TPC and adding liquid xenon.

The goal of XENONnT is to improve the sensitivity one order of magnitude compared to XENON1T and to exclude a WIMP-nucleon cross section of $1.6 \times 10^{-48}\,\mathrm{cm}^2$ at a WIMP mass

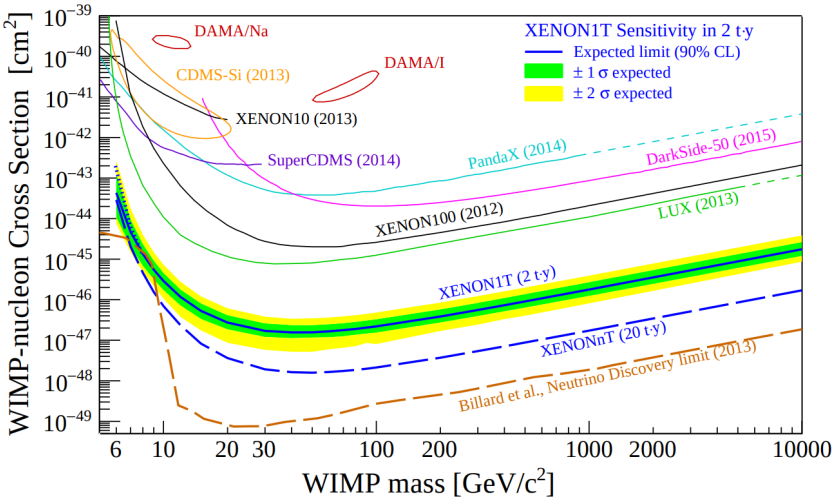

Figure 2.14: Sensitivity of the XENON1T and the XENONnT detector on the spin-independent WIMP-nucleon cross section. Figure taken from [34].

of 50 GeV/c^2. Figure 2.14 shows the expected limits of XENON1T and XENONnT compared to current published limits of other projects.

3

Inelastic WIMP-Nucleon Scattering

An elastic interaction of a WIMP with a xenon nucleus deposits recoil energy inside the TPC. This energy is converted to scintillation light that is measured by PMTs in the top and bottom array of the TPC. An alternative way for direct Dark Matter detection is to observe inelastic WIMP-nucleus scattering, in which the nuclear recoil excites the nucleus to a low-lying excited state [70]:

$$\chi + N \rightarrow \chi + N^* \tag{3.1}$$

$$N^* \rightarrow N + \gamma \tag{3.2}$$

Natural xenon contains the two odd isotopes ^{129}Xe and ^{131}Xe with an abundance of 26.4% and 21.2% respectively, with which this process is possible [44]. The xenon in the XENON100 detector contains 26.2% and 21.8% of ^{129}Xe and ^{131}Xe, respectively [43].

^{129}Xe has an excitation energy of 39.6 keV to the lowest-lying excited state [71]. Since the half-live of the excited ^{129}Xe is only 0.97 ns, the signature of an inelastic event is a nuclear recoil together with an electronic recoil with an energy of 39.6 keV induced by the deexcitation gamma. The excitation energy of ^{131}Xe is 80.2 keV to the lowest-lying state [71]. Its half-live is 0.49 ns.

In this work, the expected recoil spectrum is calculated for the two isotopes ^{129}Xe and ^{131}Xe. The analysis of the XENON100 data will focus on the more sensitive scattering off ^{129}Xe.

3.1 Recoil Spectrum of the Inelastic Process

3.1.1 Kinematics

This chapter will present the allowed energies and velocities, coming from momentum and energy conservation. The momentum conservation requires

$$\vec{p_f} = \vec{p_i} - \vec{q}\,, \tag{3.3}$$

where p_i and p_f are the initial and final momenta of the WIMP and $\vec{q}$ is the momentum transfer to the nucleus. Since the nucleus is in rest before the scattering, the nuclear recoil energy is

$$E_R = \frac{q^2}{2m_A}\,, \tag{3.4}$$

with the mass of the nucleus m_A. The energy conservation requires

$$E_{\mathrm{kin},i} + E_{\mathrm{kin},f} = \frac{p_i^2}{2m_\chi} - \frac{p_f^2}{2m_\chi} = E_R + E^* = \frac{q^2}{2m_A} + E^*\,, \tag{3.5}$$

where $E_{\mathrm{kin},i}$ and $E_{\mathrm{kin},f}$ are the initial and final kinetic energies of the WIMP, E^* is the excitation energy of the nucleus (39.6 keV) and m_χ is the WIMP mass. Putting (3.3) into (3.5) gives

$$\frac{p_i q\cos\theta + q^2}{2m_\chi} = \frac{q^2}{2m_\chi} + E^* \tag{3.6}$$

$$q^2\left(1 + \frac{m_\chi}{m_A}\right) - 2p_i q\cos\theta + 2m_\chi E^* = 0\,, \tag{3.7}$$

where θ is the angle between $\vec{q}$ and $\vec{p_i}$. Using the reduced mass for the WIMP and the nucleus

$$\mu_A = \frac{m_\chi m_A}{m_\chi + m_A} \tag{3.8}$$

one gets a quadratic equation in q

$$q^2 - (2\mu_A v_i\cos\theta)q + 2\mu_A E^* = 0\,, \tag{3.9}$$

where v_i is initial velocity of the WIMP. The solutions for this equation are

$$q = \mu_A v_i\cos\theta\left(1 \pm \sqrt{1 - \frac{2E^*}{\mu_A v_i^2\cos^2\theta}}\right)\,. \tag{3.10}$$

Because the term under the square root has to be positive,

$$\frac{E^*}{\mu_A v_i^2 \cos^2\theta} \leq 1 \Longrightarrow E^* \leq \frac{1}{2}\mu_A v_i^2 \cos^2\theta \tag{3.11}$$

$$\Longrightarrow E^* \leq \frac{1}{2}\mu_A v_i^2 \,. \tag{3.12}$$

Solving eq. (3.9) for the velocity v_i leads to a minimum velocity v_{min} for which the inelastic scattering can occur.

$$v_i = \frac{1}{\cos\theta}\left(\frac{q}{2\mu_A} + \frac{E^*}{q}\right) \Longrightarrow v_{\text{min}} = \frac{q}{2\mu_A} + \frac{E^*}{q} \tag{3.13}$$

The minimum and maximum momentum transfer is given by $\cos\theta = \pm 1$.

$$q_{\text{max, min}} = \mu_A v_i \left(1 \pm \sqrt{1 - \frac{2E^*}{\mu_A v_i^2}}\right) \tag{3.14}$$

The minimum and maximum recoil energy can be obtained with eq. (3.4).

$$E_{R,\text{max, min}} = \frac{\mu_A^2 v_i^2}{2m_A}\left(1 \pm \sqrt{1 - \frac{2E^*}{\mu_A v_i^2}}\right)^2 \tag{3.15}$$

Setting the mass of the xenon nucleus $m_A = 120\,\text{GeV/c}^2$, an example WIMP mass of $m_\chi = 100\,\text{GeV/c}^2$ and a maximal possible initial WIMP velocity in the earth's rest frame of $v_i = v_E + v_{esc} = 232\,\frac{\text{km}}{\text{s}} + 544\,\frac{\text{km}}{\text{s}} = 776\,\frac{\text{km}}{\text{s}} = 2.59 \cdot 10^{-3} c$ into the equation, we get a maximum recoil energy for ^{129}Xe of:

$$\mu_A = 54.55\,\frac{\text{GeV}}{\text{c}^2} \tag{3.16}$$

$$E_{R,\text{max}} = \frac{\mu_A^2 v_i^2}{2m_A}\left(1 + \sqrt{1 - \frac{2E^*}{\mu_A v_i^2}}\right)^2 = 285\,\text{keV}\,. \tag{3.17}$$

Table 3.1 shows the minimum and the maximum recoil energies for different WIMP masses for the nuclei ^{129}Xe ($E^* = 39.6\,\text{keV}$) and ^{131}Xe ($E^* = 80.2\,\text{keV}$)

3.1.2 Recoil Spectrum for Spin Independent Elastic Recoils

This section follows the PhD thesis of Sebastian Arrenberg [73]. First the spin independent elastic recoil spectrum will be discussed before introducing the spin dependent inelastic one.

	^{129}Xe		^{131}Xe	
m_χ (GeV/c^2)	$E_{R,\min}$ (keV)	$E_{R,\max}$ (keV)	$E_{R,\min}$ (keV)	$E_{R,\max}$ (keV)
10	—	—	—	—
25	1.5	31	—	—
50	1.2	110	6.8	81
100	1.1	285	5.4	244
250	1.1	659	4.9	601
500	1.1	954	4.7	885

Table 3.1: The minimum and the maximum energy of the recoil spectrum for different WIMP masses for the nuclei ^{129}Xe and ^{131}Xe. WIMPs with a mass of 10 GeV and lower cannot induce inelastic events with one of the two isotopes.

The recoil spectrum for spin independent elastic scattering is given in [72] as

$$\frac{dR}{dE_R} = \frac{\sigma_0 \rho_\chi}{\sqrt{\pi} v_0 m_\chi \mu_A^2} F^2(E_R)\, T(E_R)\,, \tag{3.18}$$

where σ_0 is the *zero momentum transfer* cross section (i.e. without taking into account form factors) for the nucleus, ρ_χ is the mean dark matter mass density in the halo of our galaxy and v_0 is the mean WIMP velocity. The dimensionless quantity

$$T(E_R) = \frac{\sqrt{\pi}}{2} v_0 \int_{v_{\min}}^{v_{\max}} \frac{f(v)}{v}\, dv \tag{3.19}$$

absorbs the integrals over the velocity distribution of the dark matter particles. $v_{\min}$ is the minimum velocity for a WIMP to induce an elastic recoil with the energy E_R [54]:

$$v_{\min} = \sqrt{\frac{E_R m_A}{2\mu_A^2}}\,. \tag{3.20}$$

$v_{\max}$ is the escape velocity of the of the galaxy v_{esc}.

Assuming a Maxwellian velocity distribution that is truncated at the escape velocity v_{esc}

$$f(v, v_E) = k \begin{cases} e^{-(v+v_E)^2/v_0^2} & \text{for } |v + v_E| < v_{esc} \\ 0 & \text{for } |v + v_E| \geq v_{esc} \end{cases}\,, \tag{3.21}$$

with an average velocity of the earth v_E and a normalization factor k, there are different solutions for three different ranges of $v_{\min}$ [73]:

$$T(E_R) = \begin{cases} \frac{k_0}{k_1}\left\{\frac{\sqrt{\pi}}{4}\frac{v_0}{v_E}\left[\mathrm{erf}\left(\frac{v_{\min}+v_E}{v_0}\right) - \mathrm{erf}\left(\frac{v_{\min}-v_E}{v_0}\right)\right] - \exp\left(-\frac{v_{\mathrm{esc}}^2}{v_0^2}\right)\right\}, \\ \qquad\qquad \text{if } 0 \le v_{\min} \le v_{\mathrm{esc}} - v_E \\ \frac{k_0}{k_1}\frac{1}{2v_E}\left\{\frac{\sqrt{\pi}\cdot v_0}{2}\left[\mathrm{erf}\left(\frac{v_{\mathrm{esc}}}{v_0}\right) - \mathrm{erf}\left(\frac{v_{\min}-v_E}{v_0}\right)\right]\right. \\ \qquad \left. -(v_{\mathrm{esc}} + v_E - v_{\min})\cdot\exp\left(-\frac{v_{\mathrm{esc}}^2}{v_0^2}\right)\right\}, \\ \qquad\qquad \text{if } v_{\mathrm{esc}} - v_E \le v_{\min} \le v_{\mathrm{esc}} + v_E \\ 0\,, \qquad\qquad \text{if } v_{\mathrm{esc}} + v_E \le v_{\min} \end{cases} \tag{3.22}$$

Here $\frac{k_0}{k_1}$ is the normalization constant for the velocity distribution. For a Maxwellian dark matter velocity distribution and an infinite escape velocity $v_{esc} = \infty$

$$k_0 = (\pi v_0^2)^{3/2}\,. \tag{3.23}$$

When the distribution is truncated at $|v + v_E| = v_{esc}$ the normalization factor becomes

$$k_1 = k_0\left[\mathrm{erf}\left(\frac{v_{esc}}{v_0}\right) - \frac{2}{\sqrt{\pi}}\frac{v_{esc}}{v_0}\exp\left(-\frac{v_{\mathrm{esc}}^2}{v_0^2}\right)\right]\,. \tag{3.24}$$

Elastic Form Factors

The form factor $F^2(E_R)$ is given by [72] parametrized as

$$F(E_R) = 3\cdot\frac{\sin(qr_n)/(qr_n)^2 - \cos(qr_n)/(qr_n)}{qr_n}\cdot\exp\left[-(q\cdot s)^2\right]\,. \tag{3.25}$$

r_n is

$$r_n = \sqrt{(r_0 - .6)^2 + \frac{7}{3}(0.52\pi)^2 - 5s^2}\,, \tag{3.26}$$

with $s = 0.9\,\mathrm{fm}$ and $r_0 = 1.2\,\mathrm{fm}\cdot A^{1/3}$ taken from [54]. More recent calculations [74] agree on the simple parametrization in the low energy area which is important for the inelastic analysis.

Figure 3.1 shows the elastic recoil spectrum for spin independent WIMP interactions with xenon for the WIMP masses of 10 GeV, 50 GeV, 100 GeV and 500 GeV. For the detector material only ^{129}Xe is taken into account since this is the isotope for which the inelastic events occur which are analyzed here. The following numbers are assumed: the dark matter density $\rho_\chi = 0.4\,\mathrm{GeV/cm^3}$, the WIMP-nucleon cross section $\sigma_0 = 10^{-45}\,\mathrm{cm^2}$, the mean WIMP velocity $v_0 =$

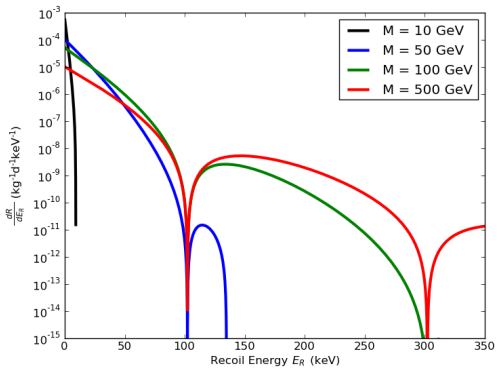

Figure 3.1: Differential recoil spectrum for four different WIMP masses for spin independent elastic scattering on ^{129}Xe.

220 km/s, the escape velocity in our galaxy $v_{\text{esc}} = 544$ km/s and the mean velocity of the earth in the galaxy $v_E = 232$ km/s.

3.1.3 Inelastic Scattering

Inelastic Spin Independent Scattering

To induce an inelastic event, the WIMP is required to have a minimal energy to be enable to excite the nucleus to a state with an excitation energy of $E^* = 39.6$ keV

$$v_{\text{min}} = \frac{q}{2\mu_A} + \frac{E^*}{q}\,, \tag{3.27}$$

as deducted in section 3.1.1. The first summand is identical to the minimal velocity in the elastic scattering (eq. 3.20); the second part comes from the excitation of the nucleus. The difference between the minimal velocity to induce an elastic recoil and an inelastic recoil for ^{129}Xe is shown in figure 3.2. For higher recoil energies the minimum velocity of the inelastic scattering approaches the one for elastic scattering as the excitation energy becomes more and more negligible.

Figure 3.3 shows the recoil spectrum for inelastic scattering with the minimal velocity (eq. 3.27). The spectrum of the 10 GeV WIMP disappears from this scale. The spectrum for the other WIMP masses drops for recoil energies near zero.

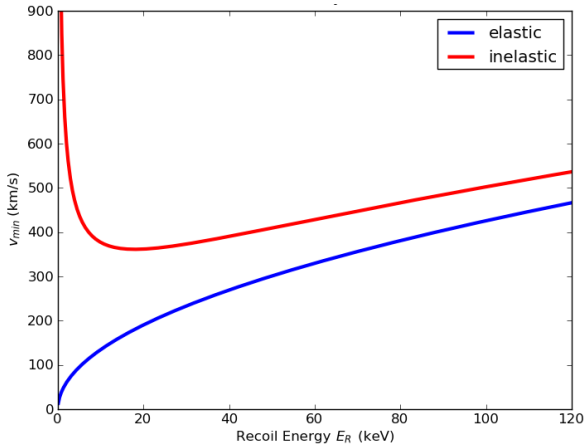

Figure 3.2: The minimum velocity to induce a nuclear recoil for elastic (blue) and inelastic (red) scattering.

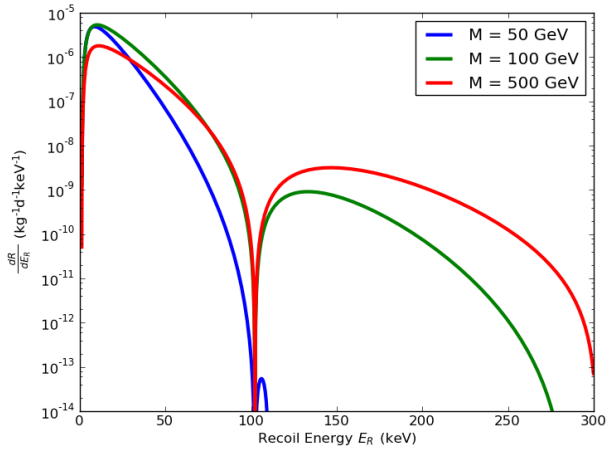

Figure 3.3: Recoil spectrum for inelastic scattering for spin independent interaction. The 10 GeV WIMP that occurs in figure 3.1 does not induce an inelastic recoil.

Spin Dependent Form Factors

The spin-dependent cross section for a nucleon is [43]

$$\sigma_n(q) = \frac{3}{4}\frac{\mu_n^2}{\mu_A^2}\frac{2\mathcal{J}+1}{\pi}\frac{\sigma_{SD}(q)}{S_A^{a_0=a\pm a_1}(q)}\,, \tag{3.28}$$

where σ_{SD} is the total WIMP-nucleus cross section, μ_A and μ_n are the WIMP-nucleus and WIMP-nucleon reduced masses, respectively and $\mathcal{J}$ the spin of the nucleus and with

$$S_A(0) = \frac{(2\mathcal{J}+1)(\mathcal{J}+1)}{\pi\mathcal{J}}\left[a_p\left\langle S_p\right\rangle + a_n\left\langle S_n\right\rangle\right], \tag{3.29}$$

where $\langle S_{p,n}\rangle = \langle\mathcal{J}|\hat{S}_{p,n}|\mathcal{J}\rangle$ are the expectation values of the proton and neutron spin operator. Hence the cross section of the WIMP and the nucleus is

$$\sigma_{\mathrm{SD}} = \frac{4}{3}\cdot\sigma_n\cdot\frac{\mu_A^2}{\mu_n^2}\cdot\frac{\pi}{2\mathcal{J}+1}S(q)\,. \tag{3.30}$$

According to [54] the total event rate per unit mass is

$$R = R_0\frac{k_0}{k}\frac{1}{4\pi v_0^2}\int_{v_{\min}}^{v_{\max}} v f(v, v_E)\,d^3v \tag{3.31}$$

and the differential rate

$$\frac{dR}{dE_R} = \frac{R_0}{E_0 r}\frac{k_0}{k}\frac{1}{2\pi v_0^2}\int_{v_{\min}}^{v_{\max}}\frac{1}{v}f(v, v_E)\,d^3v, \tag{3.32}$$

with

$$r = \frac{4m_\chi m_A}{(m_\chi + m_A)^2} \tag{3.33}$$

and the rate per unit mass for $v_E = 0$ and $v_{\mathrm{esc}} = \infty$

$$R_0 = \frac{2}{\sqrt{\pi}}\frac{N_0}{A}\frac{\rho_\chi}{m_\chi}\sigma_0 v_0 = 361\,\mathrm{events}/(\mathrm{kg}\cdot\mathrm{d})\,, \tag{3.34}$$

where N_0 is the Avogadro constant, A the atomic mass and σ_0 is the *zero momentum transfer* cross section for a nucleon. $\frac{k_0}{k}$ is defined in section 3.1.2 on page 27. Hence, the recoil spectrum

is calculated as:

$$\frac{dR}{dE_R} = \frac{T(E_R)}{E_0 r} \cdot S(q) \frac{R_0}{m_\chi m_A} \tag{3.35}$$

$$\times \left(\frac{\sigma_0}{10^{-36}\,\mathrm{cm}^2} \right) \left(\frac{\rho_\chi}{0.4\,\mathrm{GeV}c^{-2}\mathrm{cm}^{-3}} \right) \left(\frac{v_0}{230\,\mathrm{km\,s}^{-1}} \right) . \tag{3.36}$$

The masses of the WIMP and the nucleus m_χ and m_A are given in GeV, the dark matter density ρ_χ is given in $\mathrm{GeV}c^{-2}\mathrm{cm}^{-3}$ and the mean WIMP velocity v_0 is given in $\mathrm{km\,s}^{-1}$. The mean WIMP energy is given by

$$E_0 = \frac{1}{2} m_\chi v_0^2 . \tag{3.37}$$

Structure Functions

The structure functions in eq. (3.30) are parameterized via an exponential term multiplied by a polynomial

$$S_{p/n} = \exp(-y) \cdot \sum_{i=0}^{9} c_i \cdot y^i , \tag{3.38}$$

where

$$y = \frac{p^2 b^2}{2\hbar^2} \tag{3.39}$$

and the harmonic-oscillator length b is a constant for the nucleus b = 2.2853 fm for ^{129}Xe. The coefficients are calculated in [70]. There are one-body current interaction (1bc) in which the currents of all nucleons in the nucleus are summed, similar as in [75]. Additionally to that the model in [70] takes two-body currents into account (1+2bc), where WIMPs couple to two nucleons simultaneously. 2bc introduce theoretical uncertainties into the model. Hence for the recoil spectra the maximum and the minimum are shown for 1+2bc interactions.

Figure 3.4 (left) shows the pure neutron interaction with ^{129}Xe for the 1bc and for the maximum and minimum of the 1+2bc for a WIMP with a mass of 100 GeV. The maximum recoil energy in this spectrum is 284.8 keV. This is the expected value (see table 3.1 or eq. (3.17)). Figure 3.4 (right) compares the mean of the 1+2bc (between the minimum and maximum) spectra for pure neutron interaction for the three different WIMP masses 50 GeV, 100 GeV and 500 GeV. Figure 3.5 shows the recoil spectra for a 100 GeV WIMP pure neutron interaction for elastic (for ^{129}Xe and ^{131}Xe) and inelastic scattering (for ^{129}Xe and ^{131}Xe).

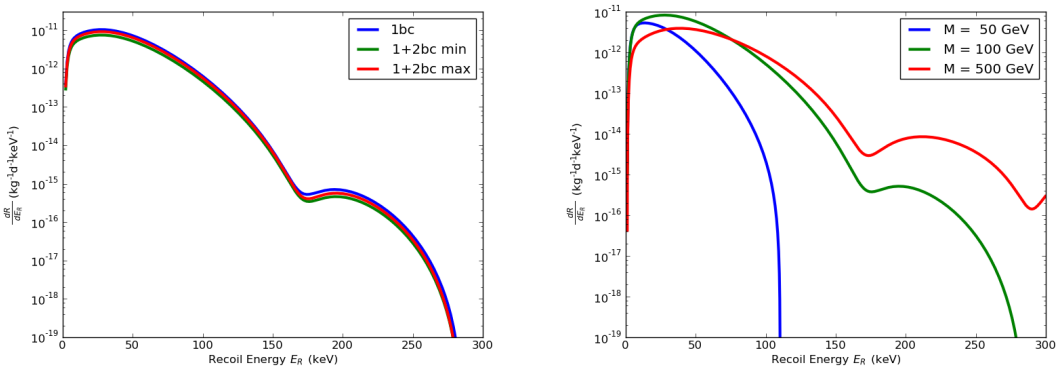

Figure 3.4: Left: Pure neutron interaction with ^{129}Xe for the 1bc (blue) and for the maximum and minimum 1+2bc (green and red respectively) for a WIMP with a mass of 100 GeV. Right: Mean value for neutron interaction with ^{129}Xe for the 1+2 body current for a WIMP with a mass of 50 GeV (blue), 100 GeV (green) and 500 GeV (red).

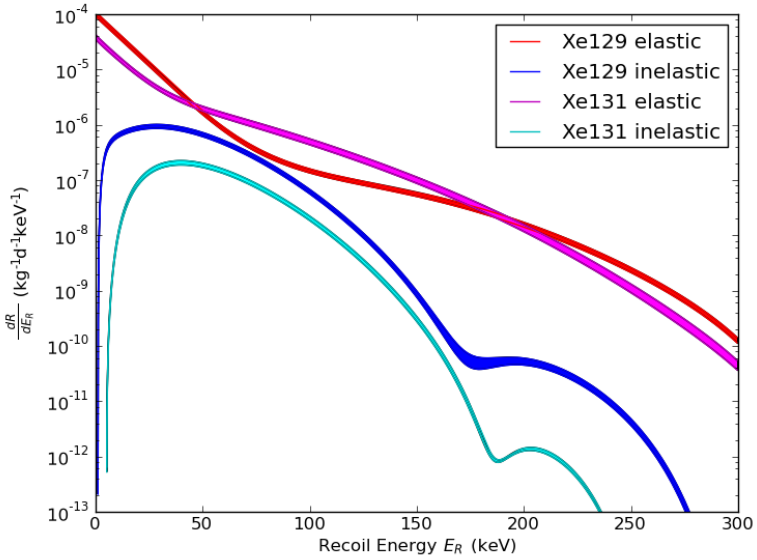

Figure 3.5: Recoil spectra for a 100 GeV WIMP pure neutron interaction for elastic and inelastic scattering for the two isotopes ^{129}Xe and ^{131}Xe. The reddish curves describe the elastic scattering (red for ^{129}Xe and magenta for ^{131}Xe) and the blueish curves are the inelastic scattering (blue for ^{129}Xe and cyan for ^{131}Xe).

3.1.4 Combining Electronic Recoil and Nuclear Recoil

The ionization density is higher for nuclear recoils than for electronic recoils. In contrast to an electronic recoil, for a nuclear recoil a large fraction of the recoil energy is converted into heat (quenching). For that fraction neither photons are emitted nor free electrons are produced. The fraction of the recoil energy converted into scintillation light is hence smaller [53]. Therefore, the conversion from recoil energy to the direct scintillation signal S1 or proportional charge signal S2 has to be modified by quenching factors for nuclear recoils. Vice versa, signals created in xenon refer to different energy scales, depending whether they are originated from an electronic or a nuclear recoil. Therefore, we mark the energies calculated from different kind of signals differently: Energies obtained from a nuclear recoil signal will be declared with a subscript "nr" (i.e. R_{nr} or E_{nr}) and will carry the unit $\mathrm{keV_{nr}}$ (standing for *nuclear recoil equivalent*), whereas the symbols for energies obtained from an electronic recoil signal will be provided with the subscript "er" (i.e. R_{er} or E_{er}) and their units will be $\mathrm{keV_{ee}}$ (standing for *electron equivalent*).

To combine the electronic recoil spectrum of the 40 keV gamma and the spectrum for the inelastic nuclear recoil both spectra have to be transformed into the same energy space. Therefore the combined recoil spectrum is calculated for the S1 signal and for the S2 signal individually.

Nuclear Recoil Spectra for the S1 Signal

For the nuclear recoil the energy is given by

$$E_{nr} = \frac{S1}{L_y}\frac{1}{\mathcal{L}_{\mathrm{eff}}(E)}\frac{S_{ee}}{S_{nr}}\,. \tag{3.40}$$

The light yield L_y is measured for a reference γ-line at 122 keV in photoelectrons (PE) per $\mathrm{keV_{ee}}$. It depends on the drift field in the detector. $\mathcal{L}_{\mathrm{eff}}(E)$ is the relative scintillation yield of nuclear recoils as described in section 2.1.2. The field suppression factors S_{ee} and S_{nr} reduce the light yield due to the quenching for electronic recoils and nuclear recoils, respectively [76]. At a drift field of 0.53 kV/cm they are [64]:

$$S_{ee} = 0.58\,, \tag{3.41}$$

$$S_{nr} = 0.95\,, \tag{3.42}$$

$$L_y = (2.28 \pm 0.04)\frac{\mathrm{PE}}{\mathrm{keV_{ee}}}\,. \tag{3.43}$$

Hence the size of the S1 signal is given by

$$S1_{\mathrm{nr}}(E) = L_y \cdot \frac{S_{nr}}{S_{ee}} \cdot E \cdot \mathcal{L}_{\mathrm{eff}}(E) = 3.73 \cdot E \cdot \mathcal{L}_{\mathrm{eff}}(E)\,. \tag{3.44}$$

The spectrum itself is written as:

$$\frac{dR_{\mathrm{nr}}}{dE_R} = \frac{dR_{\mathrm{nr}}}{dS1}\frac{dS1}{dE_R} \tag{3.45}$$

and transformed by multiplying it with the factor $\frac{dE_R}{dS1}$:

$$\frac{dR_{\mathrm{nr}}}{dS1} = \frac{dR_{\mathrm{nr}}}{dE_R} \cdot \frac{dE_R}{dS1} = \frac{dR_{\mathrm{nr}}}{dE_R} \cdot \left(\frac{1}{3.73 \cdot \mathcal{L}_{\mathrm{eff}}(E_R)} - \frac{E_{\mathrm{nr}}}{3.73 \cdot \mathcal{L}^2_{\mathrm{eff}}(E_R)} \frac{d\mathcal{L}_{\mathrm{eff}}(E_R)}{dE_R} \right)\,. \tag{3.46}$$

Converting Electronic Recoil in S1 Signal

The energy resolution of the XENON100 detector for the S1 signal of the 36.9 keV line is [33]

$$\frac{\sigma}{E} = (15.8 \pm 0.2)\%\,. \tag{3.47}$$

The electronic recoil signal is modeled by a Gaussian function with

$$\mu = 39.6\,\mathrm{keV}\,, \tag{3.48}$$

$$\sigma = (15.8\% \times 39.6)\,\mathrm{keV} = 6.257\,\mathrm{keV}\,. \tag{3.49}$$

The rate for electronic recoils is hence given by

$$\frac{dR_{\mathrm{er}}}{dE_R} = A \cdot \exp\left(-\frac{1}{2}\frac{(E-\mu)^2}{\sigma^2} \right)\,. \tag{3.50}$$

The distribution was scaled such that the integral over the Gaussian function is the same as the integral of the curve describing the nuclear recoil

$$I = \int \left(\frac{dR_{\mathrm{nr}}}{dE_R} \right) dE_R \tag{3.51}$$

since for every nuclear recoil event there is exactly one electronic event and hence the integrated rates R_{nr} and R_{er} must be the same. This leads to the factor

$$A = \frac{I}{\sqrt{2\pi}\sigma}\,. \tag{3.52}$$

The light yield for the electronic recoil for the 36.9 keV line was read out from figure 22 of [33] as

$$L_y = 2.7 \frac{\mathrm{PE}}{\mathrm{keV_{ee}}} . \tag{3.53}$$

Hence the S1 signal for an electronic recoil is

$$S1_{\mathrm{er}} = E \cdot 2.7 \frac{\mathrm{PE}}{\mathrm{keV_{ee}}} . \tag{3.54}$$

Since in this case the transformation from E_{er} to $S1$ is linear in E_{er} it is simply

$$\frac{dR_{\mathrm{er}}}{dS1} = \frac{dR_{\mathrm{er}}}{dE_R} \cdot \frac{dE_R}{dS1} = \frac{dR_{\mathrm{er}}}{dE_R} \cdot \frac{1}{2.7} . \tag{3.55}$$

The S1 Spectrum

If $f(x)$ and $g(x)$ are the S1 distributions of the nuclear recoils and the electronic recoils, respectively, the probability to get an event with S1 that is the sum of the energies of both kinds of recoil is

$$\int_{x,y,x+y=S1} f(x)g(y)dxdy. \tag{3.56}$$

Hence (substituting $y = x_0 - x$) the distribution of the sum of the energies distributed by their individual distributions is the convolution of the two functions. Since the integral of a convolution of two functions is the product of the individual integrals, the spectrum has to be divided by the integral of one of the curves. (Hence in fact the normalization of the energy distribution of the gamma does not matter.) The total S1 distribution is then

$$F(x_0) = \frac{1}{I} \int_{x=0}^{x_{\max}} f(x)g(x_0 - x)dx. \tag{3.57}$$

The curve in figure 3.6 (left) shows the combination of the nuclear recoil for a 100 GeV WIMP and the 40 keV gamma that is emitted via deexcitation. Figure 3.6 (right) shows the combination of the nuclear recoil and the 40 keV gamma for the four different WIMP masses 50 GeV, 100 GeV, 500 GeV and 5000 GeV.

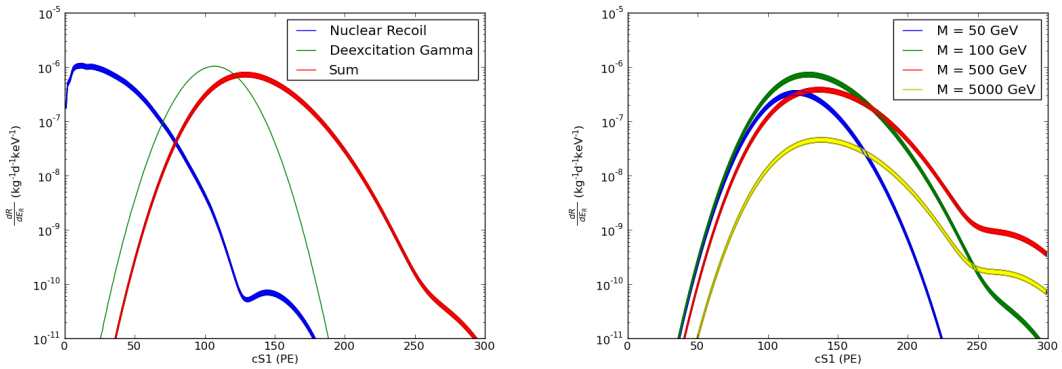

Figure 3.6: Left: The inelastic recoil spectrum for 1+2bc for ^{129}Xe neutron interaction (blue) plus the Gaussian distributed gamma energy (green) gives the total recoil spectrum converted in S1 (red). Right: The total inelastic recoil spectrum for 1+2bc for ^{129}Xe neutron interaction for WIMPs with the masses of 50 GeV (blue), 100 GeV (green), 500 GeV (red) and 5000 GeV (yellow).

Nuclear Recoils in S2

Converting the nuclear recoil energy to S2 the same formalism as above is just except the formula for S2 is [58]

$$E_{\mathrm{nr}} = \frac{S2}{Y}\frac{1}{Q_Y(E)}\,, \tag{3.58}$$

where $Y = 19.5\,\frac{\mathrm{PE}}{e^-}$ is the secondary amplification factor.

Electronic recoils in S2

For electronic recoil, the S2 signal is calculated by the total number of electrons created by that gamma, which can be obtained by [53]

$$E_{\mathrm{er}} = \varepsilon(n_\gamma + n_e)\,, \tag{3.59}$$

with

$$\varepsilon = (13.7 \pm 0.2)\,\mathrm{eV}\,. \tag{3.60}$$

For a drift field of 530 kV/cm we take from NEST [77, 78] the photon yield for the 36.9 keV gamma, 45.45 photons per keV. Hence

$$n_\gamma = 45.45 \cdot 39.6 = 1800\,\mathrm{photons}\,. \tag{3.61}$$

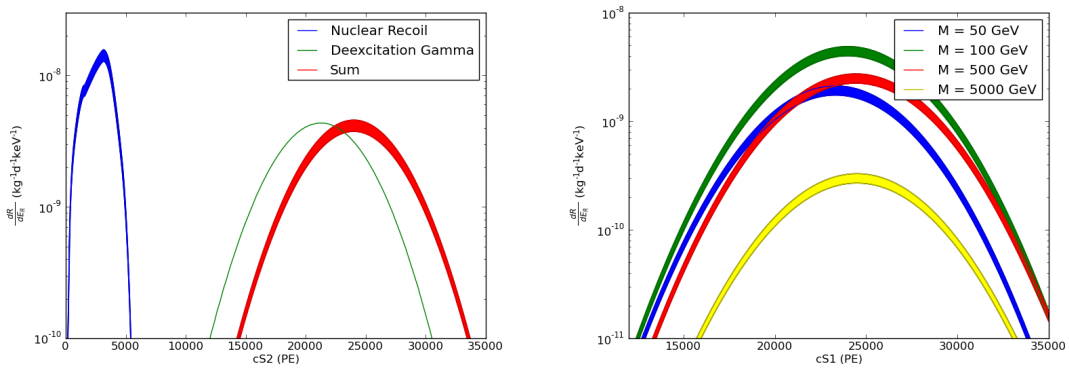

Figure 3.7: Left: The inelastic recoil spectrum for 1+2 body current for ^{129}Xe neutron interaction (blue curve) plus the Gaussian distributed gamma energy (green curve) gives the total recoil spectrum (red curve). Right: The total inelastic recoil spectrum for 1+2 body current for ^{129}Xe neutron interaction for WIMPs with the masses of 50 GeV (blue), 100 GeV (green), 500 GeV (red) and 5000 GeV (yellow).

We can thus determine the number of electrons as

$$n_e = \frac{E_{\text{er}}}{\varepsilon} - n_\gamma = \frac{39.6}{0.0137} - 1800 = 2890 - 1800 = 1090\,. \tag{3.62}$$

This results in a peak at

$$S2 = n_e \cdot Y = 1090 \cdot 19.5\,\text{PE} = 21\,255\,\text{PE}\,. \tag{3.63}$$

Combining these two spectra works equally as for the S1 signal. The results are shown in figure 3.7 (left), the combined spectrum together with the nuclear recoil spectrum for a 100 GeV WIMP and the 36.9 keV gamma and in figure 3.7 (right) for the four different WIMP masses 50 GeV, 100 GeV, 500 GeV and 5000 GeV.

Transforming Nuclear Recoil into Electronic Recoil Energy

By using the relation

$$\frac{dR}{dE_{\text{er}}} = \frac{dR}{dE_{\text{nr}}}\frac{dE_{\text{nr}}}{dE_{\text{er}}}\,, \tag{3.64}$$

the nuclear recoil spectrum can be transformed to the electronic recoil space (keV$_{\text{ee}}$). Figure 3.8 shows the combination of the transformed nuclear recoil for a 100 GeV WIMP and the 36.9 keV gamma that is emitted via deexcitation.

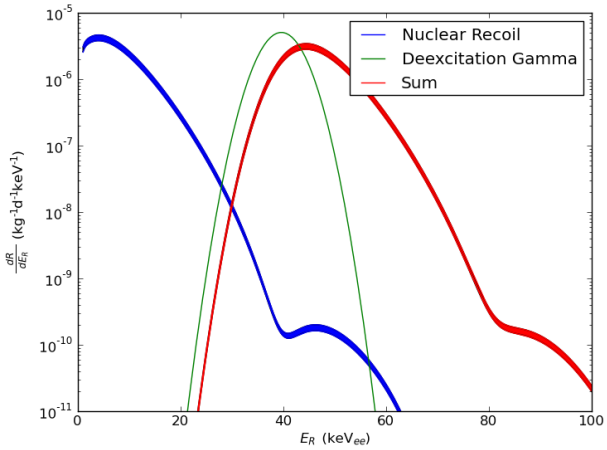

Figure 3.8: The total inelastic nuclear recoil spectrum for 1+2bc for ^{129}Xe neutron interaction for WIMPs with the mass of 100 GeV (red), the recoil spectrum of a 36.9 keV gamma (green) and the total recoil spectrum (blue).

3.1.5 Integrated Spectra

A detector with an energy threshold E_{th} measures an integrated number of events of

$$R_{\text{int}}(E_{\text{th}}) = \int_{E_{\text{th}}}^{\infty} \frac{dR}{dE'_R} dE'_R \,. \tag{3.65}$$

Figure 3.9 shows the integrated spectra for elastic and inelastic scatter events for both ^{129}Xe and ^{131}Xe for an example WIMP with a mass of 100 GeV. The figure contains also the sum of both elastic inelastic spectra, as well as the total spectrum containing the elastic and inelastic events. For these plots the nuclear recoil spectrum is transformed to electronic recoil energies.

The right graph of the figure 3.9 shows a zoomed view of the left one. There it can be seen that for detectors with a low energy threshold the elastic events have a much higher rate than the inelastic events. However, there is a threshold energy, at which the inelastic events are dominant over the elastic ones.

Table 3.2 shows the energy at which the inelastic spectrum starts do dominate over the elastic spectrum for the isotopes ^{129}Xe and ^{131}Xe individually and the composition of both isotopes for various WIMP masses.

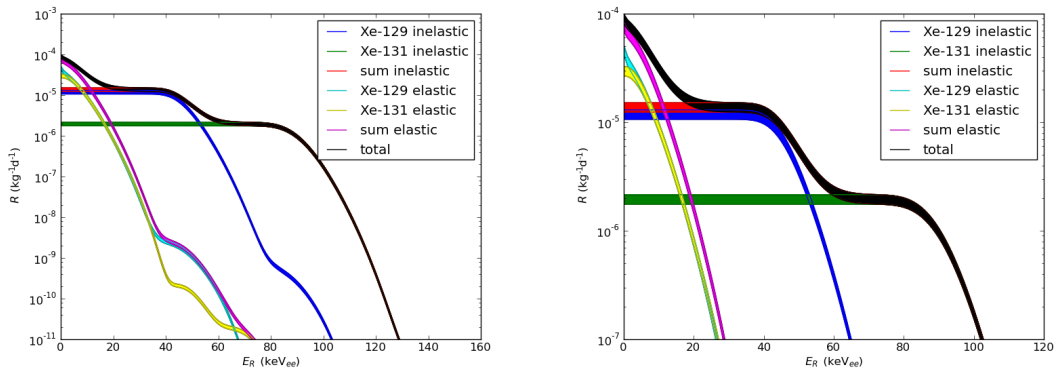

Figure 3.9: The integrated recoil spectrum for 1+2 body current for neutron interaction for WIMPs with the mass of 100 GeV in terms of electronic recoil (ER) energy keV_{ee} for the elastic scattering of ^{129}Xe (cyan), ^{131}Xe (yellow) and their sum (magenta) as well as for inelastic scattering of ^{129}Xe (blue), ^{131}Xe (green) and their sum (red). The black curve show the total integrated recoil spectrum for elastic and inelastic scattering for both isotopes. The right picture is a detailed view of the left picture.

m_χ (GeV)	E_{dom} (keV) for ^{129}Xe	E_{dom} (keV) for ^{131}Xe	E_{dom} (keV) for both isotopes	P_{dom} (MeV/c) for both isotopes
10	—	—	—	—
25	5	—	5	36
50	7	17	9	45
100	7	24	12	54
250	9	32	19	68
500	11	35	24	75

Table 3.2: Energy in keV at which the inelastic recoil spectrum starts to dominate over the elastic recoil spectrum for the isotopes ^{129}Xe and ^{131}Xe separately as well as for the combination and the corresponding momentum transfer energy for the combined detector materials.

3.1.6 Conclusion

In this section the expected interaction rate of WIMPs for liquid xenon detectors via inelastic scattering (eq. 3.2) was calculated for the two isotopes ^{129}Xe and ^{131}Xe. It was compared to the expected rate of the elastic spin-dependent scattering process. For momentum transfers close to zero the elastic rate is considerably higher than the inelastic one (for a WIMP mass of 100 GeV for about a factor 5). However, for higher momentum transfers the inelastic channel starts to dominate over the elastic one. (For a WIMP mass of 100 GeV the threshold is at 54 MeV/c, see table 3.2.) Whereas experiments that search for elastic interactions put a lot of effort to reach a low energy threshold due to the exponential decrease of the recoil spectrum, experiments with a higher energy threshold have the opportunity to search for dark matter via the inelastic channel. Furthermore, the inelastic channel could be used to probe the nature the WIMP-nucleon interaction. An observation in both channels, the elastic and the inelastic one, would indicate that the WIMP interaction in a spin-dependent way with the nucleon. The following sections show the search for inelastic events in the XENON100 data that has been recorded in between March 2011 and April 2012.

3.2 Analysis of XENON100 Data

The longest dark matter run of the XENON100 detector started in March 2011. 225 life days of data were taken during 13 month. This run led to the to date most sensitive results created by the XENON project. It was used to publish the spin independent [42] and spin dependent [43] elastic scattering results. The analysis is described in [76]. Compared to previous runs the intrinsic background of ^{85}Kr was considerably reduced by cryogenic distillation of the xenon. The total fraction of krypton was lowered to (19 ± 4) ppt [42]. To calibrate the electronic recoil (ER) background ^{60}Co and ^{232}Th sources were employed. The calibration of the nuclear recoil (NR) response consists of data taken from an AmBe neutron source.

This section describes the data and event selection of this run for the analysis that is presented. The following sections will describe two different ways to analyze the inelastic events in this run. The analysis presented in section 3.3 exploits the fact that inelastic events introduce an asymmetry into the ER background distribution due to their nuclear recoil component and an asymmetry parameter is defined. The calibration data set from the AmBe neutron source was taken for the prediction of the distribution of the signal events. Differences in the subdominant energy content of the event originated by nuclear recoil for different WIMP masses were neglected for this analysis. Section 3.4 will present a count based analysis. This analysis contains a simulation of inelastic interactions in the detector to predict the distribution of signal events. The simulation was compared to the NR spectrum from the AmBe neutron source calibration. Both analyses employ the ^{60}Co and ^{232}Th ER calibration source to create a background prediction. The signal region was blinded until the analysis principle was finalized in both cases. After unblinding the measured events were compared with the background prediction.

3.2.1 Selecting the Energy Region of Inelastic Events

For the spin independent scattering the analysis regions extends from recoil energies between 6.6 and 43.3 keV$_{\mathrm{nr}}$. In the measurement the integrated area of the S1 signal is taken to determine the energy of every event. The energy boundaries of the analysis region correspond to S1 signal of 3 or 30 photoelectrons (PEs), respectively. Events originated from an inelastic scattering interaction induce S1 signals of roughly 80 to 150 PEs. The analysis uses an energy region of S1 between 40 and 200 PEs. This corresponds to an energy region of about 10 to 75 keV$_{\mathrm{ee}}$. Therefore the event selection cuts from the elastic analyses were checked for their applicability and necessity for the higher energies of the inelastic scattering. Cuts that failed these checks were modified or redefined.

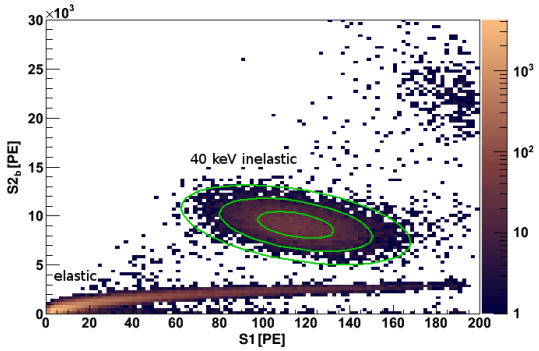

Figure 3.10: Inelastic events region fit with a two-dimensional Gaussian (green ellipses) for the anti-correlated charge proportional light signal S2 and the direct scintillation light S1. On the bottom are the elastic events; on the top right a part of the inelastic events coming from ^{131}Xe.

Figure 3.10 shows the calibration data taken with an AmBe neutron source over an S1 range from 0 to 200 PEs. The horizontal band at the bottom with an S2 smaller than 4000 PEs are the neutrons scattering off elastically in the xenon. The neutrons scattering inelastically off the ^{129}Xe create the 36.9 keV line. This line is indicated with green ellipses showing the 1-σ, 2-σ and 3-σ lines of the two-dimensional distribution. At higher energies at the upper right of the figure a part of the 80.2 keV line is visible. These events are induced by neutrons scattering inelastically off ^{131}Xe nuclei.

To be able to select the events of the 36.9 keV line, a two-dimensional Gaussian

$$\begin{aligned} f(x,y) = A \times \exp\Bigg\{ -\Bigg[&\left(\frac{\cos^2\theta}{2\sigma_x^2} + \frac{\sin^2\theta}{2\sigma_y^2}\right)(x-x_0)^2 \\ &+ 2\left(\frac{\sin 2\theta}{4\sigma_x^2} + \frac{\sin 2\theta}{4\sigma_y^2}\right)(x-x_0)(y-y_0) \\ &+ \left(\frac{\sin^2\theta}{2\sigma_x^2} + \frac{\cos^2\theta}{2\sigma_y^2}\right)(y-y_0)^2\Bigg]\Bigg\} \end{aligned} \tag{3.66}$$

was fit to the distribution, where x_0 and y_0 are the x (S1) and y (S2) coordinates of the center of the Gaussian distribution respectively. σ_x and σ_y are the width parameter in x (S1) and y (S2) direction and θ is the angle with which the blob is rotated clockwise. The results of the fit are:

$$A = 30.74 \pm 0.61\,,$$
$$x_0 = 116.89 \pm 0.23\,,$$

$$
\begin{aligned}
y_0 &= 9070 \pm 17\,, \\
\sigma_x &= 16.57 \pm 0.19\,, \\
\sigma_y &= 1352 \pm 15\,, \\
\theta &= (-5.29 \pm 0.18) \times 10^{-3}\,.
\end{aligned}
$$

The elliptical cut along the z-σ line is then defined as

$$
\frac{((x-x_0)\cdot\cos\theta-(y-y_0)\cdot\sin\theta)^2}{z^2\cdot\sigma_x^2}+\frac{((x-x_0)\cdot\sin\theta+(y-y_0)\cdot\cos\theta)^2}{z^2\cdot\sigma_y^2}<1\,. \quad (3.67)
$$

3.2.2 Event Selection Cuts

All event selection cuts that are used in the analysis of the 225 live days in 2011 are presented in [76]. To simplify, the spin independent and spin dependent elastic analysis will here be referred to as *standard analysis*. In this section, the application of all these cuts for the inelastic analysis will be discussed. For each cut this section presents the effect on the high energy events as required in inelastic scattering and conclude whether this cut is necessary or not and whether it has to be modified. Afterwards their acceptances are calculated.

Data quality cuts

Data quality cuts are designed to remove events that are originated from noise but are recognized as physical events.

S1 coincidence. PMTs spontaneously emit dark current signals that could be interpreted as an S1 signal. An S1 coincidence cut requires that at least 2 PMTs observe the S1 light signal simultaneously. However, it was observed that this cut does not have any impact on S1 signals larger than 60 PEs, since the S1 light emission is strong enough to ensure that multiple PMTs are triggered and record the event. Therefore this cut is not used in the inelastic analysis.

S1 width. The sampling rate for the PMT data is 100 MHz. Therefore the distribution of the width at 10% of the height of small S1 pulses shows a regular structure. Pulses with a very small width belong to noisy events and are rejected by an S1 width cut. Also this cut was found to have no effect on the data of interest in this analysis.

Ratio between signal and noise. To reject waveforms that contain many pick up pulses, a cut tests the waveform for the ratio of the area of the S1 and the $S2_b$ peaks over the rest of the waveform (Total Area without the S1 and the $S2_b$ peaks). $S2_b$ is the part of the S2 signal

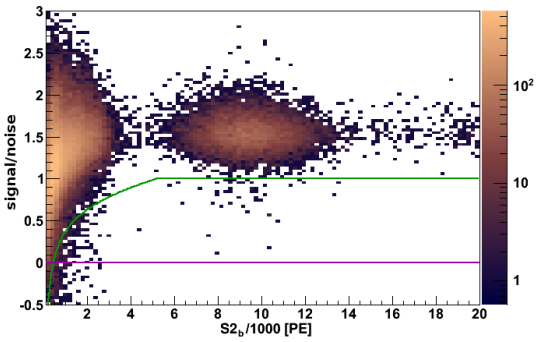

Figure 3.11: Events of elastic scattering ($S2_b$<4000 PE) and inelastic scattering (6000<$S2_b$/PE<14000) from an AmBe neutron calibration. The signal/noise cut removes events that lie below the green or the purple curve.

that is collected by the bottom PMT array. The ratio *signal/noise* is hence defined as

$$\text{signal/noise} = \log_{10}\left(\frac{\text{S1} + \text{S2}_\text{b}}{\text{Total Area} - \text{S1} - \text{S2}_\text{b}}\right) . \tag{3.68}$$

Figure 3.11 shows the signal/noise parameter over $S2_b$. At the very left (until $S2_b \approx 4000$ PE) there are the elastic events. The distribution above that around $S2_b \approx 9000$ contains the inelastic events from the 36.9 keV line. An average value of the signal/noise parameter is ∼1.6.

There are two versions of the signal/noise cut, both of which are used in the standard analysis: the first version (shown as purple line in figure 3.11) cuts events with signal/noise < 0, meaning that the area of the S1 and the $S2_b$ peak is required to be larger than the area of the rest of the waveform. There is no effect on AmBe calibration events of this cut. The second version of the cut (green line in figure 3.11) is defined to remove the 1% of the AmBe calibration data with the largest noise compared to the S1 and $S2_b$ signal, by fitting a third order polynomial to the 1% quantile to the distribution of the signalnoise parameter of the elastic scattering. In the inelastic event energy region it removes all events with signal/noise < 1. Applied to the AmBe calibration data, the cut removes 70 of 14 034 events. It was decided to keep this definition since it reliably removes events that show a much higher noise than the average. The acceptance of the signal/noise cut based on the AmBe calibration data set is $(99.5 \pm 1.7)\%$.

S2 asymmetry between top and bottom PMT array. The S1 peak may be too small to be recognized or too close to the S2 peak to be identified as a peak by itself. This happens for example for interactions that occur very close to the top PMT array. In this case, the distribution of photons collected on the top and bottom PMT array for the S2 signal is very

asymmetric. Events in the tail of the asymmetry of the S2 peak at the top and the bottom are cut away. For elastic events this cut has an acceptance of about 99.6%. For inelastic events this cut has no effect on the data set.

S2 ENERGY THRESHOLD. In the standard analysis there is an energy threshold cut for the S2 signal. This threshold is applied at 300 photoelectrons. Since S2 signals of the inelastic events imply about 10 000 photoelectrons there is no energy threshold cut required.

SELECTION OF SINGLE SCATTER EVENTS

Given the small probability of an interaction of a WIMP with the detector material, due to the small cross section particles scattering multiple times can be excluded to be WIMP interactions. Hence cuts are applied that remove events with several S1 peaks or several S2 peaks in the detector volume, as well as events with interactions that occurs simultaneously in the detector volume and in the veto.

S1 SINGLE CUT. Events with multiple S1 are filtered considering the number of PMTs by which the S1 pulse is observed. S1 peaks smaller than the largest S1 peak should not be observed by more than one PMT. In this case they can be ignored. The acceptance of the S1 single cut was calculated to be larger than $(99 \pm 1)\%$ for all energies above $S1 > 50$ photoelectrons.

S2 SINGLE CUT. The S2 single cut sets a threshold on the size of the second largest S2 peak and removes events containing an S2 peak that is too large. The standard analysis sets the threshold of the second largest S2 peak ($S2_2$) in a linear dependence that increases with the size of the largest S2 peak ($S2_1$).

$$S2_2 < \frac{S2_1}{100} + 67 \tag{3.69}$$

Figure 3.12 (left) shows the inelastic events of the AmBe neutron calibration data set. The green curve shows the energy dependent threshold of the standard analysis. Since the inelastic events are dominated by the electronic recoil of a monoenergetic gamma, they do not show this energy dependence. Hence an alternative threshold of 160 photoelectrons for the second largest S2 peak was defined.

To calculate the acceptance of this cut, it was applied to a data set that does not contain multi-scatter events. Figure 3.12 (right) shows the inelastic events, that have a time difference between the largest and the second largest S2 peak of more than 175 μs. This time difference is the maximum drift time in the XENON100 detector [33]. Hence these events are excluded to be

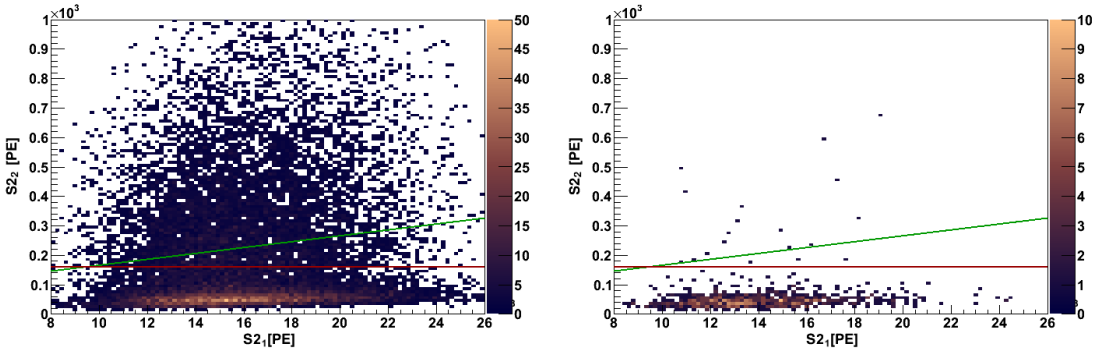

Figure 3.12: Definition of the S2 single cut. Left: inelastic events of the AmBe neutron calibration data, the threshold of the standard analysis S2 single cut (green curve) and the threshold of the redefined S2 single cut for the inelastic analysis (horizontal red line). Right: events in the inelastic energy region with a time difference between the largest and the second largest S2 peak larger than 175 μs. Since the maximum drift time in XENON100 is 175 μs, these events are excluded to be multi-scatter events.

double scatters. As a result 2.3% of the 818 events were removed. This leads to an acceptance of $(97.7 \pm 0.6)\%$.

VETO CUT. When there is an interaction in veto volume with an signal size ≥ 0.35 PE at the time of the largest S1 pulse the event is rejected. The acceptance is larger than $(99.6 \pm 0.4)\%$ for energies above $S1 > 50$ photoelectrons.

CONSISTENCY CUTS

Many of the properties of an event are correlated to each other. These properties can be checked among each other to reject events originated from extraordinary conditions that are not trustworthy and that show inconsistent properties.

S2 WIDTH CUT. The electron cloud diffuses during the drift towards the anode. Hence the S2 pulses get broader with a larger drift time. The S2 width (at 10% of the pulse height) is shown versus the drift time (dt) in figure 3.13. The data set was divided into 8 slices of dt. For each slice the median of the S2 width distribution as well as the quantiles for 95% and 99% were determined. A function

$$f(x) = p_0 + p_1 \times \sqrt{x} + p_2 \times x \tag{3.70}$$

was fit to these points. To remove events with an extraordinary large width the cut is defined along the 95% quantile:

$$\text{S2 width} < 126.86 + 2.6684 \times \sqrt{dt} + 0.44869 \times dt \tag{3.71}$$

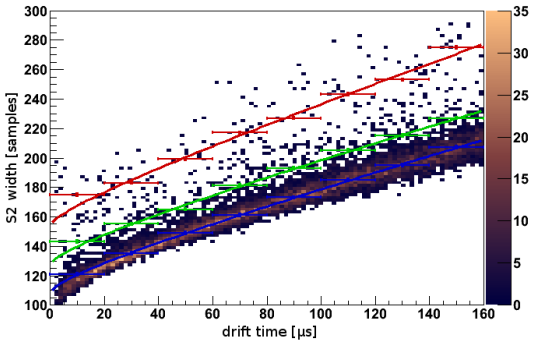

Figure 3.13: Definition of the S2 width cut. The width in samples (1 sample = 10 ns) of the S2 pulse at 10% of the pulse height from AmBe neutron calibration are shown in their dependence of the drift time (dt). The mean value of the width distribution for 8 slices in the dt (blue) together with the 95% quantiles (green) and the 99% quantiles (red).

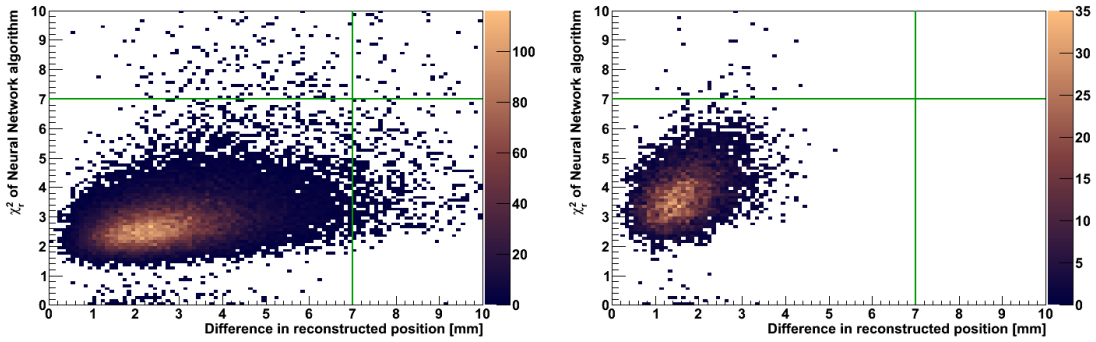

Figure 3.14: Definition of the χ^2_r and the position reconstruction cut. The cuts remove events with a χ^2_r higher than 7 and events for which the reconstructed position differs for more than 7 mm between the 3 reconstruction algorithms. Left: elastic events, right: inelastic events.

Its acceptance is (95.0±0.2)%.

Position reconstruction. The x-y-position reconstruction is performed by three different algorithms (see section 2.1.3). The best results were obtained by the neural network. Hence the coordinates obtained by this method are used for the analysis [76]. However, the reconstruction of the event can fail, for example if the hit pattern consists of two spots originated from a double-scatter event. To reject these events the difference of the position reconstructed by the three different methods may not be larger than 7 mm. Additionally, the χ^2_r value of the neutral network result may not be larger than 7. Figure 3.14 shows the distribution of the difference between the three position reconstructing algorithms (x-axis) and the distribution of the χ^2_r value (y-axis) of the neural network position reconstruction for the events of the standard

analysis (left) and for the 36.9 keV inelastic events (right) from AmBe neutron calibration data. The position reconstruction methods agree much better among each other for the inelastic events than for the elastic ones and the difference between the methods is far lower than the 7 mm threshold. Hence this cut is not applied in this analysis. 36 of the 14524 inelastic events exceed an χ^2_r value of 7, corresponding to an acceptance of 0.2%. That is comparable with the standard analysis where this cut has an acceptance of >99.8% for S1>50 photoelectrons.

GAMMA-X EVENTS. Multi-scatter events with one interaction below the cathode are referred to as *gamma-X events*. Since one of these interactions occur in an charge insensitive region, only the S1 pulse is registered. With only one valid S2 peak in the waveform these events are marked as single scatter events while the S1 pulses add up. This is dangerous because the S2/S1 fraction is lower and electronic recoil events (which have a higher S2/S1 than nuclear recoil events) are moved into the signal region of the standard analysis. To reject these events their hit pattern is compared to true single scatter events.

For the inelastic analysis, gamma-X events can not be moved inside the signal region. It is hence not crucial to remove these events and this cut is left out for the analysis.

TOTAL ACCEPTANCE. The acceptances of all cuts combined together result in a total acceptance of (91.1±3.5)%. The energy dependence of the cut acceptance is not considered, because the energy of the inelastic is dominated by the 39.6 keV photon. The width of the resolution originates purely from the detector resolution.

3.3 EXPLOITING THE ASYMMETRY

Inelastic events in the XENON100 detector have the largest energy contribution originating from electronic recoil induced by the 36.9 keV de-excitation γ and a smaller contribution from the nuclear recoil. As described in section 2.1.3, the ratio $\frac{S2_b}{S1}$ is larger for electronic recoils than for nuclear recoils. For the standard analysis this values can be used to discriminate between signal events (nuclear recoil) and background events (electronic recoils) [76]. However, since the main contribution is an electronic recoil, the event region is embedded in background events. Figure 3.15 shows the green ellipses around the inelastic events from the fit of the 2D Gaussian in figure 3.10 together with background calibration data from a ^{60}Co and a ^{232}Th source. The energy contribution from the nuclear recoil causes the inelastic events to be moved to lower $\frac{S2_b}{S1}$-ratios compared to electronic recoils.

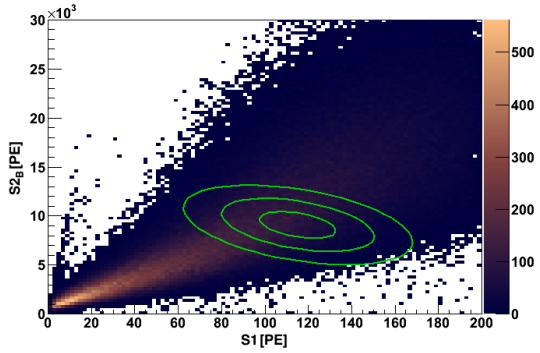

Figure 3.15: ^{60}Co and ^{232}Th calibration data in S1 over S2 together with the 1-σ, 2-σ and 3-σ ellipse indicating the location of the inelastic events

3.3.1 Defining the Flattened Discrimination Space

To exploit this asymmetry, it is advantageous to analyze the data in the *flattened discrimination* space, as it is shown in section 2.1.3. However, its definition in the standard analysis is optimized for the low energy region. This analysis takes the whole data set with S1 < 200 PE into account. Hence the flattened discrimination space has to be redefined.

Figure 3.16 (left) shows $\log_{10}(\mathrm{S2_b}/\mathrm{S1})$ over S1 of the data obtained with a ^{60}Co and a ^{232}Th calibration source. The whole data set was divided into 100 slices in S1. For each subset the mean value of the $\log_{10}(\mathrm{S2_b}/\mathrm{S1})$ over S1 was calculated. The mean value of each slice is shown in figure 3.16 as black data points depending on S1. The empirical function

$$\begin{aligned}\text{ER-mean}(x) = {} & A \cdot \exp(b \cdot x + c) \\ & + p_0 + p_1 \cdot x + p_2 \cdot x^2 + p_3 \cdot x^3 + p_4 \cdot x^4 + p_5 \cdot x^5 + p_6 \cdot x^6 \,, \end{aligned} \tag{3.72}$$

consisting of an exponential function and a 6th order polynomial, was fit to the electronic recoil mean values of $\log_{10}(\mathrm{S2_b}/\mathrm{S1})$ for different S1 values. The results of the fit are:

$$\begin{aligned} A &= 0.85 \pm 0.20 \\ b &= -0.228 \pm 0.044 \\ c &= -0.35 \pm 0.30 \\ p_0 &= 2.238 \pm 0.038 \\ p_1 &= (-1.56 \pm 0.28) \times 10^{-2} \\ p_2 &= (3.31 \pm 0.78) \times 10^{-4} \end{aligned}$$

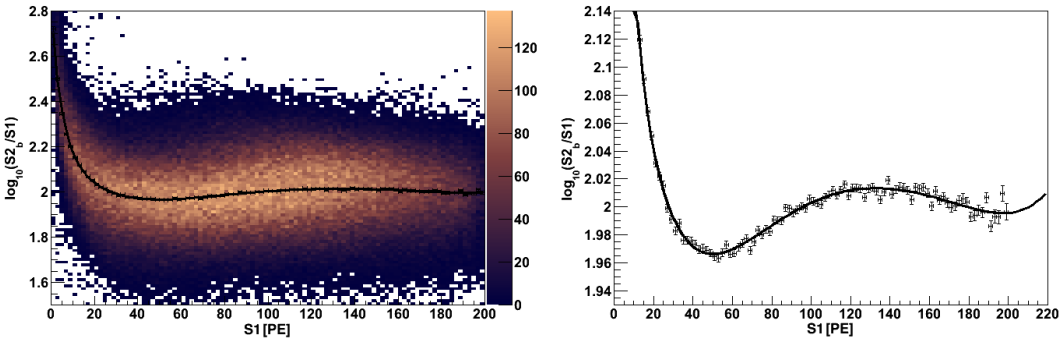

Figure 3.16: Left: Electronic recoil data from ^{60}Co and ^{232}Th calibration shown in $\log_{10}(S2_b/S1)$ over S1. The black data points show the mean of the $\log_{10}(S2_b/S1)$ parameter for slices in S1. Right: Data points for the mean of $\log_{10}(S2_b/S1)$ for each slice of S1 together with the fit function eq. (3.72).

$$p_3 = (-3.35 \pm 1.09) \times 10^{-6}$$
$$p_4 = (1.84 \pm 0.81) \times 10^{-8}$$
$$p_5 = (-5.38 \pm 3.01) \times 10^{-11}$$
$$p_6 = (6.64 \pm 4.48) \times 10^{-14}$$

Figure 3.16 (right) shows the fit function together with the data points in a range of S1 between 0 and 200.

The flattened parameter is designed such that the electronic recoil band mean gets the parameter value of 0. Hence to define the parameter space, the fit function for the electronic recoil band mean is subtracted from the $\log_{10}(S2_b/S1)$ parameter

$$\text{flattened space} = \log_{10}\left(\frac{S2_b}{S1}\right) - \text{ER-mean}(S1)\,. \tag{3.73}$$

The result of the flattening is shown in figure 3.17 with ^{60}Co and ^{232}Th calibration data. The electronic recoil events are distributed around flattened space $= 0$ for all S1.

Figure 3.17 (right) shows the same AmBe neutron calibration events as in figure 3.10 transformed to the flattened parameter space. The horizontal blue line at $\log_{10}\left(\frac{S2_b}{S1}\right) - \text{ER-mean} = 0$ indicates the electronic recoil band mean by definition. The lines above and below are the 1-σ, 2-σ and 3-σ quantiles from the Gaussian fit to the $\log_{10}\left(\frac{S2_b}{S1}\right)$ distribution of the 100 S1 slices. The green curves are the 1-σ, 2-σ and 3-σ quantiles of the inelastic event distribution like in the ellipses in figure 3.10. The 1-σ events (39%) are located almost completely below the electronic

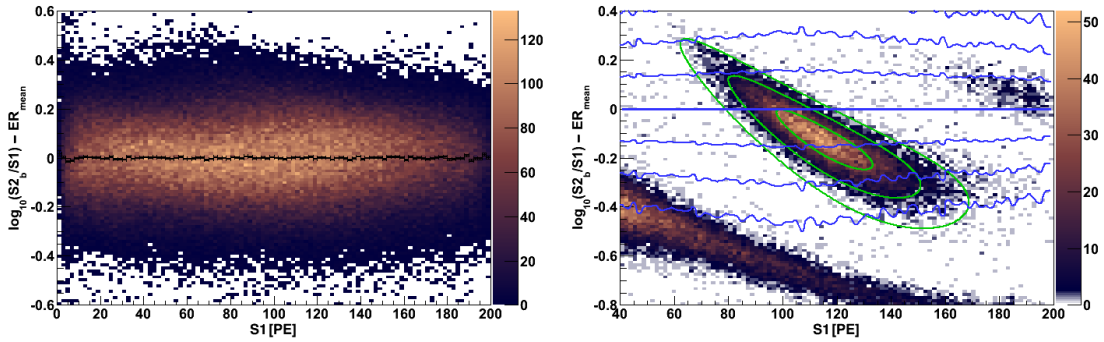

Figure 3.17: Left: Electronic recoil data from ^{60}Co and ^{232}Th calibration data in the flattened parameter space $\log_{10}(\mathrm{S2_b}/\mathrm{S1}) - \mathrm{ER\text{-}mean}$, which is designed such that the electronic recoil events are distributed around 0 for all S1. Right: Inelastic events from an AmBe neutron calibration transformed into flattened parameter space. Together with the 1-σ, 2-σ and 3-σ ellipse of the inelastic events and the mean of the electronic recoil band as well as the 1-σ, 2-σ and 3-σ lines.

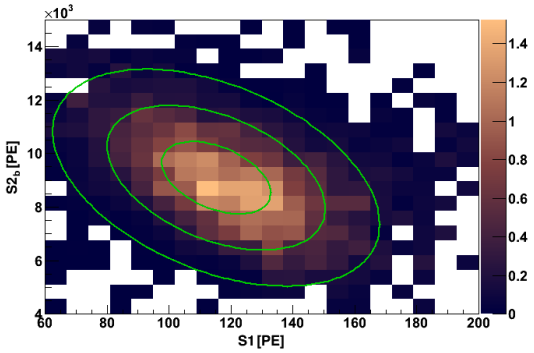

Figure 3.18: Signal to noise ratio in $\mathrm{S2_b}$ over S1. The Signal distribution is obtained by an AmBe neutron calibration and the background distribution by ^{60}Co and ^{232}Th calibration. The green ellipses indicate the 1-σ, 2-σ and 3-σ quantiles of the signal distribution.

recoil mean and only a minor fraction of the events inside the 2-σ quantile (86%) are above the electronic recoil mean.

A study of the ratio between signal and noise (figure 3.18) shows that this value drops to 50% outside of the 2-σ quantile. This suggests to take the 2-σ quantiles as boundaries of the region of interest.

3.3.2 Definition of the Asymmetry Parameter

In the flattened space the mean and the full 1-σ region of the distribution of the signal events is located below the electronic recoil mean. Hence, an asymmetry parameter can be defined by the number of events below the ER band mean and above. Figure 3.19 shows the regions

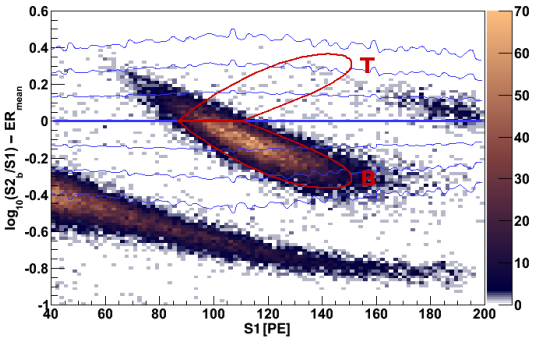

Figure 3.19: Definition of the region of interest for the asymmetry parameter. The signal region is the part of the area inside the 2-σ ellipse of the inelastic event distribution that lies below the electronic recoil mean. The control region is the signal region mirrored on the electronic recoil mean. The electronic recoil mean is shown as a horizontal blue line at 0. The other blue curves indicate the 1-σ, 2-σ and 3-σ quantiles of the event distribution.

that are taken into account for the definition of the asymmetry parameter. The part of the 2-σ ellipse that lies under the electronic recoil mean is taken as a signal region. These events will be referred to as *bottom events*. The control region is defined as the picture of the signal region mirrored on the electronic recoil mean (the flattened space $= 0$ line). They are located above the electronic recoil mean. Events in the control region will therefore be referred to as *top events*. The asymmetry parameter is defined as:

$$AS = \frac{B - T}{B + T}, \tag{3.74}$$

where B is number of bottom events and T the number of top events. An excess of signal events results in an increased number of bottom events B. Hence a signal event would increase the asymmetry parameter. The distribution of the asymmetry parameter for a specific number of signal events was determined by a Monte Carlo simulation, as explained in the next section.

3.3.3 Monte Carlo Simulation of the Asymmetry Parameter Distribution

To simulate the asymmetry parameter, background as well as signal events have to be generated. To generate the background events, the distribution of the events in the ^{60}Co and ^{232}Th calibration data (Figure 3.17, left) were scaled down such that the number of events in a selected side band in a region $30 < \mathrm{S1/PE} < 50$ is the same as in the data set of the science run with 225 life days. This region certainly does not contain signal events. There are 280

	Simulation	DM data set
in the side band	1 068 437	280
total	10 000 000	2621

Table 3.3: Number of events in total and inside the side band for as simulation and the DM data set. To get the total number of events in the Monte Carlo simulation the background distribution has to be scaled down such that it contains the same number of events in a side band.

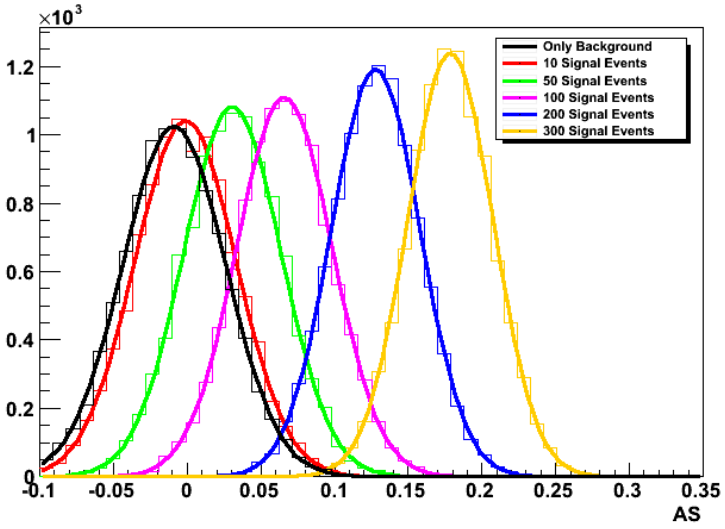

Figure 3.20: Distribution of the asymmetry parameter for different numbers of signal events. For background only (zero signal events) the mean of the distribution is located around AS=0. For in creasing number of events the distribution get shifted to higher AS values and becomes narrower.

events counted in this region. This number determines the number of events used in the MC simulation. A simulation with 10^7 events results in 1 068 437 events in the side band. Hence the total number of events in the simulation to obtain 280 in the side band is 2621 ± 157. To include the uncertainty of this number, the Monte Carlo Simulation is set up such that the total number of simulated events is picked from a Gaussian distribution around 2621 with a width of 157.

A background event for the simulation is chosen from the ^{60}Co and ^{232}Th electronic recoil calibration data in flattened space (figure 3.17, left). Each simulated event is tested whether it is located inside the bottom region or the top region. The number of events inside the top or bottom region B or T is calculated accordingly. The black curve in figure 3.20 is the distribution of the resulting parameter from only background. It is centered around an asymmetry parameter of 0.

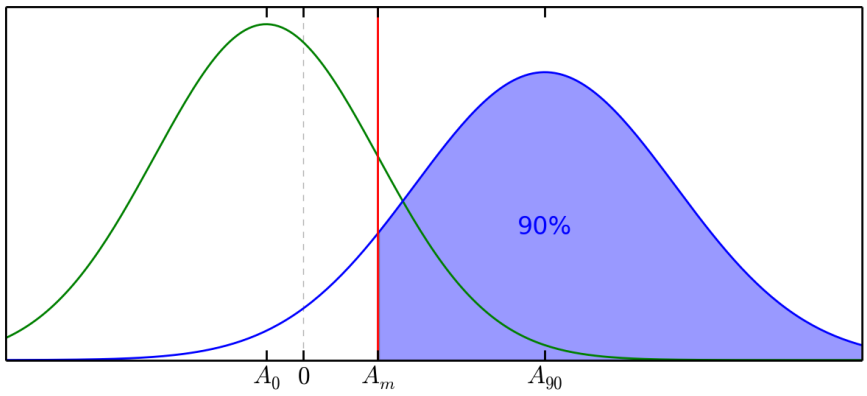

Figure 3.21: Distribution of the asymmetry parameter for different numbers of signal events. For background only (zero signal events) the mean of the distribution is located around AS=0. For in creasing number of events the distribution get shifted to higher AS values and becomes narrower.

The distribution of the asymmetry parameter including signal events was obtained in two steps. First, the same procedure for the background events was executed. After that, a certain number of signal events were chosen from the distribution of the 40 keV inelastic events of the AmBe calibration data (figure 3.17, right). For each event that was located in the bottom or the top region the numbers B and T were increased, respectively.

The distributions for various numbers of events are shown in figure 3.20. Each distribution is shown together with a Gaussian fit. With increasing number of events the distribution gets shifted towards higher values of the asymmetry parameter and at the same time narrower.

Obtaining a Limit on the Number of Signal Events

The limit on the WIMP-nucleon cross section for inelastic scattering can be directly calculated from the limit on the number of signal events in the detector by the expected event rate due to the recoil spectrum (see section 3.1). The Monte Carlo simulation presented above associates a certain number of events with a value of the asymmetry parameter. Hence a limit on the WIMP-nucleon cross section with 90% confidence level (C.L.), is correlated with the asymmetry parameter that can be excluded with a 90% C.L.

Figure 3.21 depicts the analysis principle for the limit on the asymmetry parameter. The Monte Carlo simulation for the case in which there would be only background events, yields to an Gaussian distributed asymmetry parameter around a value A_0. This value is expected to be close to 0 but can vary for different choices of the analysis region. The distribution is shown as a green curve. In case there are signal events, this asymmetry parameter increases. The null hypothesis H_0 is that the measured value for the asymmetry parameter A_m is compatible with

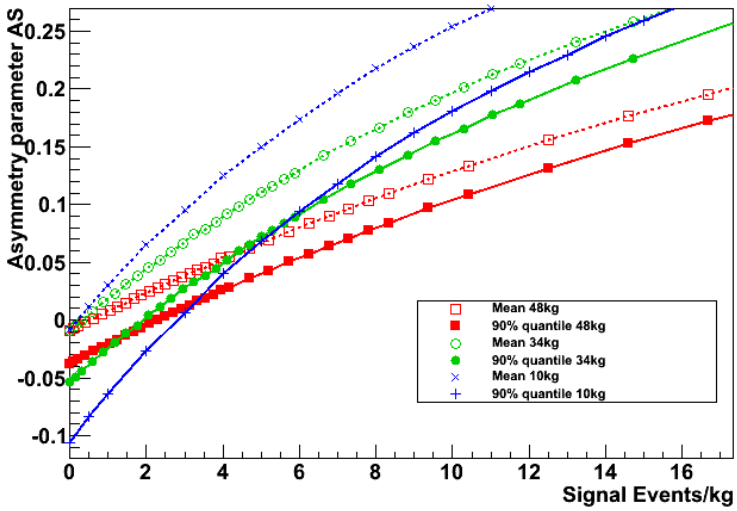

Figure 3.22: Asymmetry parameter corresponding to a certain number of signal events per kg for the fiducial masses 48 kg (red squares), 34 kg (green circles) and 10 kg (blue crosses). The mean value of the asymmetry parameter distribution is shown with open symbols (connected with a dashed lines). The 90% quantile giving the value for the 90% C.L. exclusion limit on the asymmetry parameter is shown with full symbols (connected with solid lines).

this distribution. If a value A_m (shown as vertical red line) is measured, the value A_{90} has to be found, for which 90% of the events would result in a higher asymmetry parameter than A_m. This is the value that lies 1.28 times the standard deviation of the distribution around A_{90} higher than A_m. The cross section corresponding to A_{90} (which is different for different WIMP masses) is the limit on the cross section.

Comparison of different fiducial volumes

For different fiducial volumes, the number of signal events, the number of background events and hence the distribution of the asymmetry parameter changes. Figure 3.22 shows how the asymmetry parameter is connected with the number of signal events per kg for the fiducial masses 10 kg, 34 kg and 48 kg. For a certain number of signal events, a Monte Carlo Simulation was performed to obtain the distribution of the asymmetry parameter. The mean of the distribution is shown by open symbols that are connected by dashed lines and the 90% quantile is shown by full symbols.

The number of signal events that can be excluded with 90% C.L. for a certain fiducial mass is the value at which the curve of the 90% quantiles crosses the horizontal line at the measured asymmetry parameter. For a lower measured asymmetry parameter (under-fluctuation

Fiducial mass (kg)	excluded nr. of events	excluded events per kg
10	27	2.7
34	65	1.9
48	110	2.3

Table 3.4: Number of signal events that can be excluded when an asymmetry parameter of 0 is measured for the fiducial masses 10 kg, 34 kg and 48 kg. Of these masses, 34 kg creates the lowest limit per kg fiducial mass on the number of signal events.

of the background), larger fiducial volumes lead to a lower limit of signal events, whereas for a higher measured asymmetry parameter (over-fluctuation of the background), smaller fiducial volumes are advantageous. Table 3.4 shows the excluded total number of signal events and the excluded number of events per kg fiducial mass for the three simulated fiducial volumes. With a fiducial mass of 34 kg the lowest exclusion limit is obtained for an asymmetry parameter of 0. Therefore in this analysis this is chosen as the fiducial mass.

Comparison of sigma contour lines for the signal region

After determining the fiducial volume, the final shape of the signal region has to be chosen. Figure 3.17 shows the 1-σ, 2-σ and the 3-σ ellipse of the two-dimensional fit to the inelastic events. Taking different sigma contour lines for the signal region changes the number of events in the signal region, the number of background events and hence the distribution of the asymmetry parameter changes. Figure 3.23 shows the connection between the asymmetry parameter and the number of signal events for the different contour lines of 1.0, 1.5, 2.0, 2.5, 3.0 sigma. For a certain number of signal events a Monte Carlo Simulation was performed to get the distribution of the asymmetry parameter. The mean of the distribution is shown by open symbols that are connected by dashed lines and the 90% quantile is shown by full symbols.

The number of signal events that can be excluded with 90% C.L. for a certain fiducial value is the value at which the curve of the 90% quantiles crosses the horizontal line at the measured asymmetry parameter. While the exclusion curve for the 1.0 and the 1.5 sigma contour is clearly worse than the others for a large range of signal events, the curve for 2.0, 2.5 and 3.0 sigma show similar values near the expected value for the asymmetry parameter. In general the lower the sigma the higher the slope of the curve. Hence, for a lower measured asymmetry parameter (under-fluctuation of the background), the 3.0 sigma contour leads to a lowest limit of signal events, whereas for a higher measured asymmetry parameter (over-fluctuation of the background), smaller signal regions are advantageous.

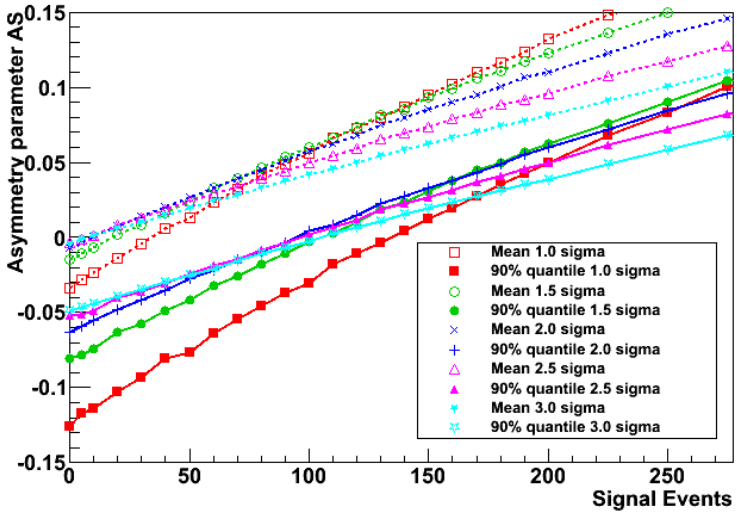

Figure 3.23: Asymmetry parameter corresponding to a certain number of signal events for the contour lines of 1.0 (red squares), 1.5 (green circles), 2.0 (blue crosses), 2.5 (purple triangles) and 3.0 (cyan stars) sigma. The mean value of the asymmetry parameter distribution is shown with open symbols (connected with a dashed lines). The 90% quantile giving the value for the 90% C.L. exclusion limit on the asymmetry parameter is shown with full symbols (connected with solid lines).

Contour line	Sensitivity Integral I_S
1.0 σ	102.5
1.5 σ	82.9
2.0 σ	77.2
2.5 σ	87.4
3.0 σ	98.9

Table 3.5: Sensitivity integral for the different sigma contours lines for the definition of the signal region.

A measure for the sensitivity of a sigma contour is the integral over all excluded signal events weighted with the probability to measure the corresponding asymmetry parameter $W_0(AS)$ in case that there are no signal events:

$$I_S = \int W_0(AS) \times \text{Signal}(AS)\, d(AS) \tag{3.75}$$

The probability to measure the asymmetry parameter AS with zero signal events is obtained from the MC simulation for zero signal events with the particular sigma contour line. Table 3.5 shows the sensitivity integral I_S for the simulated sigma contours. Taking the 2.0 sigma contour line leads to the best sensitivity and was therefore chosen for this analysis.

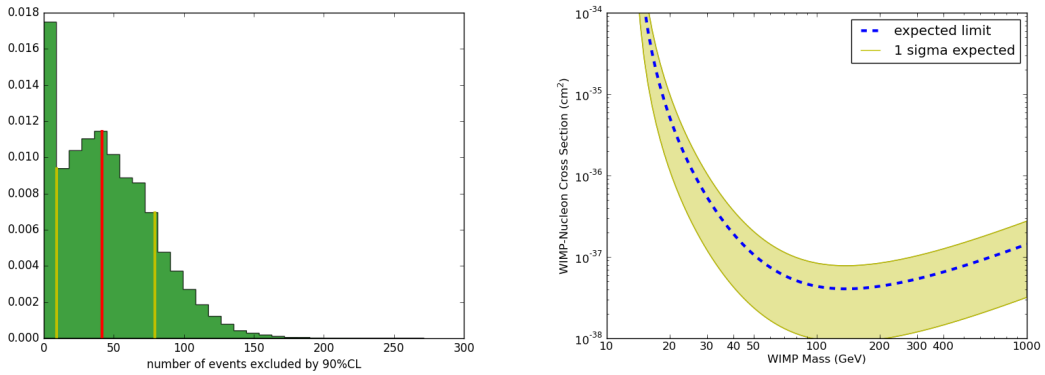

Figure 3.24: Sensitivity of the asymmetry parameter analysis. Left: Distribution of limits on the number of signal events from sampling number of events around the expected number of background events. The median is given by a red line. The borders for the 1 σ band by two yellow lines. Right: Limit calculated from the median of the excluded number of signal events together with the 1 σ band.

Sampling the Sensitivity

To determine the sensitivity 100 000 values of the asymmetry parameters were sampled from the distribution of the asymmetry parameter for background only obtained by Monte Carlo simulation (figure 3.20). For each sampled asymmetry parameter, the asymmetry parameter A_{90} was calculated that can be excluded with 90% C.L. With the results the Monte Carlo simulations for different number of signal events A_{90} can be converted into the number of signal events N_{90} that can be excluded with 90% C.L. The distribution of N_{90} is shown in figure 3.24 (left). The median of this distribution is $N_{90,\mathrm{med}} = 41.7$ events. The 1 σ band reaches from 9.2 events to 79.4 events. Figure 3.24 shows the expected limit on the cross section obtained from $N_{90,\mathrm{med}}$ together with the 1 σ band. The expected limit has a minimum at $4.05 \times 10^{-38}\,\mathrm{cm}^2$ at a WIMP mass of $140\,\mathrm{GeV/c}^2$. At this WIMP mass the 1 σ band reaches from $(7.8 - 0.9) \times 10^{-38}\,\mathrm{cm}^2$.

3.3.4 Result

After unblinding of the 225 live days run $T = 256$ events in the top and $B = 228$ events in the bottom region are found. That corresponds to an asymmetry parameter of

$$AS_{\mathrm{DM}} = \frac{B - T}{B + T} = -0.0579\,. \tag{3.76}$$

The Dark Matter events with the signal and the control region are shown in figure 3.25. This asymmetry parameter leads to a number of excluded events of 13.13. The limit on the cross

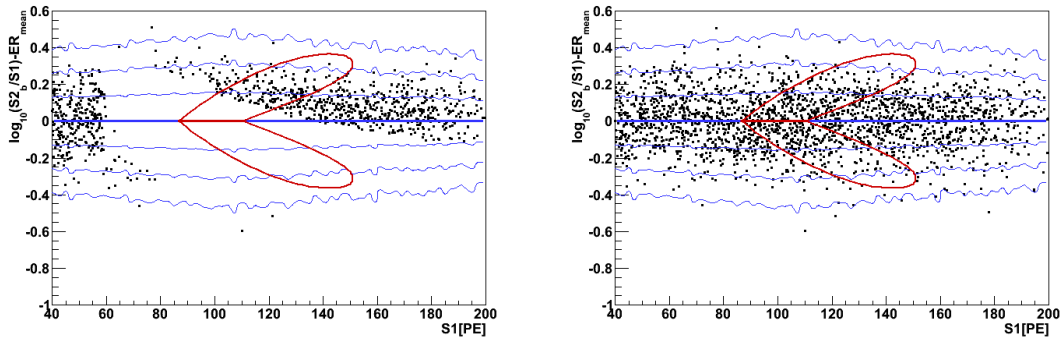

Figure 3.25: Dark matter events for the asymmetry parameter in the region of interest of the 225 life days run in the flattened parameter space after unblinding using all analysis cuts and a fiducial volume of 34 kg. Left: dark matter data set with blinded signal region. Right: Dark matter data set after unblinding.

section is shown in figure 3.26. The limit has a minimum cross section of $1.29 \times 10^{-38}\,\mathrm{cm}^2$ at a WIMP mass of $140\,\mathrm{GeV/c}^2$.

3.4 Count Based Analysis of the Inelastic Scattering Events

This analysis aims to improve the sensitivity by comparing the number of events inside the signal region with the number of expected events.

3.4.1 Simulation of the Inelastic Events

In section 3.1 the energy recoil spectrum of elastic and inelastic events was discussed. The difficulty, however, is to obtain the distribution in the S1-S2 plane. As explained in section 2.1.1 on page 10, the deposited energy is converted either into charge or light and therefore S1 and S2 are anti-correlated. Here a model for the S1-S2 distribution of the electronic recoil and the nuclear recoil part of the inelastic events is presented.

Correlation coefficient or electronic recoil events

The energy of the inelastic events is dominated by the electronic recoil of the de-excitation gamma. For small energy depositions the size of S1 and S2 can be regarded as uncorrelated [76]. Therefore, to simulate the S1 and S2 signal for an inelastic event, the electronic recoil event is simulated with a given anti-correlation of S1 and S2, whereas the nuclear recoil event is assumed to have uncorrelated S1 and S2. The S1 and the S2 of each part is summed up separately (see figure 3.27).

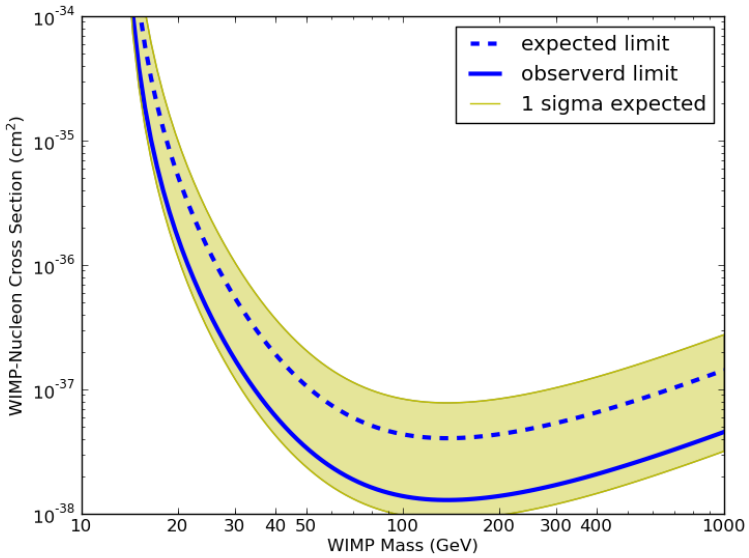

Figure 3.26: Limit from the asymmetry parameter. The expected sensitivity is shown by the dashed blue line and the yellow band (1σ) and the resulting exclusion limit by a solid blue line.

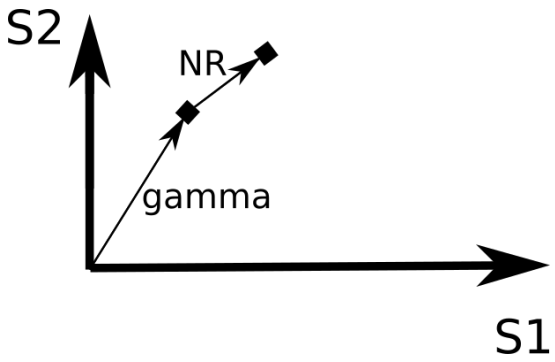

Figure 3.27: Principle of the simulation of the signal events. The S1 and the S2 for the gamma is simulated independently from the nuclear recoil. The S1 and the S2 of the nuclear recoil is added to the ones of the electronic recoil respectively.

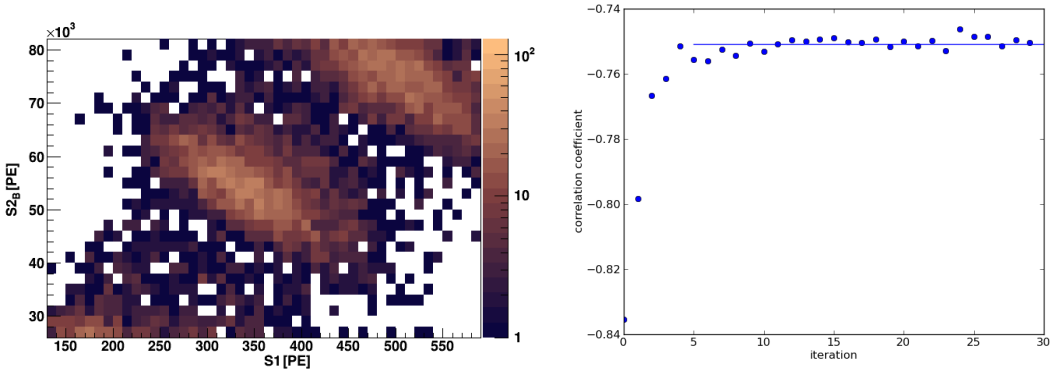

Figure 3.28: Determination of the correlation coefficient for electronic recoils. Left: events of the 164 keV gamma line of the metastable state ^{131m}Xe state. Right: iteration of the correlation coefficient (iteration algorithm described in the text). For the mean value (blue line) the values with iteration number larger than 5 were taken into account.

By neutron scattering the isotope ^{131}Xe can get activated to the metastable state ^{131m}Xe with an energy level of 164 keV and a half-life of 11.8 days [79]. During the AmBe calibration data taking, these ^{131m}Xe states are accumulated. The emitted gamma line can be used to obtain the correlation coefficient for an electronic recoil event in XENON100.

Figure 3.28 (left) shows background data taken in the 20 days after the AmBe neutron calibration. It can be seen that there are other lines neighboring the 164 keV gamma line of the ^{131m}Xe state. Therefore the events have to be selected by a cut. However, a linear cut between the 164 keV line and the neighboring lines would bias the correlation coefficient. The only cut that does not bias the correlation coefficient is an elliptical cut given by the fit of a two-dimensional Gaussian to the 164 keV line. At first, the events were selected by hand. But since the fit depends on the selection of the events, the following steps were repeated iteratively to approach the correlation coefficient to the true value.

1. A two-dimensional Gaussian is fit to the selected data.

2. The data that lie within the 2 sigma contour of the two-dimensional Gaussian are selected.

3. The correlation coefficient is calculated with the newly selected data.

The value of the correlation for each iteration step is shown in figure 3.28 (right). It converges already after 5 iteration steps. As final value, the mean value after iteration step was taken (horizontal blue line). The uncertainty is half of the difference between the maximum and the

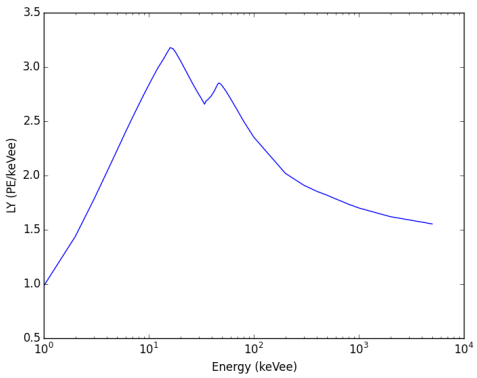

Figure 3.29: Light yield from the NEST model [77] over recoil energy for a drift field of 530 V/cm scaled to the detector response for the XENON100 experiment

minimum values. Hence the correlation coefficient is

$$\rho = -0.75 \pm 0.01\,. \tag{3.77}$$

Since the uncertainty is smaller than one percent, it is not necessary to take it into account as a nuisance parameter in the profile likelihood analysis.

Simulating electronic recoil

The mean value for the electronic recoil S1 is given by the energy and the light yield at this energy. The NEST model [77] predicts the light yield depending on the energy and the drift field. According to that model in the present drift field of 530 V/cm for a 40 keV gamma, 45.45 photons are produced. Figure 3.29 shows the detected photoelectrons per $\mathrm{keV_{ee}}$ for electronic recoil for different energies for the XENON100 experiment. Therefore the NEST curve for a drift field of 530 V/cm was scaled to the number of photoelectron measured in XENON100 at 122 $\mathrm{keV_{ee}}$ [76] $\left\langle \mathcal{L}_y \right\rangle = 2.20\,\mathrm{PE/keV_{ee}}$. Hence, for a 36.9 keV gamma in XENON100 2.7 photoelectron are produced. Therefore the mean of the S1 distribution is

$$\mu_{S1} = \mu_E \times 2.7 \frac{\mathrm{PE}}{\mathrm{keVee}} = 106.9\,\mathrm{PE}\,, \tag{3.78}$$

with the deposited energy of the gamma $\mu_E = 39.6\,\mathrm{keV}$. The width of the distribution was determined by the detector resolution of the 36.9 keV neutron line and of the 41.5 keV gamma line from a ^{83m}Kr calibration source. The result is

$$\sigma_{S1} = 15.8\% \times \mu_{S1} = 16.9\,\mathrm{PE}\,. \tag{3.79}$$

According to the NEST model [77],

$$N_{e^-} = (73.0 - N_\gamma)\frac{\text{electrons}}{\text{keV}} = (73.0 - 45.45)\frac{\text{electrons}}{\text{keV}} = 27.55\,\frac{\text{electrons}}{\text{keV}}. \tag{3.80}$$

In XENON100 the S2 signals have to be corrected for the electron lifetime but the electron extraction efficiency is 100% [33]. To obtain the number of photoelectrons, the number of electrons has to be multiplied by the secondary amplification factor $Y = 19.5\frac{\text{PE}}{e^-}$ [58] and the ratio of photoelectron measured in the bottom PMT array over the total (top and bottom) photoelectrons $r = 0.4195$ be considered. The secondary amplification factor Y includes the detection efficiency. The S2 light collection ratio r was measured in AmBe neutron calibration data. Hence the mean of the S2 peak is given by

$$\mu_{S2} = \mu_E \times 27.55\frac{e^-}{\text{keVee}} \times Y \times r = 8922\,\text{PE}\,. \tag{3.81}$$

The width of the distribution was determined by the detector resolution of the 36.9 keV neutron line and of the 41.5 keV gamma line of ^{83m}Kr. The result is

$$\sigma_{S2} = 14.7\% \times \mu_{S2} = 1312\,\text{PE}\,. \tag{3.82}$$

With the given values for μ_{S1}, σ_{S1}, μ_{S2} and σ_{S2} a two-dimensional Gaussian for S1 and S2 for the gamma can be created with any given correlation. By this means the angle of the ellipse is determined. The uncertainties on the resolutions $\sigma_{S1,S2}$ are around 1%. Hence they will not be taken into account as a nuisance parameter in the profile likelihood analysis.

Simulating nuclear recoil

Since the nuclear recoil energy is considerably smaller than the electronic recoil, S1 and S2 can be regarded as uncorrelated and be added to the S1 and S2 signals from the gamma.

For a recoil energy E the S1 signal is given by

$$S1 = E \cdot \mathcal{L}_{\text{eff}}(E) \cdot L_y(122\,\text{keV}_{\text{ee}}) \cdot \frac{S_{\text{nr}}}{S_{\text{ee}}}\,, \tag{3.83}$$

with $\mathcal{L}_{\text{eff}}(E)$ taken from [58], the light yield $L_y(122\,\text{keV}_{\text{ee}}) = 2.2\,\frac{\text{PE}}{\text{keV}_{\text{ee}}}$ and the field quenching factors $S_{\text{nr}} = 0.95$ and $S_{\text{ee}} = 0.58$ [76].

The S2 signal for a recoil energy E is given by

$$S2 = E \cdot Y \cdot r \cdot Q_y(E), \tag{3.84}$$

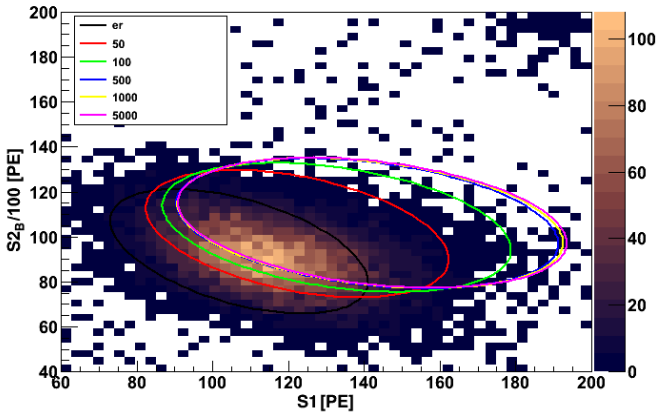

Figure 3.30: 2-σ contour lines of the S1-S2-distribution for electronic recoil (black) and for different WIMP masses between 50 GeV and 5 TeV together with the AmBe neutron calibration data.

where $Q_y(E)$ is taken from [58] and $Y = 19.5\,\frac{\mathrm{PE}}{e^-}$ and r is the same as above.

Figure 3.30 shows the result of the simulation. Over the AmBe neutron calibration data, it shows the ellipses of the 2-σ contour lines of the fit of a two dimensional Gaussian to the simulated S1-S2-distribution for different WIMP masses between 50 GeV and 5 TeV as well as for the electronic recoil only. It can be seen that the nuclear recoil ellipses are shifted mostly to higher S1 values with respect to the electronic recoil ellipse. The shift to higher S2 values is considerably smaller. The mean values of the S2 distribution differ only slightly for different WIMP masses, whereas there is a larger difference of the S1 mean values for different WIMP masses. However, for large WIMP masses ($m_\chi > 500\,\mathrm{GeV}$) the ellipses do not differ strongly anymore.

The mean values of the distribution of S1 and S2 for different masses are shown in figure 3.31. On average the gamma contributes 107 photoelectrons to S1 and 89.1 to S2 (indicated by a horizontal dotted line). For low WIMP masses the contribution from nuclear recoil vanishes. For larger WIMP masses the S1 signal converges to 140 photoelectrons; the S2 signal converges to 10 300 photoelectrons. The S1 signal is stronger influenced by a nuclear recoil than the S2 signal. The S2 signal carries a contribution originated from nuclear recoil of maximum 13%, whereas for S1 the nuclear recoil part is maximum 24%.

Comparison of simulation and AmBe data

To test the method of the simulation, the distribution of AmBe neutron inelastic events were simulated to compare it with the data. The spectrum of the neutron nuclear recoil was taken from Monte Carlo Simulations with the AmBe source. Figure 3.32 shows the 40 keV line of the

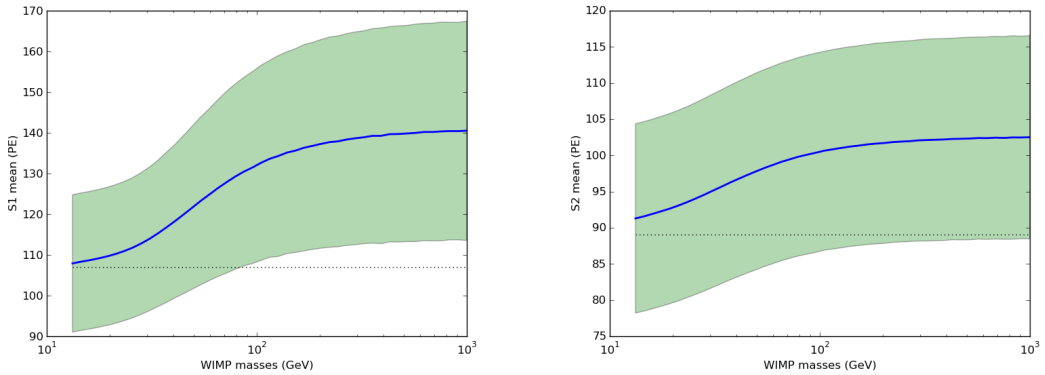

Figure 3.31: Mean values (solid blue line) of the S1 distribution (left) and of the S2 distribution (right) depending on the WIMP mass. The green band shows the root mean square of the distribution. The horizontal dotted black line shows the mean energy of the 36.9 keV gamma.

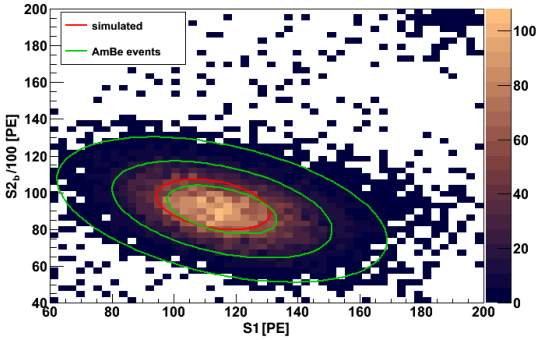

Figure 3.32: Simulation of the AmBe neutron calibration data compared with the measured data. The red ellipse shows the 1-σ contour of the simulation, next to the green 1-σ, 2-σ and 3-σ ellipse of the AmBe data.

	μ_{S1} (PE)	$\mu_{S2}/100$ (PE)
Simulation	112.7	93.6
Data	115.5	90.8
Shift	-2.8	3.2
Discrepancy	-2.5%	3.1%

Table 3.6: Comparison of the mean values of S1 and S2 between simulation and AmBe data

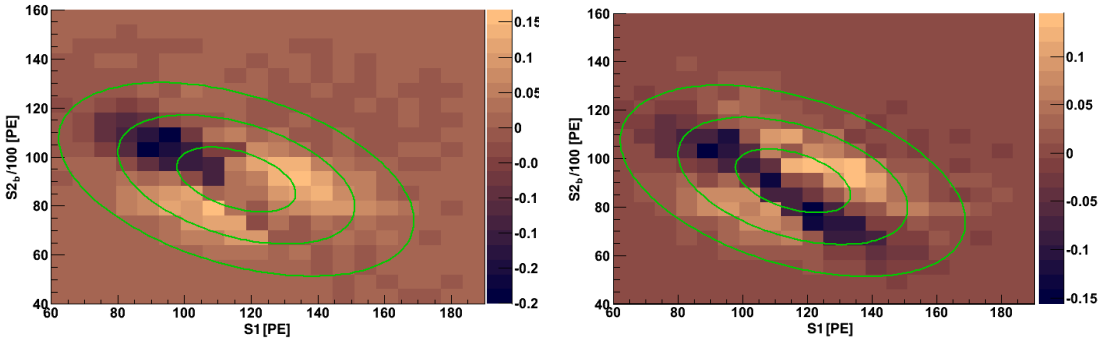

Figure 3.33: Residual of simulation and AmBe data (eq. 3.85) before (left) and after (right) the systematic shift.

AmBe neutron calibration data. The red ellipse indicates the 1-σ contour of the simulation. The green ellipses are the 1-σ, 2-σ and 3-σ ellipse of the AmBe data. Table 3.6 shows the mean values of the ellipses from the simulation and the AmBe data. The simulation is shifted with respect to the data for about 3%. To work against this discrepancy the shift in S1 and S2 direction is subtracted from all simulated events, meaning that every simulated event is shifted for 2.8 PE to S1 direction and for −3.2 PE in the direction of S2/100. This discrepancy is used as systematic uncertainty in the profile likelihood analysis. The effect of the shift is illustrated in the figures 3.33 and 3.34. The plots show the residuals or the ratio in the signal region between the normalized histograms of the AmBe data and the simulated events. Each histogram is scaled such the maximum bin has a content of 1. For each bin (i, j) the residual (figure 3.33)

$$\text{Res}_{ij} = \frac{\text{AmBe}_{ij}}{\max(\text{AmBe})} - \frac{\text{Simulation}_{ij}}{\max(\text{Simulation})} \tag{3.85}$$

or the ratio (figure 3.34)

$$\text{Ratio}_{ij} = \frac{\text{AmBe}_{ij}/\max(\text{AmBe})}{\text{Simulation}_{ij}/\max(\text{Simulation})} \tag{3.86}$$

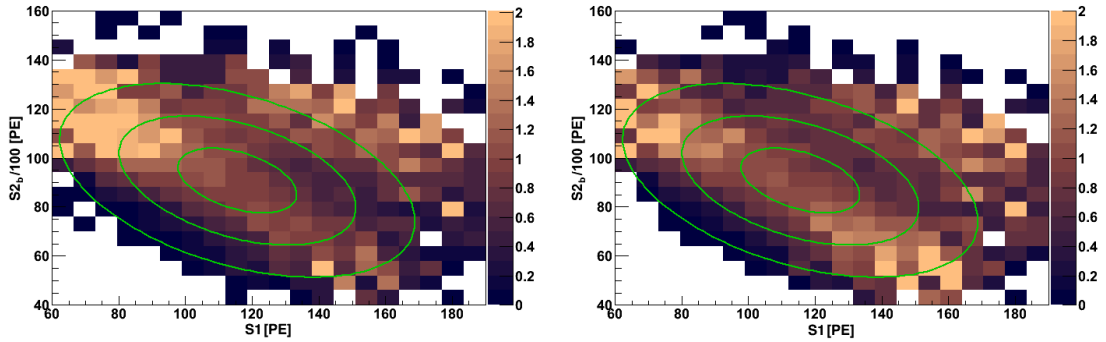

Figure 3.34: Ratio of simulation and AmBe data (eq. 3.85) before (left) and after (right) the systematic shift.

is shown. In both figures the green ellipses show the distribution of the AmBe data.

Estimation of the uncertainties

In the section above the uncertainties compensating a shift in S1 and S2 were described. The calculation of S1 for electronic recoil (eq. 3.78) does not imply further uncertainties. The energy of the de-excitation gamma is derived in nuclear physics and known with high precision. The NEST model itself does not include uncertainties.

The S2 light collection ratio between the top and the bottom PMT array

$$r = \frac{S2_{\text{bottom array}}}{S2_{\text{total}}} \tag{3.87}$$

and the secondary amplification factor Y are both factors for the formals for the S2 signal for both, electronic recoil (eq. 3.81) and nuclear recoil (eq. 3.84). Hence S2 scales with the same relative uncertainties as r and Y. The relative uncertainties of r and Y were determined to be 3.15% and 0.52%, respectively, leading to a combined relative uncertainty of 3.66% for S2. This way the uncertainties of S2 for the electronic recoil are covered as well. As for S1 the energy of the gamma is known with high precision and the NEST model itself does not include uncertainties.

For the nuclear recoil parts of S1 and S2 the situation is slightly more complicated, since $\mathcal{L}_{\text{eff}}$ and Q_y are functions of the recoil energy E. Hence the uncertainty depends as well on the recoil energy. The light yield $L_y(122\,\text{keV}_{ee})$ acts only on the nuclear recoil. However, since the electronic recoil depicts the dominant energy contribution, the uncertainty of $L_y(122\,\text{keV}_{ee})$, $\mathcal{L}_{\text{eff}}$ and Q_y is suppressed compared to the pure nuclear recoil events of elastic scattering. The conclusions of figure 3.30 imply that the uncertainties of Q_y have a weaker impact than the ones of $\mathcal{L}_{\text{eff}}$. The nuclear recoil effect larger changes on S1 than on S1.

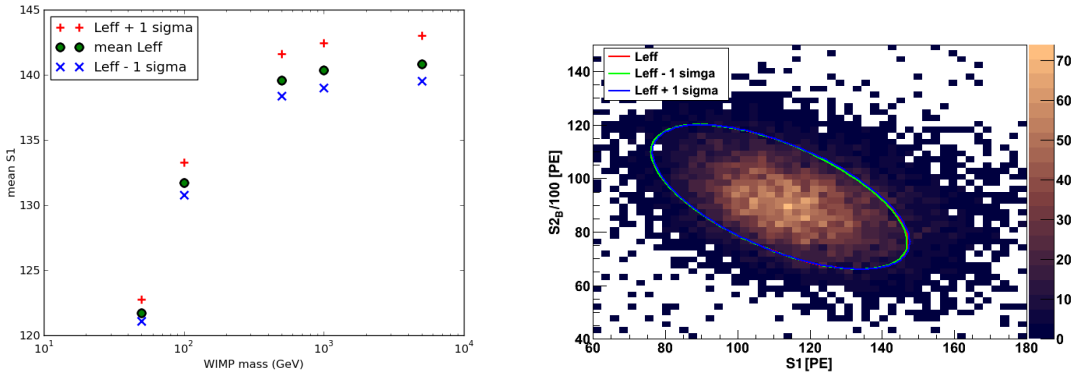

Figure 3.35: Changes of sigma ellipses when $\mathcal{L}_{\text{eff}}$ is changed. Left: Mean of S1 distribution for different WIMP masses for $\mathcal{L}_{\text{eff}}$ (green circles) and for $\pm 1\sigma$ (red pluses and blue crosses). Right: The change for the 2-σ contour line for the simulation of the AmBe neutron calibration data for $\mathcal{L}_{\text{eff}}$ (red) and for $\pm 1\sigma$ (blue and green).

The uncertainty of $L_y(122\,\text{keV}_{ee})$ is 4% [76]. However, since the contribution of the nuclear recoil to the total S1 is maximum 24% (see figure 3.31) we can neglect this uncertainty.

To see the effect of a change of $\mathcal{L}_{\text{eff}}$ within its uncertainty, figure 3.35 (left) shows the mean values of the S1 distribution for different WIMP masses for 3 different cases: when $\mathcal{L}_{\text{eff}}$ is remained unchanged, when $\mathcal{L}_{\text{eff}}$ is enhanced by 1 σ and when it is decreased by 1 σ. A change of $\mathcal{L}_{\text{eff}}$ by 1 σ results in changes of S1 of about 1%. Figure 3.35 (right) gives a qualitative idea on the effect on the simulation of AmBe neutron calibration.

For a more detailed idea of the impact of the uncertainty of $\mathcal{L}_{\text{eff}}$ figure 3.36 shows the deviation of the mean of S1 for a change of $\mathcal{L}_{\text{eff}}$ by 1 σ.

$$\text{deviation} = \frac{S1(\text{Using } \mathcal{L}_{\text{eff}} + 1\sigma) - S1(\text{Using normal } \mathcal{L}_{\text{eff}})}{S1}\,. \tag{3.88}$$

As expected the larger the WIMP mass, the larger the effect. The largest change is 1.6% for a 1 TeV WIMP. Since the deviation is always smaller than 2% the uncertainty of $\mathcal{L}_{\text{eff}}$ can be neglected. The deviations of the simulation in S2 were checked but as expected S2 does not change with $\mathcal{L}_{\text{eff}}$.

An analogous study to see the effect of a change of Q_y within its uncertainty, figure 3.37 (left) shows the mean values of the S2 distribution for different WIMP masses for the 3 cases for an unchanged Q_y, for a Q_y enhanced by 1 σ and for a Q_y decreased by 1 σ. A change of Q_y by 1 σ results in changes of S2 lower than 0.5%. Figure 3.37 (right) gives a qualitative idea on the effect on the simulation of AmBe neutron calibration. The deviations of the simulation in

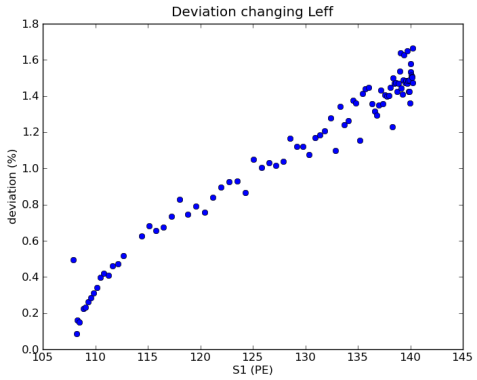

Figure 3.36: Deviation of the S1 value when $\mathcal{L}_{\text{eff}}$ is changed to $\mathcal{L}_{\text{eff}} + 1\sigma$ for different WIMP masses.

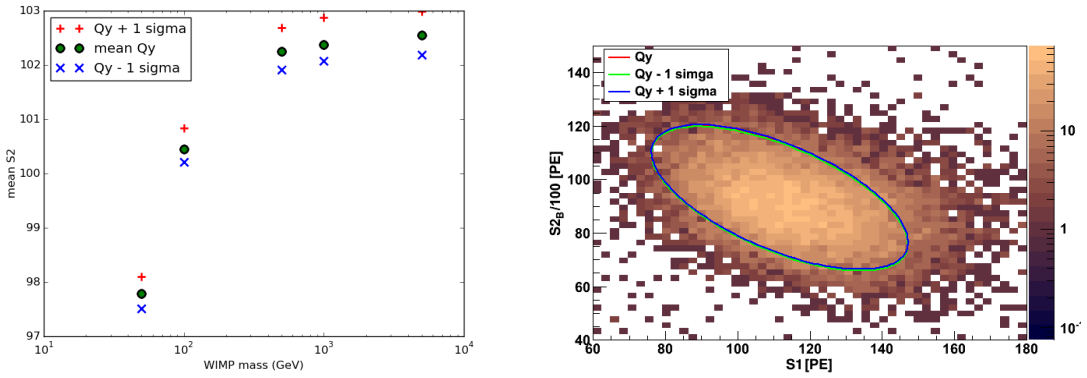

Figure 3.37: Changes of sigma ellipses when Q_y is changed. Left: Mean of S1 distribution for different WIMP masses for Q_y (green circles) and for $\pm 1\sigma$ (red pluses and blue crosses). Right: The change for the 2-σ contour line for the simulation of the AmBe neutron calibration data for Q_y (red) and for $\pm 1\sigma$ (blue and green).

S1 were checked but as expected S1 does not change with Q_y. Therefore, the uncertainties of Q_y can be neglected.

The uncertainties of the secondary amplification factor Y, the S1-S2-anti-correlation ρ, the light yield at 122 keV_{ee}, $\mathcal{L}_{\text{eff}}$ and Q_y are not taken into account into the analysis. In contrast, the S2 light collection ratio r and a systematic shift into S1 and S2 direction are taken as nuisance parameters into the profile likelihood analysis.

3.4.2 Determination of the Signal Region

Figure 3.38 (left) shows the background calibration data from a ^{60}Co and ^{232}Th calibration source. The green ellipses indicate the 2-σ contour lines of the event distribution from WIMPs

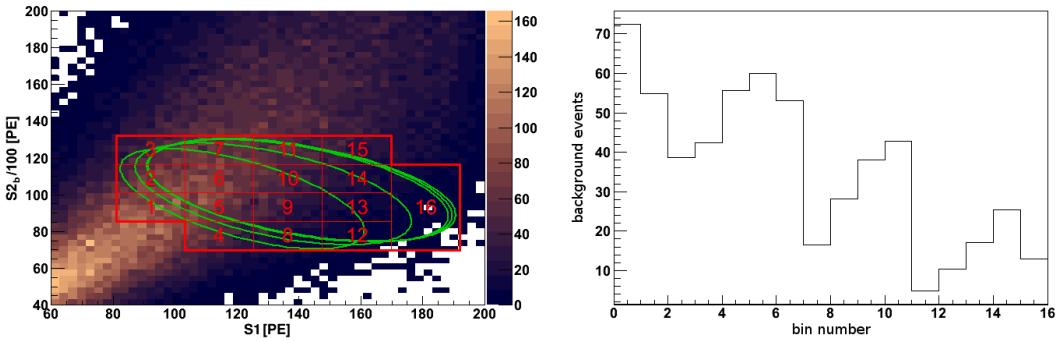

Figure 3.38: Left: background distribution (^{60}Co and ^{232}Th calibration source) with the 2-σ contour lines of the event distribution generated from WIMPs between 50 GeV and 5 TeV from figure 3.30 (green ellipses). The red frame is the border of the signal region, that is divided into 16 bins. Right: Expected background in each bin of the signal region. The distribution of the ^{60}Co and ^{232}Th calibration data was scaled to the dark matter data using the number of events outside the signal region (eq. 3.89).

between 50 GeV and 5 TeV shown in figure 3.30. To generate the signal region a rectangle around all possible sigma 2-ellipses was drawn, including the region 81 < S1/PE < 192 and 70 < $S2_b$/PE < 132. Then it was divided into 4 × 5 sub boxes. The sub box at the bottom left and the one at the top right is included into the signal region as we don't expect signal events there. The 3 boxes on the very right were merged (to bin number 16), because they contain very few events for both signal and background. This leaves a signal region with 16 bins, as it is shown in figure 3.38 (left) together with ^{60}Co and ^{232}Th calibration data.

Figure 3.38 (right) shows the expected number of background events in each of the bins 1 – 16, employing ^{60}Co and ^{232}Th data, scaled to background, using the events outside and inside the signal region. For the events outside the signal region the data was restricted to S1 < 191 (the maximum S1 of the signal region) to avoid influence of the high energy veto – a hardware cut for high energy events that is applied to reduce the amount of stored data. The data set of the ^{60}Co and ^{232}Th data contains 101 179 events outside the signal region and 27 030 events inside. In the dark matter data set, for which the signal region itself is blinded, 2140 events were counted outside the signal region. Hence the number of events inside the signal region for the dark matter data has to be scaled down by

$$S = \frac{N_{\text{outside,DM}}}{N_{\text{outside,cal}}} = 0.0212\,. \tag{3.89}$$

With this scaling factor, the expected number of background events is

$$N_{\text{bkg,exp}} = S \times N_{\text{inside,cal}} = 0.0212 \times 27030 = 571.7\,. \tag{3.90}$$

	Background calibration data set	DM data set
outside the signal region	101 179	2140
inside the signal region	27 030	571

Table 3.7: Number of events inside and outside the signal region to calculate the background expectation.

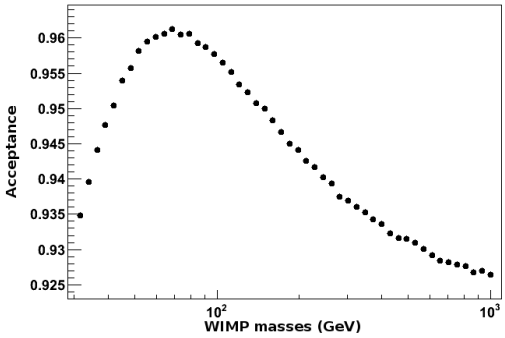

Figure 3.39: Acceptance of the signal region for different WIMP masses.

Figure 3.39 shows the acceptance of the total signal region for different WIMP masses. It was obtained by counting the number of events laying outside and inside of the signal region. With values between 92% and 96% the acceptance is higher than the one of the signal region for elastic scattering [42].

Comparison of background and data

To estimate the background distribution the ^{60}Co and ^{232}Th calibration data was scaled to the dark matter data set. To test this method the distribution of the events in the calibration data an in the dark matter data have to be compared outside the signal region. Figure 3.40 shows both distributions projected on the S1 axis (left) and on the S2 axis (right). The events inside the signal region (influencing the region 81 < S1/PE < 192 or 70 < S2/PE < 132) were not counted in both cases. The two distributions show a very good agreement.

3.4.3 Simplified Maximum Likelihood Analysis with one Bin

This section will present a simplified analysis where all bins are combined in one bin. The two most important nuisance parameters are implemented into the Likelihood function, i.e. the number of background events in the signal region B and the cut acceptance a_c. The Likelihood

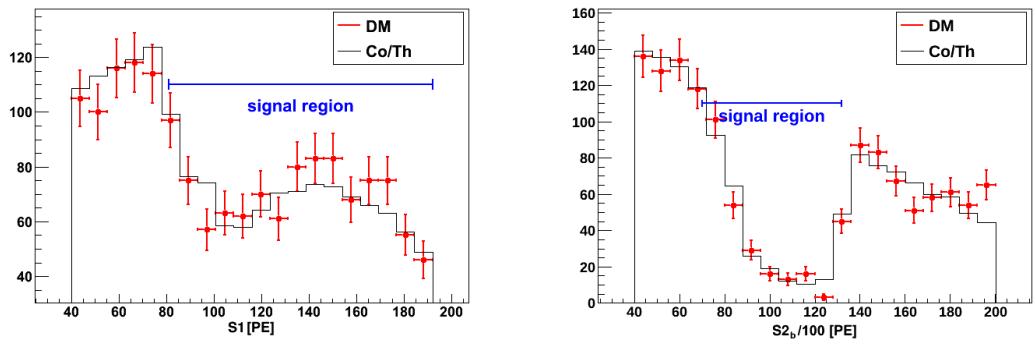

Figure 3.40: Test of the background model: comparison of the background data (black line) and expected background distribution (red points) of S1 (left) and S2 (right). The signal region (indicated by a blue bar) is blinded for both data sets.

function is defined as

$$\mathcal{L} = P(N; a_c \cdot S + B, \sqrt{a_c \cdot S + B}) \times P(B; \mu_B, \sigma_B) \times P(a_c; \mu_{a_c}, \sigma_{a_c}) \,, \tag{3.91}$$

where S is the parameter for the number of signal events and N is the number of measured events. For all P functions a Gauss distribution was taken.

The Likelihood function was calculated for each S, B and a_c. Then the nuisance parameters B and a_c were marginalized by summing over them, first over a_c then over B. Figures 3.41 shows the Likelihood function $\mathcal{L}(S, B)$ as a function of S and B, where a_c is already marginalized (left) and the Likelihood of the number of signal events with the marginalized background events (right)

$$\mathcal{L}(S) = \sum_B \mathcal{L}(S, B) \tag{3.92}$$

for two example values of measured events in the signal region N = 500 (top) and N = 600 (bottom). $\mathcal{L}(S)$ is a Gaussian distribution, truncated at 0, since negative number of signal events are not physical. The number of signal events that can be excluded by 90% confidence level N_{lim} is the number for which 90% of the area under $\mathcal{L}(S)$ is located left of N_{lim}

$$\int_0^{N_{\text{lim}}} \mathcal{L}(S) dS = 0.9 \times \int_0^{\infty} \mathcal{L}(S) dS. \tag{3.93}$$

In the example of figure 3.41 the 90% C.L. exclusion limit is at 25.9 signal events for N = 500 and 76.5 signal events for N = 600.

N = 500:

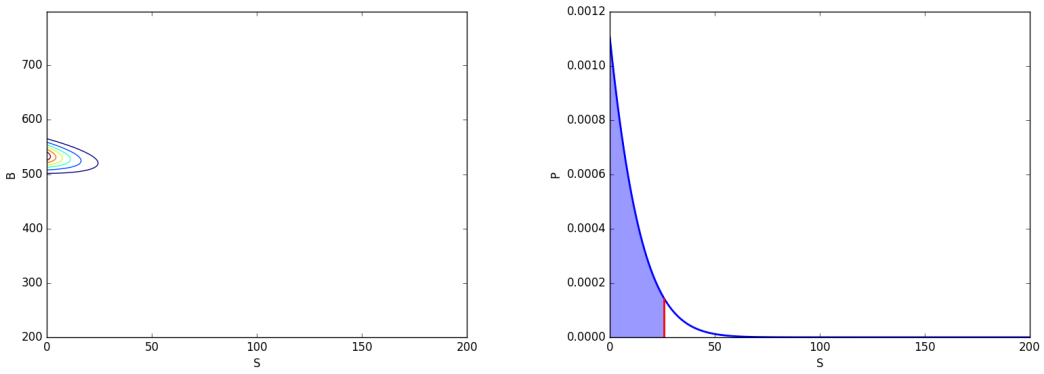

N = 600:

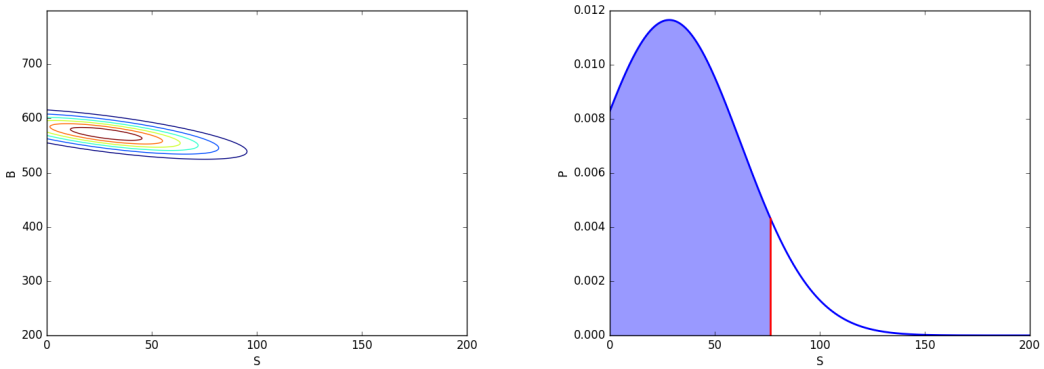

Figure 3.41: Two example Likelihood functions for the number of measured events N = 500 and N = 600. The left figures show the likelihood of the number of signal events S and the number of background events B (the cut acceptance a_c is already marginalized). The right figures show the Likelihood of the number of signal events S where the number of background events is marginalized. The number of signal events that can be excluded by 90% C.L. is marked by a vertical red line: The likelihood that the number of signal events is lower than that value is 90% (blue shaded area).

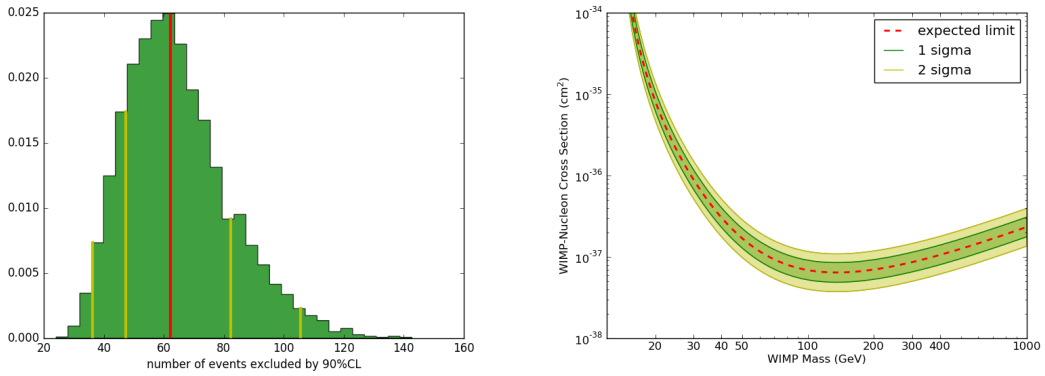

Figure 3.42: Sensitivity of the count based analysis with one bin. Left: Distribution of limits on the number of signal events from sampling number of events around the expected number of background events. The median is given by a red line, the boundaries for the 1 σ and the 1 σ band by yellow lines. Right: Limit calculated from the median of the excluded number of signal events together with the 1-σ band (green) and the 2-σ band (yellow).

Sampling a Sensitivity

To determine the sensitivity of this measurement, the limit was calculated for a distribution of number of events around the expected number of background events μ_B. Therefore the number of events N was sampled 10 000 times from a Gaussian distribution around $\mu_B = 571.7$ with a standard deviation of $\sqrt{\mu_B} = 23.9$. The distribution of limits on the number of signal events is shown in figure 3.42 (left). The median of the distribution is at 62.3 signal events. The boundaries for the 1 σ band are 47.2 and 82.4, and for the 2 σ band 36.2 and 105.5.

Figure 3.42 (right) shows the sensitivity on the cross section of this measurement. Therefore the limit of the median of the distribution of excluded signal events was calculated. The minimum of the expected limit is $6.4 \times 10^{-38}\,\mathrm{cm}^2$ at a WIMP mass of $134\,\mathrm{GeV/c}^2$.

3.4.4 Result

After unblinding, $N = 531$ events were found inside the signal region. Figure 3.43 shows the distribution in the dark matter events with the signal region. The measured number of events is 1.7 σ below the expected value. Figure 3.44 shows the likelihood function for the number of background events B and the number of signal events S given the number of events measured after unblinding. With the integration of the Likelihood function $\mathcal{L}(S)$, the limit on the number of signal events can be set to $N_{\mathrm{lim}} = 35.3$ events. This leads to a limit on the cross section that is below the sensitivity median shown in figure 3.42. The limit on the cross section derived

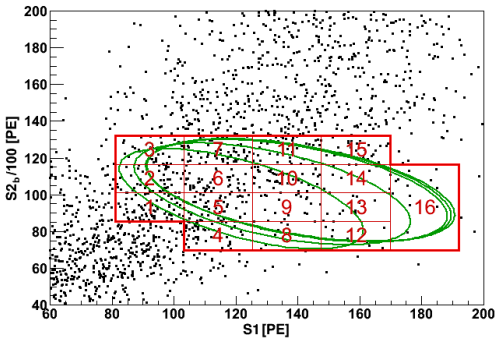

Figure 3.43: Dark matter events for the counting experiment in the signal region.

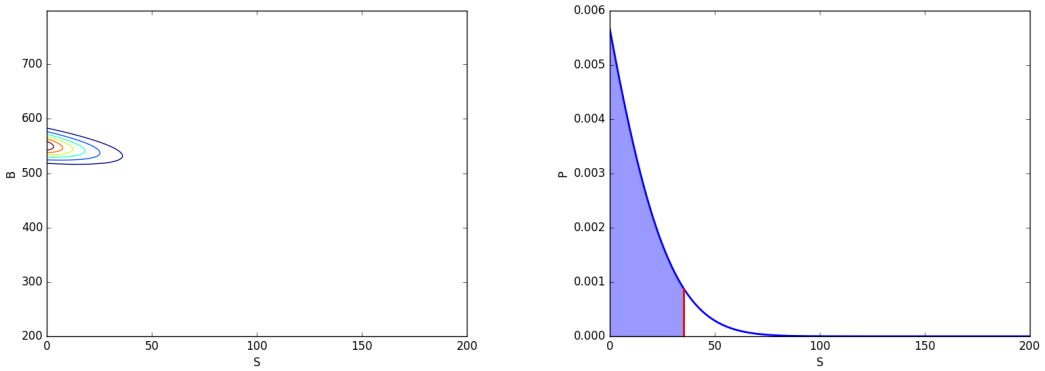

Figure 3.44: Likelihood functions for the number of measured events $N = 351$. Likelihood of the number of signal events S and the number of background events B (left) and the Likelihood of the number of signal events S where the number of background events is marginalized (right). The number of signal events that can be excluded by 90% C.L. is $N_{\text{lim}} = 35.3$ events (vertical red line).

from that number of events is shown in figure 3.45. It has a minimum of $6.4 \times 10^{-38}\,\text{cm}^2$ at a WIMP mass of $134\,\text{GeV/c}^2$.

3.5 Summary

Figure 3.46 summarizes the calculated limits that are discussed in this chapter together with the limit published by the XMASS experiment [80] for comparison. The asymmetry parameter analysis copes with a much smaller signal region than the counting method. Therefore the statistic is smaller and a background under fluctuation pushes the observed limit much further below the expected limit. Hence the asymmetry parameter analysis sets the most stringent limit on the inelastic cross section. However, the limit from the counting experiment has smaller uncertainties and is therefore more reliable than the fluctuation sensitive limit from

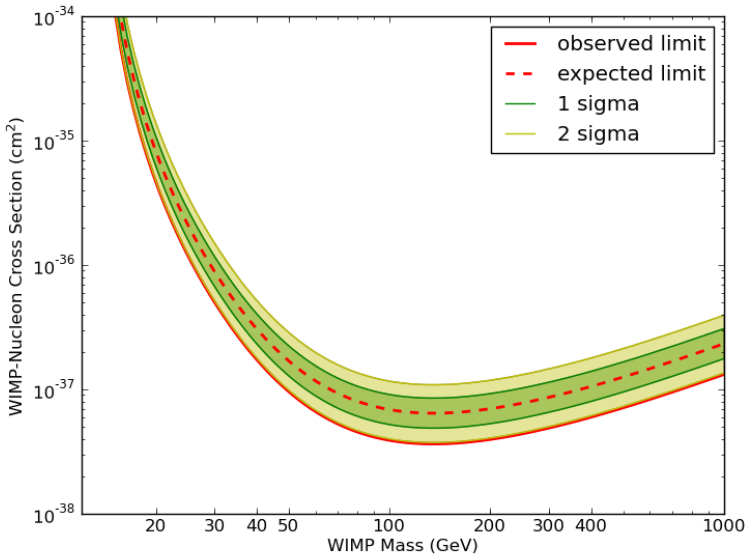

Figure 3.45: Limit from the counting experiment. The expected limit is shown as dashed line. The 1 σ and the 2 σ band are shown in green and yellow. The observed limit is shown as solid red line.

the asymmetry parameter. The more careful selection of the signal region in the counting experiment makes the limit more trustworthy as well. The 1 σ and 2 σ band is therefore shown for the counting experiment method.

The full Profile Likelihood analysis was performed by Alessandro Manfredini. It uses the division of the signal region into 16 bins, as shown in figure 3.38 and takes into account the nuisance parameters discussed above. This limit will be published in [81]. The minimum of this limit is $3.1 \times 10^{-38}\,\mathrm{cm}^2$ at a WIMP mass of $134\,\mathrm{GeV/c}^2$.

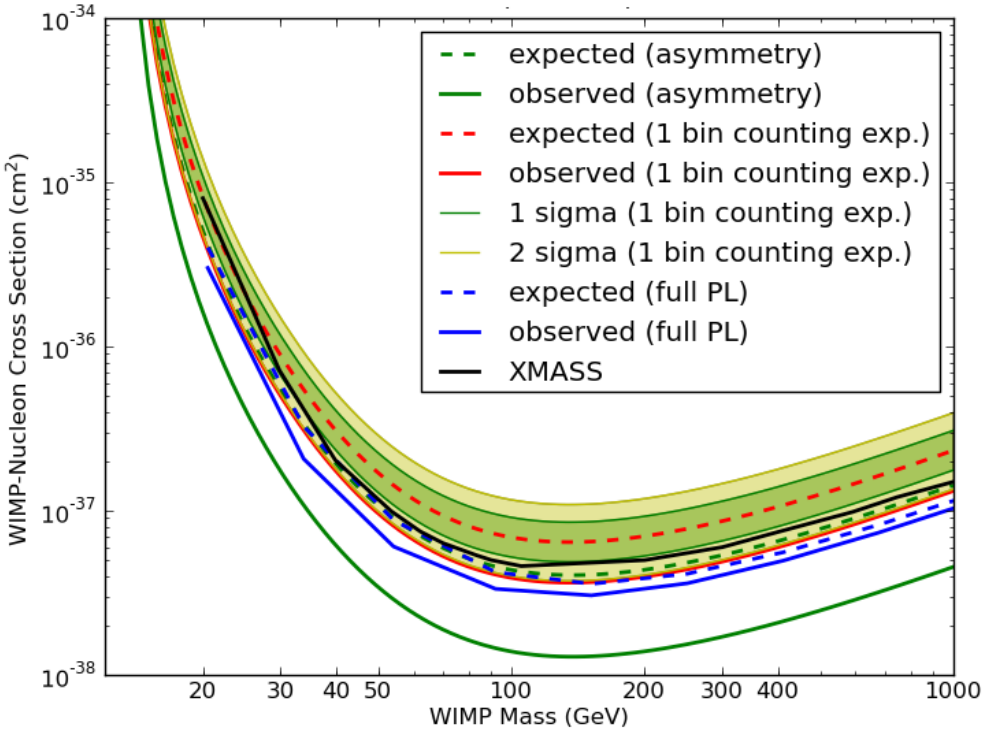

Figure 3.46: All Limits of the inelastic scattering. For the asymmetry parameter analysis (section 3.3) the expected (dashed line) and observed (solid line) is shown in green. The limit of the simplified 1 bin counting experiment (section 3.4) is shown in red together with 1 σ and the 2 σ band (green and yellow bands). The full Profile Likelihood result is shown in blue [81]. The black line shows the result of the XMASS experiment [80].

4

Cables and Connectors for the XENON1T Experiment

4.1 Introduction

In the two-phase xenon time projection chamber (TPC) of the XENON1T detector, 248 Hamamatsu R11401 [68, 69] photomultiplier tubes (PMTs) are installed: 127 in the top and 121 in the bottom array. For each PMT, four channels are required: two channels for the high voltage (high voltage and ground return) to place the dynodes on different electric potentials and two channels to pick up the signal from the last dynode. It is beneficial to use a coaxial cable for the transmission of the signal. In addition to the 248 R11401 PMTs, 6 R8520 PMTs are installed in the surrounding volume of the TPC vessel, to observe interactions in the liquid xenon outside of the TPC. Other than in XENON100, this is not used as an active veto. Temperature sensors and level meters are located in the TPC vessel as well for which additional 14 and 21 coaxial cables will be used, respectively.

All cables that are used for the TPC are guided through a pipe in the water tank to the infrastructure building and connect the PMTs with the amplifiers or the power supply over a total distance of 16.2 meters. Because of the signal run time the length of all signal cables has to be the same. The length difference between the signal cables is in the order of 1 cm.

To facilitate the assembly process, the cable tree is divided in three sections that are connected to each other by custom-made connectors. An overview of the cabling is given in

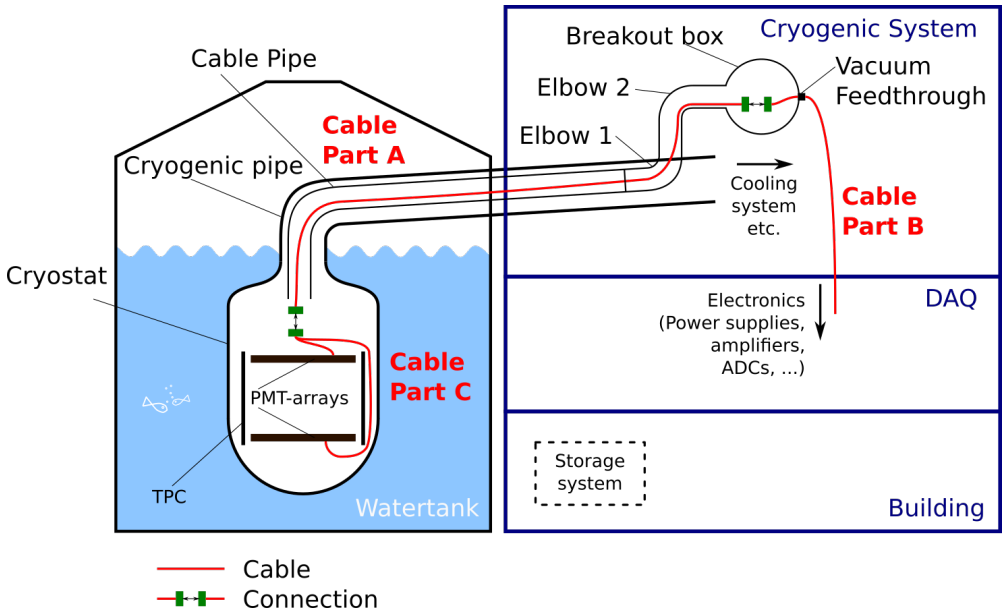

Figure 4.1: Overview of the cabling in XENON1T (not drawn to scale). The *cryogenic pipe* guides the cable pipe from the TPC that is situated in the center of the water tank, to the upper floor of the *building* where the cable pipe ends up in the *breakout box* that is equipped with vacuum feedthroughs. From there the cables are guided to the amplifiers and the DAQ in the middle floor.

figure 4.1. Going from the detector to the electronics, the first part of the cable tree reaches from the PMT bases in the detector to the top of the cryostat that contains the TPC. The second part goes through the pipe to the *breakout box* inside the building. The breakout box is a holder for the vacuum feedthrough flanges. The last part guides the cables from the breakout box through the vacuum feedthroughs and to the electronics: the signal first goes into an amplifier and then into the ADC. The HV cables are connected to the PMT power supplies.

For all the components in the experiment and its surroundings there are very stringent requirements with respect to their radioactivity. Hence the material selection of the cables and connectors plays an important role in their development, besides the performance and reliability. For the cable insulations the radio pure materials perfluoroalkoxy alkanes (PFA), polytetrafluoroethylene (PTFE or Teflon) and Kapton (polyimide) were chosen and the holding structure of the connectors were entirely made of PTFE.

Section 4.2 describes the development and the design of the cables and connectors for high voltage (sec. 4.2.1) and signal (sec. 4.2.1) in detail. In section 4.3 we discuss the results of the material screening for gamma emitters. In section 4.4 we describe the assembly process, and conclude in section 4.5.

4.2 Design of cables and connectors

This section will detail the development and selection of the cables and connectors for the high voltage and the signal lines of the PMTs.

4.2.1 High voltage

High voltage cables

The R114010 PMTs in the XENON1T detector are operated at about 1.5 kV with negative high voltage. However, the gain of each PMT may slightly vary. To set the gain of all PMTs to the same value, the voltage of each PMT is tuned individually. The setup has to allow to switch off particular PMTs if a problem occurs with them. Therefore the high voltage cables have to supply the PMTs with individual voltages that may also be zero. The requirement for the high voltage (HV) cables is to reliably stand the voltage applied to one PMT against the ground.

We identified a company that produces silver plated copper single wires (AWG 30) with a Kapton insulation that were rated up to 2 kV [82]. Similar single wires insulated with different flouropolymers like PTFE, PFA, fluorinated ethylene propylene (FEP) or ethylene tetrafluoroethylene (ETFE) were considered but no company could be found that can offer these products for a competitive price.

High voltage connector

Within the development of the connector, tests were performed with custom-made copper pins in a PTFE connector structure. However, the disadvantage of pure copper is the fact that it is not elastic enough to deliver a constant spring from one pin to another for a stable contact. One concept was to perform the contact by exploiting the fact that the PTFE support shrinks stronger than copper while cooling down and thus presses the female pins together onto the male pins. This concept was considered as not trustworthy for long-term performance. As the final solution we took the standard D-subminiature for the pins. These pins consist of a copper alloy plated with gold. The beryllium inside the copper alloy hardens the copper such that the contact between female and male pins is performed by the spring force of the pins itself. Section 4.3 presents the measured radioactivities of the pins and the cables.

We developed a PTFE structure (figure 4.2) to hold the channels for 24 PMTs. The ground returns of the PMTs are collected before they reach the connectors. Therefore only one ground return channel is required. For redundancy we installed two ground return channels in each HV connector such that each connector holds in total 26 pins. The pins are held between two PTFE pieces that prevent the pins from slipping out of the connector in both directions. This

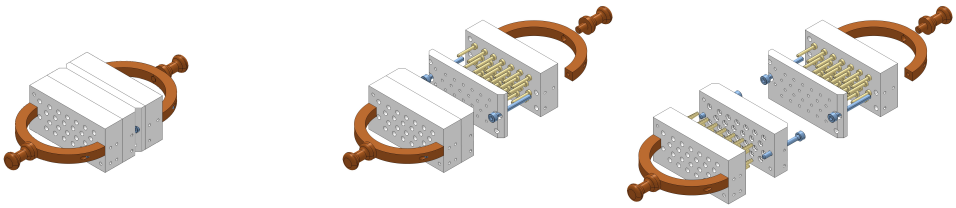

Figure 4.2: Technical drawing of the high voltage connector. It consists of PTFE, copper and stainless steel screws. The pins inside the connector are made of a copper alloy plated with gold.

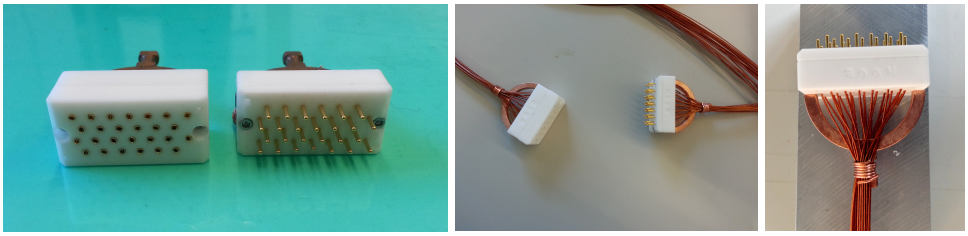

Figure 4.3: Picture of the high voltage connector. Left: unconnected female and male connector without cables. Center: cable ends with attached female and male connector. Right: male connector with connected cables.

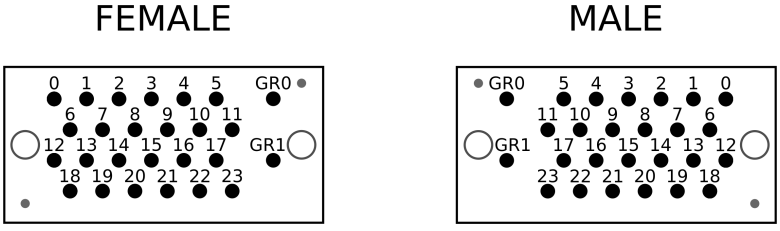

Figure 4.4: Pin distribution for the high voltage connector.

makes it necessary to put the cable through the holes of the piece that is behind the pins before installing the pins on the cables. The pins are crimped to the cables. Behind the PTFE holding structure a copper frame is installed on which the cables can be fastened with a copper wire (figure 4.3, right) to relief the strain on the cables. In the connector, the pins are aligned in four shifted rows with a distance of 4 mm between each pin. The ground return pins on one side of the connector have a larger distance to the other pins to introduce some asymmetry, preventing the connector to be connected the wrong way. To identify each bunch we punched numbers into the PTFE part of each connector (c.f. figure 4.3, right). Additionally, we produced small copper labels that were attached to the cable bunches with a small copper wire.

To test whether the connector pins loose their spring power, the connector was connected and disconnected repeatedly. Stability against high voltage was tested by supplying up to 2 kV to one pin, having the neighboring pins on ground in an air environment and in liquid nitrogen. Under realistic conditions, namely in gaseous xenon at a temperature of 166 K, a PMT was operated at 1.7 kV for about one minute. In none of these tests the connector showed any problems.

4.2.2 Signal

The MarmotXL testing facility

To test the cabling, a facility, MarmotXL, was used, in which the PMTs can be fully operated in 2 kg liquid and gaseous xenon environment (figure 4.5). The PMTs are installed inside a vacuum chamber. A cold finger located above the PMTs is connected to a pulse tube refrigerator (PTR). the PTR cools down the cold finger to a temperature below the operating temperature of 165 K, the boiling point of xenon. A heater allows to regulate the temperature very precisely. The xenon chamber is surrounded by an insulation vacuum. When the chamber is filled with gaseous xenon, the gas condenses on the cold finger and drops inside. The gaseous and the liquid xenon are cooling down the vacuum chamber. From the bases of the PMTs, both HV and signal cables are guided to vacuum feedthroughs at the top of the chamber.

Signal cables

The signal cable must transport the signal from the PMTs to the DAQ. Single wires, twisted pair cables and striplines were tested but discarded because of their significantly worse signal transmission properties compared to coaxial cables.

Two viable options were identified: Kapton insulated 30 AWG coaxial cables with 50 Ω impedance by Accuglass [82] and RG196 PTFE coaxial cables insulated with PFA by koax24 [83]. Both cables were screened for their radioactivity (see section 4.3). The screening results fa-

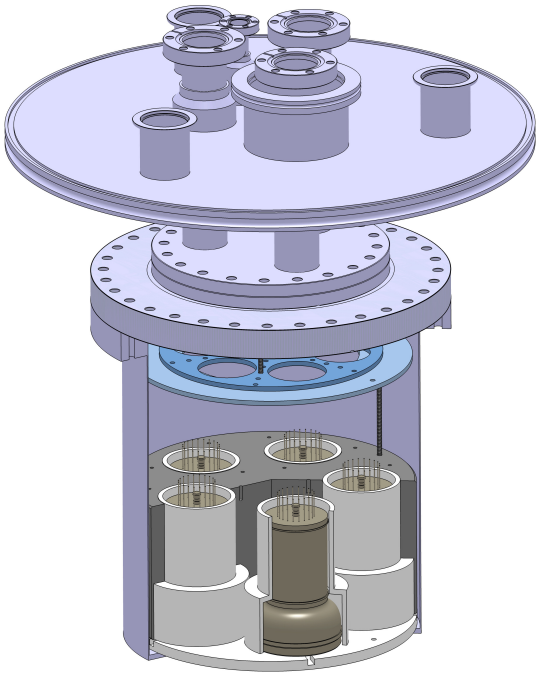

Figure 4.5: MarmotXL: A facility to test 5 simultaneously PMTs in liquid and gaseous xenon environment. The xenon chamber is surrounded by an insulation vacuum.

vor the RG196 cables. Furthermore, we experienced problems in the handling of the Kapton cables. It turned out to be much more difficult to strip their Kapton insulation and they are much stiffer. When the cables are fixed at the bases and then bent into cable guides the stiffness would result in an increased force on the bases and on the connection of the cables to the bases and hence in an unforeseeable risk to break. Finally Kapton cables would have been 12 times more expensive than the PTFE cable. For these reasons, the decision fell on the RG196 cables.

Signal connector

Noise pick up As a first approach, a connector similar to the HV connector was designed. This was a connector with parallel single pins for each signal and ground return channel. Since there is no coaxial connection, the signal channel is not shielded and hence prone to pick up noise.

Figure 4.6 (left) shows a recorded single photo-electron spectrum with the signal transmitted through the single pin connector, compared to the situation where a full coaxial connection is used. The spectra are normalized to the number of events. With the single connector there are less events in the single-photo electron peak than without. However the connector increases

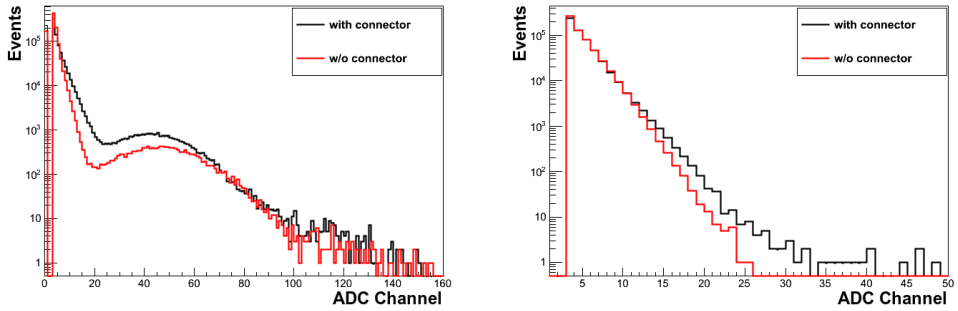

Figure 4.6: Noise pick up of non-coaxial connector: PMT spectra are shown with the connector (black) and with a coaxial connection (red). Left: Situation shown for a single photoelectron spectrum. Right: Shown for only noise.

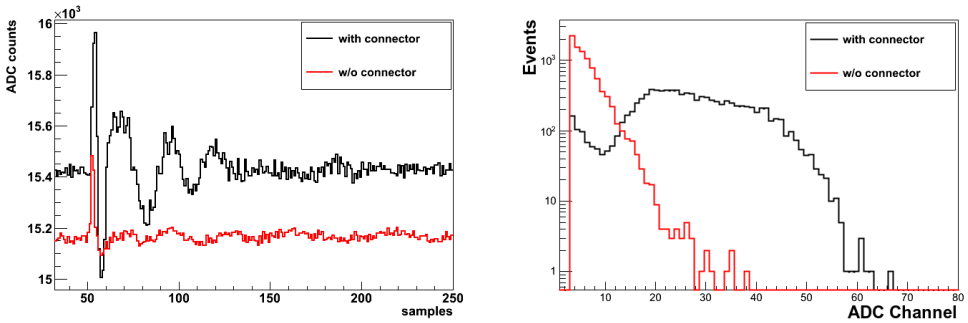

Figure 4.7: Crosstalk of a neighboring channel of a channel connected to a running PMT in the non-coaxial connector. Left: waveform with electric noise created by crosstalk in the connector (black) and waveform without the connector (red). Right: Spectrum with the recorded crosstalk events.

the number of events in the noise peak. In figure 4.6 (right) only the noise peak is recorded. The PMT high voltage is switched off in that measurement such that the PMT does not produce signals. There are more events with a larger noise. This means that the connector picks up noise and hence shifts noise events to higher energies.

Crosstalk Using parallel non shielded channels also gives rise to crosstalk between channels. To test this effect, a signal was transmitted by one channel and the neighboring channel was read out. Figure 4.7 (left) shows the additional noise in a waveform that is taken from a channel next to a PMT signal channel inside the single pin connector compared to the full coaxial connection. The spectrum of the registered peaks in this waveforms is shown in figure 4.7 (right). The connector creates an own population of events around 30 ADC channels.

For these reasons we decided to tolerate the extra material and to use an MMCX connector (figure 4.8, left) that establishes a fully coaxial connection. The MMCX pins are held by a

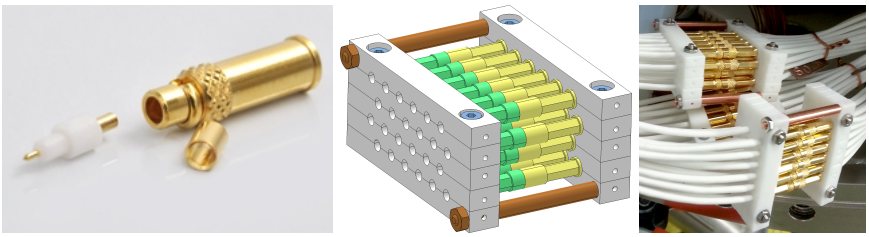

Figure 4.8: Left: An MMCX pin (male) for the signal connector. Center: technical drawing of the signal connector. Right: signal connector equipped with bunches of 24 coax cables and MMCX connectors.

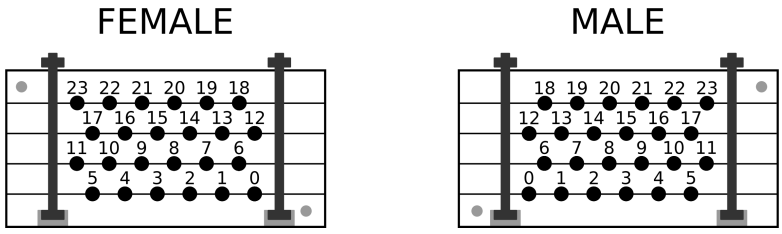

Figure 4.9: Pin distribution for the signal connector.

sandwich-like PTFE structure, each contains 24 cables in one bunch. This prevents the shield from getting in contact and creating ground loops. The whole holding structure is held together by two copper rods with a threat on both sides (figure 4.8, center). Like for the HV connector we punched numbers into the PTFE part of each connector and attached small copper labels to the cable bunches.

4.2.3 Vacuum Feedthroughs

For the vacuum interface we developed a *breakout box* – a cylindrical vessel that acts as a support structure for various CF flanges[1] (figure 4.10). The main body is a 350 mm diameter stainless steel cylinder which correspond to the CF350 standard. The length of the cylinder is 400 mm. This vessel is connected to the cable pipe through a CF100 elbow on the cryogenic system in the upper level of the building. The breakout box holds 3 CF40 feedthrough flanges for the HV cables and 6 CF63 feedthrough flanges for the PTFE coax cables.

The flanges are custom produced by *RHS*[84]. Either 104 HV cables or 72 signal cables are potted into the flanges using a confidential two part epoxy with high thermal conductivity, great electrical resistance and low outgassing [85] (figure. 4.11).

The stability of the feedthroughs against pressure has been tested in vacuum and using overpressure of 3.6 bar. The feedthroughs were mounted on a cylindrical chamber with an inner volume of 4.1 liters. The results of the test with overpressure is shown in figure 4.12.

[1]Standard for vacuum flanges by the company *Varian*, standing for CONFLAT

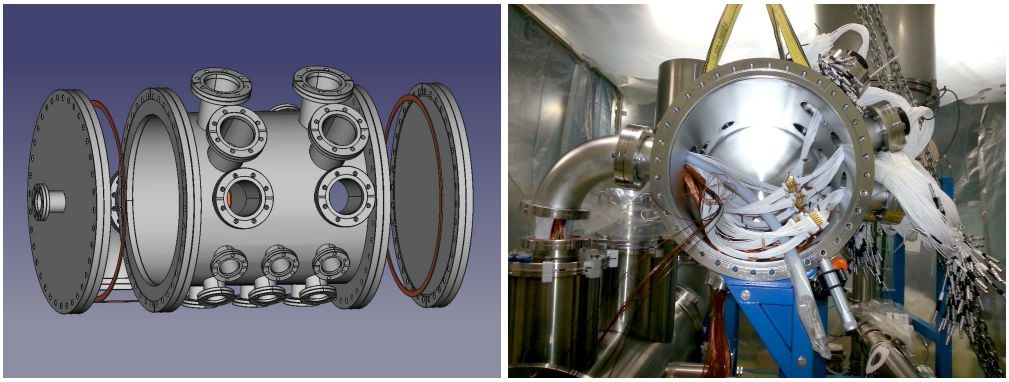

Figure 4.10: Breakout box. Left: Technical drawing. 6 CF63 nipples and 9 CF40 nipples without the feedthrough flanges are visible. Right: Picture of the breakout box during its installation in the cryogenic system. The feedthrough flanges for the cables are attached and the cable bunches are connected in the body of the breakout box.

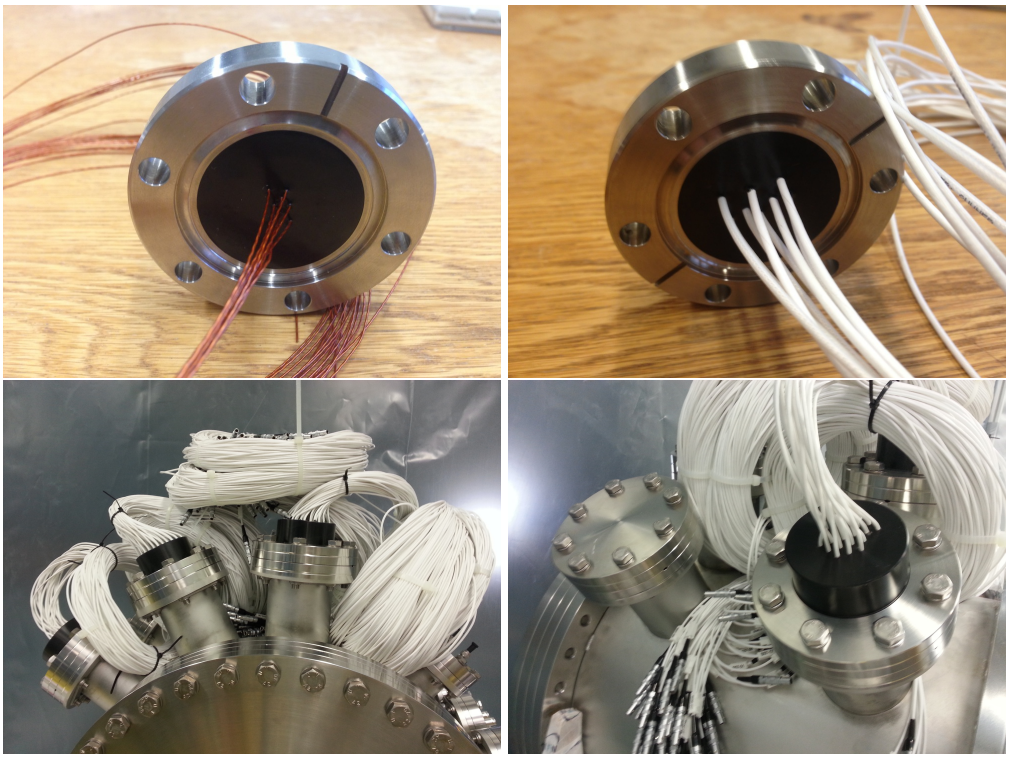

Figure 4.11: Potted feedthroughs: Top: Example CF40 flange with 10 Kapton insulated high voltage cables (left) and 10 PTFE coaxial signal cables (right) potted into the flange. Bottom: Signal feedthroughs for XENON1T installed to the breakout box.

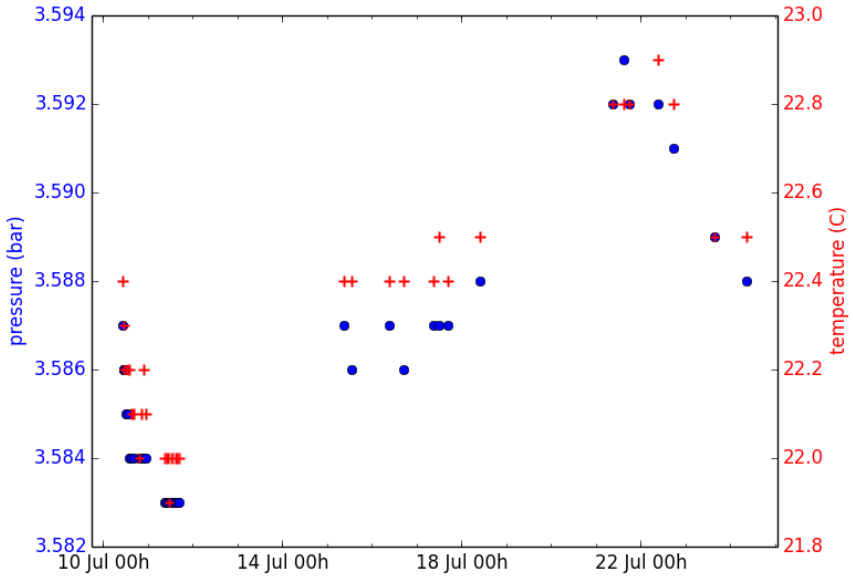

Figure 4.12: Stability in bar of the over pressure using the potted feedthrough at 3.6 bar measured over 2 weeks. The pressure i (blue dots) varies within about 10 mbar. The temperature (red crosses) varies analog to the pressure.

Over two weeks the pressure was constant within 10 mbar. Pressure fluctuations are strongly correlated to temperature changes in the lab. The test shows an impressive stability of the pressure of the feedthroughs.

4.3 Screening results

Due to the stringent background requirements and in order to establish an accurate background model, all materials that are used in XENON1T are screened by high purity germanium spectrometers (HPGe) and Inductively coupled plasma mass spectrometry (ICP-MS). The most relevant γ-emitters are the isotopes in the natural uranium and thorium decay chains. However, these isotopes also contribute to the nuclear recoil background due to neutrons created in (α, n) reactions. Furthermore the isotopes ^{40}K, ^{60}Co are ^{137}Cs contribute to the electronic recoil background.

The low-background HPGe detectors Gator [86] and GeMPI [87, 88] are located at the LNGS. The ICP-MS measurements were carried out by the chemistry laboratory of the LNGS. The measurements with Gator, as well as the analysis of the background contribution were performed by Francesco Piastra and will be published in his PhD thesis. The results for the iso-

topes in the U and Th chains ^{238}U, ^{226}Ra, ^{228}Ra, ^{232}Th, ^{228}Th and ^{235}U are listed in table 4.1. The results for the three gamma emitters ^{40}K, ^{60}Co, ^{137}Cs are shown in table 4.2. Upper limits are given at 90% confidence level and the quoted errors include statistical and systematical errors.

For the measurements of the cables we ordered two different batches for the pipe and for the TPC. The batch of Kapton wires and the PTFE coax cables for the TPC for 42.5 and 41.5 life days respectively. The Kapton and PTFE cables in the pipe were screened for 11.8 and 12.5 life days respectively. Both results are given in tables 4.1 and 4.2. For the cables in the building the results from the pipe cables will be used.

Table 4.3 shows the number of the installed cables for each part of the cable tree together with the total length and the total mass. There is a total of 11.4 km. The Kapton single wire and the PTFE signal coaxial cables have a mass of 0.78 kg and 8.8 kg per 1000 meters, respectively. The total mass and the activities of the cables and connectors will be included in a full GEANT4 [65] simulations of the XENON1T detector to determine their contribution for the background.

4.4 Assembly and installation

This section we describes the installation of the three different parts, as described in section 4.1, in chronological order.

4.4.1 Cable pipe

After the water tank and the structure of the building were erected underground the first part to be installed was the cryogenic pipe containing the pipe for the cables (part A in figure 4.1). A technical drawing of the pipe is shown in figure 4.13. The cable pipe consist of a straight 5.93 meter long stainless steel pipe which is connected to a 1.45 meter long bellow, 0.9 meters of which are bent in an angle of 85°. The flexible bellow is required since the cable pipe has to be pushed into a bent pipe. The total length of the pipe is 7.38 meters and its diameter is 100 mm. On the TPC side the pipe will end inside the vessel that houses the TPC. On the building side the pipe is connected on the cryogenic system to a pipe that guides the cables to the breakout box (elbow 1 and 2 in figure 4.1). The cables in the pipe have to reach from the end of the bellow (the top of the TPC vessel) on the one side to the center of the breakout box on the other side. The distance from the pipe to the breakout box is another 0.7 meters. The cables in the pipe are 9.6 meters long.

In the water tank the cryogenic pipe is attached to the vessel that houses the TPC. This cryogenic pipe contains various other pipes and is surrounded by an insulation vacuum. The

		^{238}U	^{226}Ra	^{228}Ra / ^{232}Th	^{228}Th	^{235}U
High voltage						
cables						
mBq/kg$^{(1)}$	Ge	< 179	11.2 ± 3.1	< 24.2	< 15.2	< 9.06
mBq/kg$^{(2)}$	Ge	< 130	4.5 ± 1.1	< 2.2	< 3.6	< 2.8
mBq/kg	MS	4.2	–	0.73	–	–
μBq/m$^{(1)}$	Ge	< 140	8.7 ± 2.4	< 18.9	< 11.9	< 7.07
μBq/m$^{(2)}$	Ge	< 101	3.5 ± 0.9	< 1.71	< 2.8	< 2.2
μBq/m	MS	3.3	–	0.57	–	–
pins						
mBq/kg	Ge	< 130	< 4.77	< 9.66	< 4.70	< 2.83
μBq/cpl.	Ge	< 211	< 0.775	< 1.14	< 0.764	< 0.460
μBq/cpl.	MS	< 0.82	–	< 0.27	–	–
Signal						
PTFE cables						
mBq/kg$^{(1)}$	Ge	< 27	0.4 ± 0.2	< 0.77	< 0.56	< 1.5
mBq/kg$^{(2)}$	Ge	< 25	< 0.59	< 0.58	0.6 ± 0.2	< 1.0
mBq/kg	MS	1.9 ± 0.6	–	2.4 ± 0.7	–	–
μBq/m$^{(1)}$	Ge	< 238	3.5 ± 1.8	< 6.8	< 4.9	< 13
μBq/m$^{(2)}$	Ge	< 220	< 5.2	< 5.1	5.3 ± 1.8	< 8.8
μBq/m	MS	17 ± 5	–	22 ± 6	–	–
Kapton cables						
mBq/kg	Ge	< 179	11.2 ± 3.1	< 24.2	< 15.2	< 9.06
mBq/kg	MS	5.1	–	0.73	–	–
μBq/m	Ge	< 999	62.5 ± 17.3	< 135	< 84.8	< 50.6
μBq/m	MS	28	–	4.1	–	–
pins						
mBq/kg	Ge	487 ± 87	< 19.2	42.5 ± 7.9	48.0 ± 5.7	22.4 ± 4.0
μBq/cpl.	Ge	431 ± 77	< 17.0	37.6 ± 6.9	42.4 ± 5.0	19.8 ± 3.5
μBq/cpl.	MS	590 ± 80	–	30.2 ± 9.0	–	27.2 ± 8.3

Table 4.1: Results of the two different methods, germanium (Ge) screening and the mass spectroscopy (MS), in mBq/kg for isotopes in the ^{235}U, ^{238}U and ^{232}Th chains for cables and connector pins. The isotopes ^{228}Ra and ^{232}Th belong to the same chain and are in equilibrium. Hence they are presented in the same column. However the mass spectrometer measures ^{232}Th whereas germanium detectors are sensitive to ^{228}Ra. The conversion to μBq per cable meter or μBq per connector pin couple (cpl.) is given. $^{(1)}$Batch 1: installed in the pipe. $^{(2)}$Batch 2: installed into the TPC. The Kapton signal cables are not used in the experiment.

	^{40}K	^{60}Co	^{137}Cs
High voltage			
cable (mBq/kg)$^{(1)}$	828 ± 96	< 5.03	< 5.08
cable (mBq/kg)$^{(2)}$	2600 ± 300	< 1.1	< 0.54
cable (μBq/m)$^{(1)}$	646 ± 75	< 3.92	< 3.96
cable (μBq/m)$^{(2)}$	2028 ± 234	< 0.86	< 0.42
pins (mBq/kg)	23.1 ± 5.7	< 1.75	< 1.04
pins (μBq/cpl.)	3.75 ± 0.93	< 0.284	< 0.169
Signal coaxial			
PTFE cable (mBq/kg)$^{(1)}$	9 ± 3	< 0.27	< 0.41
PTFE cable (mBq/kg)$^{(2)}$	33 ± 4	< 0.21	< 0.10
PTFE cable (μBq/m)$^{(1)}$	79 ± 26	< 2.4	< 3.7
PTFE cable (μBq/m)$^{(2)}$	290 ± 35	< 1.8	< 0.88
Kapton cable (μBq/m)	4620 ± 536	< 28.1	< 28.3
pin (mBq/kg)	198 ± 32	< 4.31	< 3.70
pin (μBq/cpl.)	175 ± 28	< 3.81	< 3.27

Table 4.2: Results of the germanium screening in mBq/kg for ^{40}K, ^{60}Co and ^{137}Cs for the cables and connector pins. Also the conversion to μBq per cable meter or μBq per connector pin couple (cpl.) is given. $^{(1)}$Batch 1: installed in the pipe. $^{(2)}$Batch 2: installed into the TPC. The Kapton signal cables are not used in the experiment.

	number	length (m)	mass (kg)
High voltage			
1. TPC	261	485.6	0.38
2. pipe	468	4492.8	3.50
3. building	312	206.0	0.16
Total	1041	5184.4	4.04
Signal coaxial			
1. TPC	287	671.0	5.64
2. pipe	432	4147.2	34.84
3. building	312	1378.8	11.58
Total	1031	6197.0	52.05

Table 4.3: Number of cables together with the total cable length and mass for both installed cable types, Kapton single wire and PTFE coax cable, for each part.

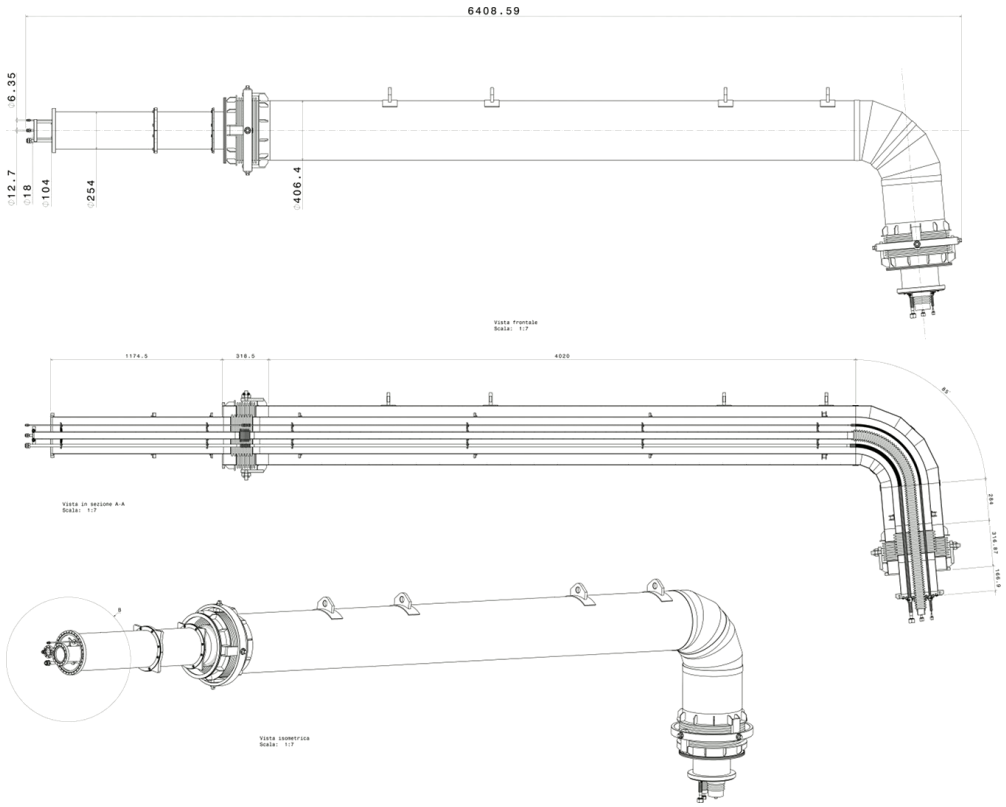

Figure 4.13: Technical drawing of the umbilical pipe that contains the cable guiding pipe in the XENON1T experiment.

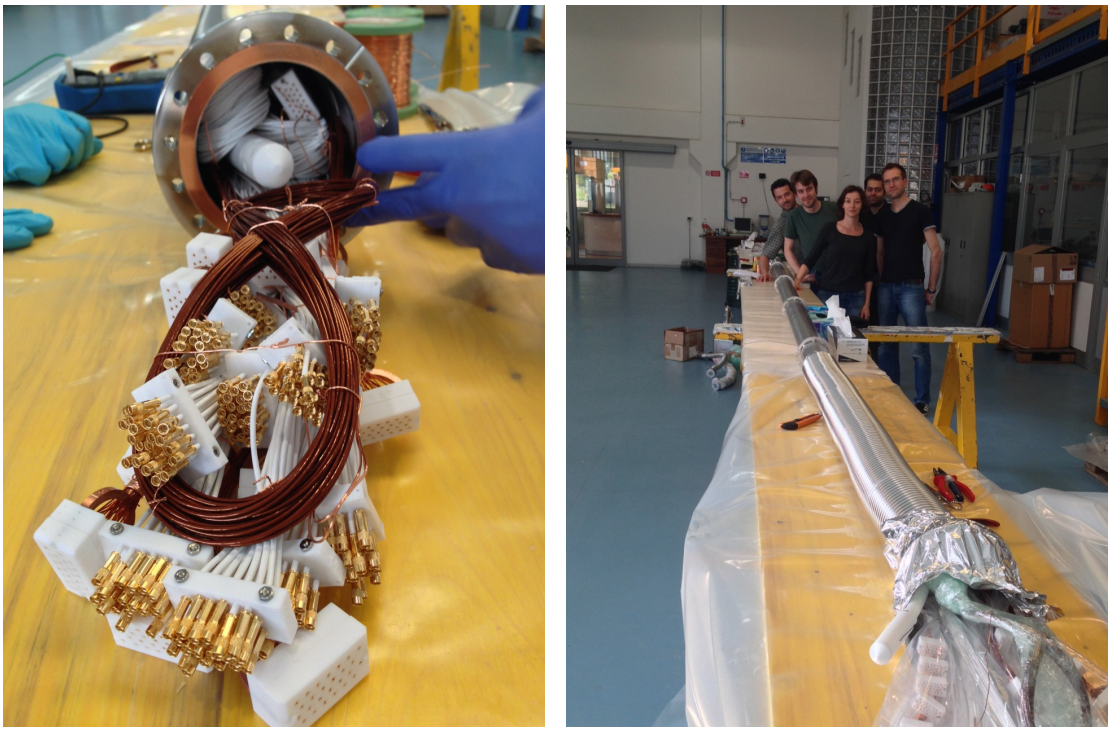

Figure 4.14: Installation of the cables into the pipe. Left: The cable bunches at the TPC side of the pipe. The additional cables for the upgrade to XENONnT are pushed back into the pipe and fixed. Right: Cable pipe after finished insertion of the cables. The cable bunches are packed in plastic foil to protect them against dirt.

whole pipe is produced by ALCA Technology [89] in Italy. Before the cable pipe was inserted into the cryogenic pipe we installed the cables into the cable pipe at the ALCA facilities. Since the cable pipe is nested at a hard accessible location we installed an additional number of cables in the pipe (c.f. table 4.3), since the XENON1T detector is planned to be upgraded to XENONnT with an enlarged target mass and an increased number of PMTs. For both, Kapton single wires and PTFE coaxial cables, we installed 18 bunches. 11 bunches will be used for the operation of XENON1T. The ends of all other bunches were bent back into the pipe such they do not hang into the vessel of the TPC in order to reduce their contribution to the radioactive background near the TPC.

We installed the cables in June 2014 (Figure 4.14). They were pulled bunch-wise into the cable pipe. On both sides the bunches are terminated with pins that are held in a connector. The whole installation procedure was trained with an 6 meter long aluminum pipe (95 mm diameter) at the University of Zürich before traveling to ALCA. At the beginning of the installation, a 12 meter long steel wire was pushed into the empty pipe. Each bunch was fixed to

this wire and pulled into the pipe. The steel wire itself was pulled back by another steel wire that was carried along during the whole procedure to ensure that the steel wire never goes between cables in one bunch and that each bunch is pulled into the pipe on top all bunches that are already installed. After the installation of the cables the cable pipe was closed and pumped to keep the cables in a clean environment. In Autumn 2014 the whole cryogenic pipe was placed on its position in the water tank.

4.4.2 Building site with the breakout box

In January 2015 we connected the breakout box to the cryogenic system and positioned the cables in the building. We attached all feedthrough flanges to the slots on the breakout box. The slots which have been added to be used in the XENONnT upgrade, were closed with blind flanges. We leak checked the assembled breakout box and the leak rate was proved to reach our goal of $< 5 \times 10^{-11}\,\mathrm{mbar} \cdot \mathrm{l/s}$.

Since the time information of the signal is crucial for the experiment the total length of all signal cables have to be the same. The cables inside the pipe have all the same length. But the cables inside the TPC have to be longer when they come from the bottom PMT array. We therefore have calculated a length difference of cables between the top and the bottom array of 80 cm. This length difference has to be compensated outside of the vacuum. Therefore cables connected to the top array are 80 cm longer than the once for the bottom array.

Before we removed the cap that closes the pipe on the building side we started to flush the pipe with clean nitrogen from the other side. Then the cables were bunch-wise pushed through the elbows. A steel wire was not needed given the short length of the pieces the cables had to be pushed through.

Inside the breakout box we connected the bunches of the two parts. We closed the breakout box and checked the connections.

4.4.3 Cables for the TPC

We divided the PMTs of both arrays into groups of 24. Figure 4.15 shows a schematic of the groups in the arrays. The 127 PMTs of the top array form 6 groups. Their bunches are routed through 3 channels on the side of the bell in an angle of 120° from each other. Hence each channel contains the bunches of two PMT groups. The 121 PMTs of the bottom array were divided into 5 groups of 24 PMTs. One remaining PMTs was assigned to a top PMT group. There are 4 cable guides at the side of the TPC. Hence the cables of the 5 groups are routed along 4 positions. One cable guide contains the bunches of two PMT groups. The grouping

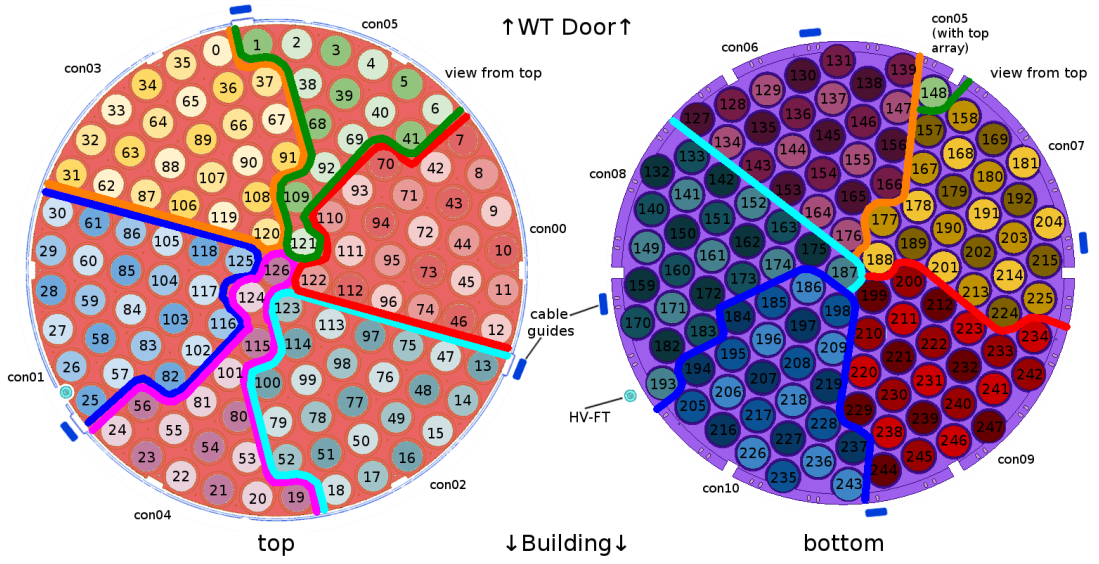

Figure 4.15: Grouping of the PMTs inside the TPC: The grouping was optimized to result a minimum cable length. One group contains maximum 24 PMTs. There are 6 groups in the bottom PMT array (left) and 5 groups in the bottom (right). One of the PMTs in the bottom array (number 148) had to be added to a group of the top array. The schematic shows both array from the top, such the service building is below and the watertank door above the picture.

was optimized to minimize the length of the cables from the PMTs to the top of the TPC, where they are connected to the cables of the pipe.

We cut the signal cables to two different lengths, one for the top and one for the bottom PMTs. The HV cable for each PMTs was individually cut to the required length. We labeled the voltage divider for each PMT and inserted them into a Plexiglas frame that kept all of them in the final configuration (Figure 4.16). Having the voltage divider in these frames we attached the HV and signal cables. The ground returns of all 24 PMTs in one group were collected in a copper block. Cables from this block are inserted into the HV connector. For the installation of the PMT arrays with the Plexiglas frames we could insert each voltage divider to the assigned position in the array before we attached the PMT to it. The arrays with the PMTs and attached voltage divider is shown in figure 4.17.

After the assembly of the TPC we routed the cables into the cable guides to the top of the TPC. After the installation of the TPC into the watertank we connected them to the cables of the pipe.

The vessel of the TPC has been closed in December 2015. In February 2016 the data acquisition group tested every single PMT. For that purpose light guiding fibers were installed to expose the PMTs with pulsed light signals from an LED outside of the watertank to induce

Figure 4.16: Plexiglas holder for the top (left) and the bottom (right) PMT array with the voltage divider and the cables inserted at their dedicated position

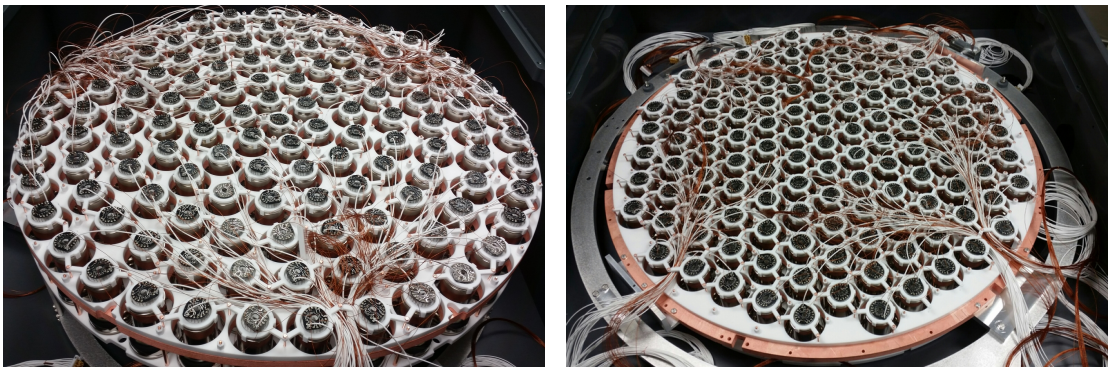

Figure 4.17: Assembled arrays

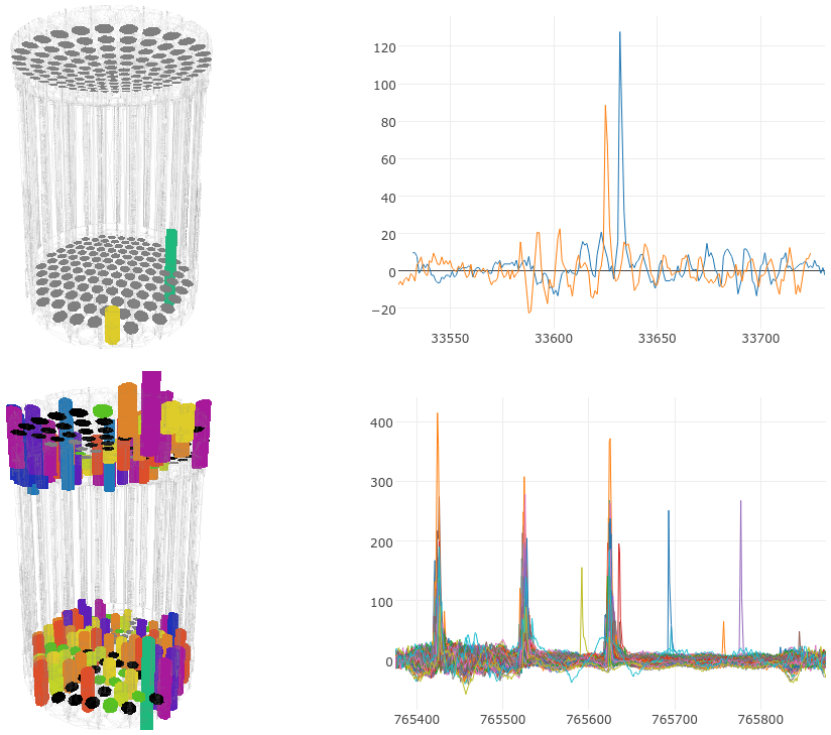

Figure 4.18: Waveforms of the PMTs in XENON1T from an LED run. The example on the top shows the situation with a low light level. Only 2 PMTs are responding with a signal that is 4 σ higher than the base line. For the example on the bottom the light level is higher. Figure made by Daniel Coderre.

single photoelectrons in every PMT. Each PMT was tested individually and from every PMT single photoelectron signals could be observed. This proves that the high voltage and signal connections of all PMTs are working. Figure 4.18 gives an overview of the recorded waveforms by the PMTs during an LED run for different light levels. Each PMT is shown if the response to the LED light exceeds 4 σ of the base line. Figure 4.19 shows the average signal strength (area under the LED pulse) for all PMTs.

4.5 Conclusion

For the 254 PMTs employed in the XENON1T TPC signals and high voltage has to be transported over a distance of 16 meters. We tested various options for cables and connectors. We concluded that the best solution for the signal transmission is to use the PTFE coaxial cable RG196 with MMCX connectors and for the high voltage supply Kapton insulated copper wires with d-subminiature pins. We developed connectors made of PTFE to connect bunches of 24 channels each. For the vacuum feedthroughs we decided to use CF40 and CF63 flanges in which the cables are potted with a low outgassing epoxy. All cables are screened for their

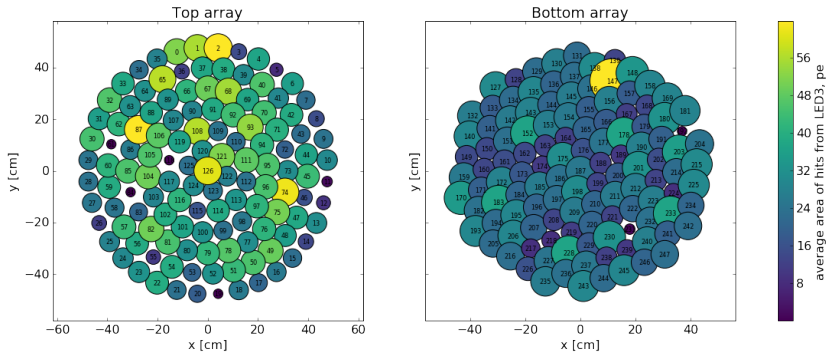

Figure 4.19: Signal size form LED runs of all PMTs in XENON1T. Figure made by Payam Pakarha.

radio-activity with high purity germanium detectors and inductively coupled plasma mass spectrometry. The cables were successfully installed in three different steps and the connection between these steps are established by custom made connectors. Every cable was tested to transmit high voltage or signal and was proved to be fully functional.

References

[1] Gianfranco Bertone, *Particle Dark Matter – Observations, Model and Searches*. Cambridge University Press, 2013.

[2] Planck Collaboration: P. A. R. Ade et al., "Planck 2013 results. XVI. Cosmological parameters," *Astronomy and Astrophysics **571** 66*, no. A16, 2014.

[3] J.H. Oort, "The force exerted by the stellar system in the direction perpendicular to the galactic plane and some related problems," *Bull. Astr. Inst. Neth **6** 249*, 1932.

[4] V.I. Korchagin et al., "Local Surface Density of the Galactic Disk from a 3-D Stellar-Velocity Sample," *arXiv:astro-ph/0308276*, 2003.

[5] F. Zwicky, "Die Rotverschiebung von extragalaktischen Nebeln," *Helvetica Physica Acta **6** 110-127*, 1933.

[6] L. Volders, "Neutral hydrogen in M 33 and M 101," *Bull. Astron. Inst. Neth. **1**, 379*, 1959.

[7] V. Rubin, J. Ford and W. Kent, "Rotation of the Andromeda Nebula from a Spectroscopic Survey of Emission Regions," *Astrophys. J. **159** 379*, 1970.

[8] K. G. Begeman, A. H. Broeils and R. H. Sanders, "Extended rotation curves of spiral galaxies: dark haloes and modified dynamics," *Mon. Not. Roy. Astron. Soc. **249** 523*, 1991.

[9] A. Einstein, "Über den Einfluss der Schwerkraftauf die Ausbreitung des Lichtes," *Annalen der Physik **340** no 10*, 1911.

[10] F. Zwicky, "Nebulae as Gravtiational Lenses," *Phys. Rev. **51** 290*, 1937.

[11] D. Clowe et al, "A Direct Empirical Proof of the Existence of Dark Matter," *Astrophys. J. **648** L109*, 2006.

[12] M. Milgrom, "A modification of the Newtonian dynamics as a possible alternative to the hidden mass hypothesis," *Astrophysical Journal **270**: 365–370.*, 1983.

[13] C. L. Bennet et al, "4-Yeak 4-Year COBE DMR Cosmic Microwave Background Observations: Maps and Basic Results," *Astrophys. J. **464***, 1996. `arXiv:astro-ph/9601067`.

[14] E. Komatsu et al., "Seven-year Wilkinson Microwave Anisotropy Probe (WMAP) observations: cosmological interpretation," *Astrophys. J. Suppl.* ***192*** *18*, 2011. arXiv:1001.4538.

[15] M. Ackermann et al, "Search for Gamma-ray Spectral Lines with the Fermi Large Area Telescope and Dark Matter Implications," *Phys. Rev. D* ***88****, 082002*, 2013. arXiv:1305.5597.

[16] J. Aleksić et al, "Searches for Dark Matter annihilation signatures in the Segue 1 satellite galaxy with the MAGIC-I telescope," *JCAP* ***1106****:035*, 2011. arXiv:1103.0477.

[17] A. Abramowski et al, "Search for a Dark Matter annihilation signal from the Galactic Center halo with H.E.S.S," *Phys. Rev. Lett.* ***106****:161301*, 2011. arXiv:1103.3266.

[18] M. G. Aartsen et al, "Search for dark matter annihilations in the Sun with the 79-string IceCube detector," *Phys. Rev. Lett.* ***110****, 131302*, 2013. arXiv:1212.4097.

[19] S. Adrián-Martinez et al, "First Search for Dark Matter Annihilation in the Sun Using the ANTARES Neutrino Telescope," *JCAP* ***2013***, 2013. arXiv:1302.6516.

[20] O. Adriani et al, "The cosmic-ray positron energy spectrum measured by PAMELA," *Phys. Rev. Lett.* ***111*** *081102*, 2013. arXiv:1308.0133.

[21] M. Aguilar et al. (AMS Collaboration), "First Result from the Alpha Magnetic Spectrometer on the International Space Station: Precision Measurement of the Positron Fraction in Primary Cosmic Rays of 0.5–350 GeV," *Phys. Rev. Lett.* ***110****, 141102*, 2013.

[22] ATLAS Collaboration, "Search for dark matter candidates and large extra dimensions in events with a jet and missing transverse momentum with the ATLAS detector," *JHEP* ***1304*** *075*, 2013. arXiv:1210.4491.

[23] CMS Collaboration, "Search for New Physics with a Mono-Jet and Missing Transverse Energy in pp Collisions at sqrt(s) = 7 TeV," *Phys. Rev. Lett.* ***107****, 201804*, 2011. arXiv:1106.4775.

[24] Guillaume Plante, *The XENON100 Dark Matter Experiment: Design, Construction, Calibration and 2010 Search Results with Improved Measurement of the Scintillation Response of Liquid Xenon to Low-Energy Nuclear Recoils.* PhD thesis, Coumbia University, 2012.

[25] R. Bernabei et al, "The DAMA/LIBRA apparatus," *Nucl. Instrum. Meth. A****592****:297-315*, 2008. arXiv:0804.2738.

[26] C. E. Aalseth et al, "CoGeNT: A Search for Low-Mass Dark Matter using p-type Point Contact Germanium Detectors," *Phys. Rev. D **88**, 012002*, 2013. arXiv:1208.5737.

[27] R. Agnese et al, "Silicon Detector Dark Matter Results from the Final Exposure of CDMS II," *Phys. Rev. Lett. **111**, 251301*, 2013. arXiv:1304.4279.

[28] E. Armengaud et al, "Final results of the EDELWEISS-II WIMP search using a 4-kg array of cryogenic germanium detectors with interleaved electrodes," *Phys. Lett. B **702** 329-335*, 2011. arXiv:1103.4070.

[29] G. Angloher et al, "Results from 730 kg days of the CRESST-II Dark Matter Search," *The European Physical Journal C 72:1971*, 2012. arXiv:1109.0702.

[30] S. Archambault et al, "Dark Matter Spin-Dependent Limits for WIMP Interactions on 19-F by PICASSO," *Phys. Lett. B **682**:185-192*, 2009.

[31] E. Behnke et al, "First dark matter search results from a 4-kg CF3I bubble chamber operated in a deep underground site," *Phys. Rev. D **86**, 052001*, 2012. arXiv:1204.3094.

[32] C. Amole et al, "Dark Matter Search Results from the PICO-2L C3F8 Bubble Chamber," *Phys. Rev. Lett. **100**, 231302*, 2015.

[33] E. Aprile et al. (XENON100)., "The XENON100 Dark Matter Experiment," *Astropart. Phys. **35** 573-590*, 2012.

[34] E. Aprile et al (XENON collaboration), "Physics reach of the XENON1T dark matter experiment," *JCAP04, 027*, 2016. arXiv:1512.07501.

[35] D. Yu. Akimov et al, "WIMP-nucleon cross-section results from the second science run of ZEPLIN-III," *Phys. Lett. B **709***, 2012. arXiv:1110.4769.

[36] D. S. Akerib et al, "The Large Underground Xenon (LUX) Experiment," *Nuclear Inst. and Methods in Physics Research A**704** 111 - 126*, 2013. arXiv:1211.3788.

[37] A. Wright, "The DarkSide Program at LNGS," *Proceedings of the DPF-2011 Conference*, 2011. arXiv:1109.2979.

[38] K. Abe et al, "Light WIMP search in XMASS," *Phys. Lett. B **719** 78-82*, 2013. arXiv:1211.5404.

[39] J. Billard et al, "Implication of neutrino backgrounds on the reach of next generation dark matter direct detection experiments," *Phys. Rev. D **89** 023524*, 2014. arXiv:1307.5458.

[40] J. Angle et at., "First Results from the XENON10 Dark Matter Experiment at the Gran Sasso National Laboratory," *Phys. Rev. Lett.* ***100***, no. 201303, 2008. arxiv:0706.0039.

[41] Laboratori Nazionali del Gran Sasso (LNGS) https://www.lngs.infn.it/en.

[42] E. Aprile et al. (XENON100)., "Dark Matter Results from 225 Live Days of XENON100 Data," *Phys. Rev. Lett.* ***109****, 181301*, 2012.

[43] E. Aprile et al. (XENON100)., "Limits on spin-dependent WIMP-nucleon cross sections from 225 live days of XENON100 data," *Phys. Rev. Lett.* ***111****, 021301*, 2013.

[44] J. Falbe and M. Regitz, *Römpp Chemie Lexikon.* Thieme, 1992.

[45] U. Asaf and I. T. Steinberger, "Photoconductivity and electron transport parameters in liquid and solid xenon," *Phys. Rev. B* ***10*** *4464 – 4468*, 1974.

[46] J. Jortner et al., "Local Excitations in Condensed Ne, Ar, Kr and Xe," *The Journal of chemical physics* ***42*** *no 12, 4250*, 1965.

[47] E. Aprile et al., "Liquid xenon detector for particle physics and astrophysics," *Review of modern physics* ***82*** *no. 3, 2043 – 2097*, 2010.

[48] S. Kubota, M. Hishida and J. Raun, "Evidence for a TripletState of the Self-Trapped Exciton States in Liquid Argon, Krypton and Xenon," *J. Phys. C* ***11*** *2645*, 1978.

[49] A. Hitachi et al., "Effect of Ionization Density on the Time Dependence of Luminescence from Liquid Argon and Xenon," *Phys. Rev. B* ***27****, 5279*, 1983.

[50] C. E. Dahl, *The physics of background discrimination in liquid xenon and first results from XENON10 in the hunt for WIMP dark matter.* PhD thesis, Princeton University, 2009.

[51] T. Doke et al., "Absolute Scintillation Yields in Liquid Argon and Xenon for Various PartiPart," *Jpn. J. Appl. Phys.,* ***41****, 1538*, 2002.

[52] J. Lindhard et al., "Integral Equations Governing Radiation Effects," *Mat. Fys. Medd. Dan. Vid. Selsk.* ***33*** *no. 10*, 1963.

[53] P. Sorensen and C. E. Dahl, "Nuclear recoil energy scale in liquid xenon with application to the direct detection of dark matter," *Phys. Rev. D* ***83***, no. 063501, 2011.

[54] P. F. Smith and J. D. Lewin, "Review of mathematics, numerical factors, and correlations for dark matter experiment based on elastic nuclear recoil," *Phys. Rept.* ***187*** *203*, 1990.

[55] P. Sorensen et al, "The scintillation and ionization yield of liquid xenon for nuclear recoils," *Nucl. Instrum. Meth. A* ***601****, 339-346*, 2009. arXiv:0807.0459.

[56] V. N. Lebedenko et al., "Results from the First Science Run of the ZEPLIN-III Dark Matter Search Experiment," *Phys. Rev. D* ***80****, 052010*, 2009. arXiv:0812.1150.

[57] M. Horn et al., "Nuclear recoil scintillation and ionisation yields in liquid xenon from ZEPLIN-III data," *Phys. Rev. Lett.* ***705****, 471-476*, 2011. arXiv:1106.0694.

[58] E. Aprile et al. (XENON100)., "Response of the XENON100 Dark Matter Detector to Nuclear Recoils," *Phys. Rev. D.* ***88*** *012006*, 2013.

[59] E. Aprile et al., "Scintillation Response of Liquid Xenon to Low Energy Nuclear Recoils," *Phys. Rev. D* ***72****, 072006*, 2005. arXiv:astro-ph/0503621.

[60] E. Aprile et al., "New Measurement of the Relative Scintillation Efficiency of Xenon Nuclear Recoils Below 10 keV," *Phys. Rev. C* ***79****, 045807*, 2009. arXiv:0810.0274.

[61] V. Chepel et al., "Scintillation efficiency of liquid xenon for nuclear recoils with the energy down to 5 keV," *Astropart. Phys.* ***26*** *58-63*, 2006. arXiv:physics/0512136.

[62] A. Manzur et al., "Scintillation efficiency and ionization yield of liquid xenon for mono-energetic nuclear recoils down to 4 keV," *Phys. Rev. C* ***81****, 025808*, 2010. arXiv:0909.1063.

[63] G. Plante et al, "New Measurement of the Scintillation Efficiency of Low-Energy Nuclear Recoils in Liquid Xenon," *Phys. Rev. C* ***84****, 045805*, 2011. arxiv:1104.1103.

[64] E. Aprile et al., "Simultaneous measurement of ionization and scintillation from nuclear recoils in liquid xenon as target for a dark matter experiment," *Phys. Rev. Lett.* ***97*** *081302*, 2006. arxiv:astro-ph/0601552.

[65] S. Agostinelli et al., "Geant4—a simulation toolkit," *Nuclear Instruments and Methods in Physics Research Section A: Accelerators, Spectrometers, Detectors and Associated Equipment* ***506*** *(3): 250*, 2003.

[66] E. Aprile et al. (XENON100)., "Study of the electromagnetic background in the XENON100 experiment," *Phys. Rev. D* ***83****:082001*, 2011. arXiv:1101.3866.

[67] E. Aprile et al. (XENON Collaboration), "Conceptual design and simulation of a water Cherenkov muon veto for the XENON1T experiment," *JINST* ***9*** *P11006*, 2014. arxiv:14.06.2374.

[68] Hamamatsu Photonics http://www.hamamatsu.com.

[69] Hamamatsu Photonics K.K., "Photomultiplier Tubes – Basics and Aplications," (third edition 2007).

[70] L. Baudis et al., "Signature of Dark Matter Scattering Inelastically Off Nuclei," *Phys. Rev. D **88**, 115014*, 2013.

[71] J. Magill, G. Pfennig, R. Dreher, Z. Sóti, *Karlsruher Nuklidkarte*. Nucleonica GmbH, 2012.

[72] G. Jungman et al., "Supersymmetric dark matter," *Phys.Rept. **267** 195-373*, 1996.

[73] S. Arrenberg, *Searching for Dark Matter with the Cryogenic Dark Matter Search Experiment*. PhD thesis, Universität Zürich, 2011.

[74] L. Vietze et al, "Nuclear structure aspects of spin-independent WIMP scattering off xenon," *Phys. Rev. D **91**, 043520*, 2015. arXiv:1412.6091.

[75] Engel, J. and Pittel, S. and Vogel, P., "Nuclear physics of dark matter detection," *Int.J.Mod.Phys. **E1** 1-37*, 1992.

[76] E. Aprile et al. (XENON100)., "Analysis of the XENON100 Dark Matter Search Data," *Astropart. Phys. **54** 11-24*, 2014.

[77] Szydagis et al., "NEST: A Comprehensive Model for Scintillation Yield in Liquid Xenon," *JINST **6** P10002*, 2011. arxiv:1106.1613.

[78] J. Mock et al., "Modeling Pulse Characteristics in Xenon with NEST," *JINST **9** P04002*, 2014. arxiv:1310.1117.

[79] L. Ni et al., "Preparation of Neutron-activated Xenon for Liquid Xenon Detector Calibration," *Nucl.Instrum.Meth.* **A582***: 569-574*, 2007.

[80] U. Uchida et al. (The XMASS collaboration), "Search for inelastic WIMP nucleus scattering on 129Xe in data from the XMASS-I experiment, status and results," *Prog. Theor. Exp. Phys. 063C01*, 2014. arXiv:1401.4737.

[81] E. Aprile et al. (XENON100)., "Limits on the cross section for inelastic WIMP-nucleon scattering of Xe-129 from 225 live days of XENON data," *to be published.*

[82] Accu-Glass Products, Inc. 30 AWG, Kapton Insulated Wire. http://accuglassproducts.com/.

[83] koax24 30 AWG, RG196 50Ω cable http://www.koax24.de/.

[84] Reliable Hermetic Seals Inc., http://www.rhseals.com/.

[85] Reliable Hermetic Seals Inc., personal correspondance.

[86] L. Baudis et al., "Gator: a low-background counting facilitz at the Gran Sasso Underground Laboratory," *JINST **6** P08010.* arxiv:1103.2125.

[87] N. Neder, G. Heusser and M. Laubenstein, "Low level γ-ray germanium-spectrometer to measure very low primordial radionuclide concentrations," *App. Rad. Isot. **53** 19*, 2000.

[88] D. Budjas et al., "Highly sensitive gamma-spectrometers of gerda for material screening: Part 2," arxiv:0812.0768.

[89] ALCA Technology S.r.l., Schio, Italy http://www.alcatechnology.com/.